

Structural, Electrical and Optical Properties of Transparent Conducting Si-doped ZnO Thin Films Grown by Pulsed Laser Deposition

NESSA FERESHTEH SANIEE



**UNIVERSITY OF
BIRMINGHAM**

A thesis submitted to the University of Birmingham

For the degree of master of philosophy

School of Metallurgy and Materials
The University of Birmingham
SEPTEMBER 2009

UNIVERSITY OF
BIRMINGHAM

University of Birmingham Research Archive

e-theses repository

This unpublished thesis/dissertation is copyright of the author and/or third parties. The intellectual property rights of the author or third parties in respect of this work are as defined by The Copyright Designs and Patents Act 1988 or as modified by any successor legislation.

Any use made of information contained in this thesis/dissertation must be in accordance with that legislation and must be properly acknowledged. Further distribution or reproduction in any format is prohibited without the permission of the copyright holder.

Synopsis

Thin silicon doped zinc oxide films were ablated onto borosilicate glass substrates by pulsed laser deposition of a bulk ZnO target doped with 2 wt% silicon. The rotating target was irradiated at low ambient oxygen pressures by a KrF Excimer laser (Lambda physics LPX 300) emitting pulses of 0.18 ns in length, with frequency of 10 Hz, at a wavelength of 248 nm and with energy fluence of 1-2 J/cm². The temperature of the substrate was changed from room temperature to 500°C at the fixed oxygen pressure of 5 mTorr. The partial oxygen pressure was varied from 0.01 to 500 mTorr at the substrate temperature of 300°C. The growth rate was differed by varying target-to-substrate distance from 50 to 70 mm at 5 mm increment. The films were characterised by atomic force microscopy, Hall effect measurements, ellipsometry, laser microscope, X-ray diffraction, spectrophotometry, four point probe and scanning electron microscopy.

Deposition parameters such as, the substrate temperature, oxygen pressure, target-to-substrate distance and the number of pulses were varied to maximise optical transmittance and minimise resistivity. The optimum deposition circumstances were found to be at a substrate temperature of 300°C, an oxygen pressure of 5 mTorr, target-to-substrate distance of 70 mm, and with 5000 pulses. These conditions yielded a film of resistivity of $4.12 \times 10^{-4} \Omega\text{cm}$ and a transmittance of 89%.

Acknowledgements

I would like to thank my supervisors Prof. Abell and Prof. Crisan for their support and encouragement during my project. They helped me through this one-year research project at many stages and I benefited from their advice, positive outlook and confidence which inspired me and gave me enthusiasm to further my research beyond the ordinary boundaries of an M.Phil. degree.

I would also thank Mr. A. Bradshaw, for his technical and mechanical support on pulsed laser deposition system and XRD.

My thanks go out to Dr. Pavelo and superconductivity group for their spent time and help of atomic force microscopy.

I wish to thank Dr. Koohpayeh who helped me to start my project organized and with purpose.

I would like to thank Dr. Malek who was the first person worked on Si-doped zinc oxide and helped me to use Hall measurements facility at the University of Oxford.

I would like to mention Mr. Paul Stanely for his technical support of scanning electron microscopy.

My thanks are given to Dr. J. Bowen who helped me by Ellipsometry in Chemical Eng. Department.

I would like to mention Dr. Vladimir (University of Oxford) to help with Hall measurements.

My thanks also go to my colleagues Shadi and Gael for their help in this year.

Contents

1	Introduction.....	1
1.1	Transparent Conducting Oxides.....	1
1.2	Pulsed Laser Deposition.....	1
1.3	Objectives of Research.....	2
2	Background Theory and Literature Review.....	3
2.1	Zinc Oxide and Related Compounds: General Properties	3
2.1.1	ZnO Structure.....	3
2.1.2	Concept of Self-texture Control in ZnO Thin Films.....	4
2.1.3	Electrical Conductivity and Doping of ZnO.....	5
2.1.4	Optical Properties of ZnO.....	9
2.2	ZnO Thin-Film Growth by PLD	11
2.2.1	Pulsed Laser Deposition (PLD)	11
2.2.2	Advantages of PLD for ZnO Films.....	12
2.2.3	Optimum PLD Conditions for ZnO Films	12
2.3	Other Thin Film Fabrication Methods	17
2.4	Applications of ZnO Films.....	18
3	Methodology.....	19
3.1	Pulsed Laser Deposition (PLD).....	19
3.2	X-ray Diffraction (XRD).....	21
3.3	Atomic Force Microscopy (AFM)	22
3.4	Scanning Electron Microscope (SEM).....	23
3.5	Thickness Measurement.....	24

3.5.1	Film Thickness Measured Using an Optical Laser Microscope	24
3.5.2	Film Thickness Measured Using an Ellipsometer	25
3.5.3	Film Thickness Measured Using SEM	26
3.6	Optical Transmittance	26
3.7	Electrical Measurements	27
3.7.1	Hall Effect.....	27
3.7.2	Four-Point Probe:.....	28
4	Results and discussion on SZO depositions.....	29
4.1	Effect of PLD Conditions on Si-doped ZnO Films.....	29
4.1.1	Influence of Substrate Temperature on SZO Films	29
4.1.2	Influence of Oxygen Pressure on SZO films	42
4.1.3	Influence of Target-to-substrate Distance on SZO Films	57
4.1.4	Influence of Number of Pulses on SZO films.....	68
5	Conclusion and Future Work	79
5.1	Conclusion.....	79
5.2	Future Work	81
6	Appendix.....	82
6.1	Target Preparation	82
6.2	Hall Effect Measurements.....	87
6.3	Other Deposition Conditions.....	89
7	References.....	91

1 Introduction

1.1 Transparent Conducting Oxides

Transparent conducting oxides (TCO) have an extensive range of applications, including transparent electrodes in flat-panel displays and solar cells, transparent and heat reflecting material for windows in buildings, solar collectors and lamps. For optoelectronic industry use, the film must exhibit high electrical conductivity and high optical transmittance in the visible spectrum [1].

The first report of TCO growth was in 1907 by Baedeker [2] who prepared cadmium oxide (CdO) thin films grown by the thermal oxidation of sputtered cadmium. Since then, TCO films have been broadly used as an important part of many optoelectronic devices. A large number of TCO materials have been studied over the years such as In_2O_3 , SnO_2 , ZnO , and CdO as well as their doped oxides. All of the mentioned TCO materials are n-type semiconductors. However, there have been some studies on fabricating p-type TCO films, such as CuGaO_2 [3] and CuAlO_2 [4] and nitrogen and phosphorus doped ZnO [5, 6]. Of all the TCO films, indium tin oxide (ITO) is the most widely used TCO in optoelectronic device applications. In the last decade, ZnO films doped with impurities, such as Al, Ba, Ga and In, have been keenly considered as TCO (Transparent Conductive Oxides) materials because they are nontoxic and inexpensive and have comparable electrical and optical properties to ITO [7].

1.2 Pulsed Laser Deposition

As the complexity of devices based on TCO materials increases, enhanced optical and electrical properties of the TCO films are essential. Hence, the deposition techniques play an important role to improve the film properties. These techniques include chemical vapor deposition, vacuum evaporation, sputtering, spray pyrolysis [7], and Pulsed Laser Deposition (PLD). The resemblance in stoichiometry between the target and the deposited thin film makes the progression of PLD well suited to the deposition of complex oxides [1]. In the pulsed laser deposition technique, high power laser pulses are employed to evaporate material from the

surface of a target. Because of a combination of the very low ambient pressures in the chamber (10^{-7} mbar) and the high energy beam ablating the target a flux of atoms, ions and electrons is ejected normal to the target surface. The ablated species condense on the substrate located opposite to the target [8]. A schematic diagram of the typical PLD system is shown in Figure 1.1.

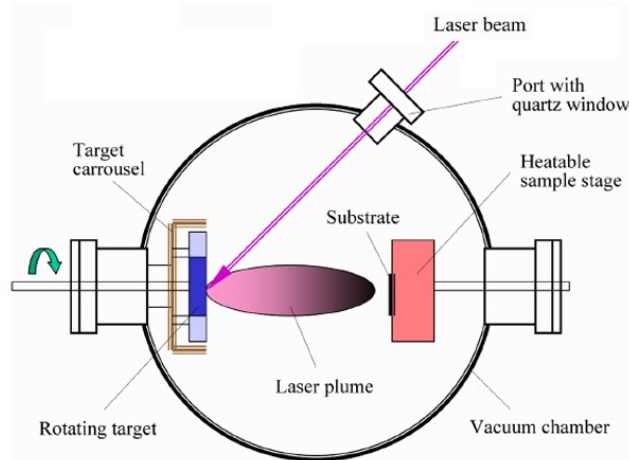


Figure 1.1 Schematic of a PLD chamber [9]

1.3 Objectives of Research

ITO as a transparent conducting oxide thin film has restrictions; above all it is expensive due to the inadequate indium supply. Therefore, research is being carried out to find other appropriate materials for optoelectronic applications. An unpublished research by the University of Birmingham has reported the synthesis by PLD of silicon doped zinc oxide thin films with comparable electrical and optical properties to ITO with the optimal degree of 2 wt.% Si doping. To find out whether the electrical and optical properties of ITO could be replicated, or even improved upon, through Si-doped ZnO, this project was started by preparing the PLD target under various circumstances followed by the deposition of thin films by varying the temperature of the substrate, partial pressure of oxygen during deposition, target-to-substrate distance, and number of pulses. Deposition conditions were varied to minimize resistivity, and maximize optical transmittance.

2 Background Theory and Literature Review

2.1 Zinc Oxide and Related Compounds: General Properties

Zinc oxide (ZnO) is a II-VI compound semiconductor. The recent growth in interest in ZnO semiconductor materials can be seen from more than 1500 papers on ZnO thin-film growth and properties published in the last 5 years. From the exciting new developments in several key areas, pure or doped ZnO films appear to be a highly promising new and advanced functional material.

2.1.1 ZnO Structure

ZnO occurs in nature as the mineral zincite. ZnO crystallizes like most of the group II-VI binary compound semiconductors, in the hexagonal wurtzite structure. It has a polar hexagonal axis, the c-axis, chosen to be parallel to z (0001). The zinc atoms locate almost in the position of hexagonal close packing. Every oxygen atom places within a tetrahedral group of four zinc atoms. The thermodynamically stable crystal structures shared by ZnO at ambient conditions, is wurtzite (B 4-Type) as schematically shown in Figure 2.1 [7].

The hexagonal unit cell in wurtzite structure has two lattice parameters, a and c , in the ratio of $c/a=1.633$ and belongs to the space group of $P6_3mc - C_{6v}^4$ ($a = 0.3296$ and $c = 0.52065$ nm) [8]. The structure of ZnO can be basically illustrated as a number of sporadic planes composed of O^{2-} and Zn^{2+} ions, tetrahedrally coordinated and stacked in an alternate sequence along the c-axis. A non-central symmetric structure can be made by the tetrahedral coordination in ZnO [10].

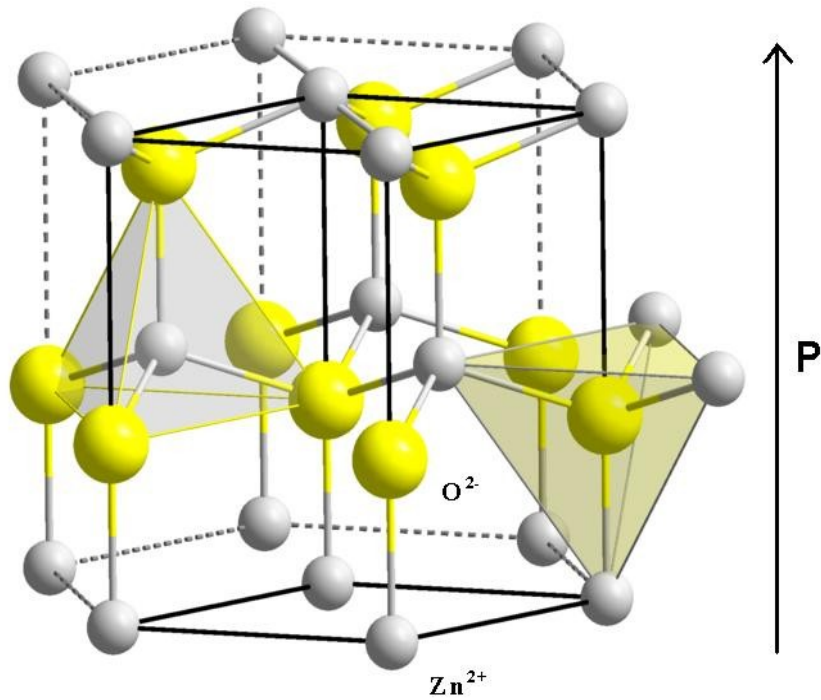


Figure 2.1 The wurtzite lattice of ZnO: small circles represent zinc atoms, whereas large circles depict oxygen atoms. The tetrahedral coordination of Zn–O is shown [11] It has a polar hexagonal axis, the c-axis, chosen to be parallel to z.

2.1.2 Concept of Self-texture Control in ZnO Thin Films

In general, film grows to minimize the surface energy. The surface free energy of each crystal plane affects the preferred orientation of thin films. The surface free energy is strongly dependant on the hybridized orbit in semiconductors. The surface of the film is likely to be the (0001) plane, as a sp^2 hybridized orbit has a second order directed orbit and the bond makes a layered graphite structure. In most semiconductors, the most important bonding style is an sp^3 hybridized orbit, in which each directed orbit spreads along the [111] direction in the cubic system, and along [0001] direction in the hexagonal system. The surfaces of the films deposited on the amorphous substrates like glass, tend to be on one of the (111) and (0001) planes, because

these planes have minimum surface free energies. This can be called “preferred orientation”; this word is not only applied to the self-textured films but also applied to textured structure caused by the epitaxial effect. Highly oriented or single crystalline epitaxial film can be obtained by strong self-texture if it overcomes the force of a substrate, which limits achieving a specific crystallographic structure (epitaxy)[12]. When no influence of epitaxy exists, the film will grow on the plane with the minimum surface energy, which is parallel to the surface below roughening temperature [13]. The close-packed plane plays a significant role in the eventual texture of the film. The sp^3 hybridized orbit forms the tetrahedral coordination in ZnO. It is also calculated that the surface energy of the (002) plane is the lowest in the ZnO crystal (Figure 2.2) [14].

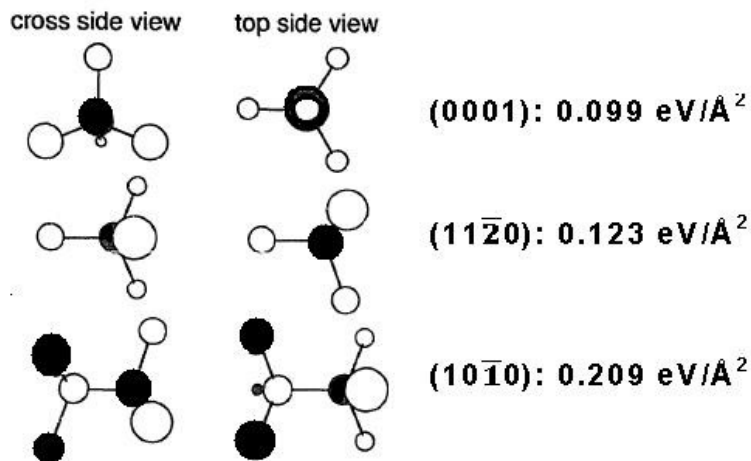


Figure 2.2 Atomic arrangement and calculated densities of surface energy of ZnO.

2.1.3 Electrical Conductivity and Doping of ZnO

ZnO, as a large-band-gap and direct material, is attracting a lot of interest for a range of optoelectronic applications. The major difficulty for the application of ZnO as a material for optoelectronic devices is ambipolar doping. Doping of n-type with shallow donors is easily achievable up to high densities, while the opposite type (p-type by shallow acceptors) is barely possible. This problem is found often for wide band gap materials. The semiconductors ZnO, ZnSe or GaN are in general n-type while ZnTe, Cu₂O or CuCl are commonly p-type [15].

Hall effect is the most extensively used method to measure the electrical properties. For semiconductor materials, it gives the carrier concentration and carrier mobility. In particular, experimental data on Hall measurements give quantitative information on uniformity, impurities, imperfections, and scattering mechanisms.

2.1.3.1 N-type doping

Negatively charged electrons are added to the semiconductor by n-type dopants. For n-type doping one would be selected to replace Zn or O with atoms that have one or two electrons more in the outer shell than the atom which they substitute. Hence the group III or IV elements Al, Ga, In, Sn and Si are shallow and effective donors on Zn cation sites in accordance with:



where the equilibrium is at room temperature, D^0 is the neutral donor and D^+ is the ionized one [15]. Doping of ZnO films by aluminium, gallium or indium is reported [16-23] to have a significant effect on their electrical properties. Doping of ZnO films develops not only their electrical properties but also their steadiness. For example, ZnO films doped with 3 wt% In are found [24] to exhibit thermal stability up to 650 K in vacuum and up to 450 K in oxygen ambient. Many researchers [24-27] have reported highly conductive films of aluminium-doped ZnO.

2.1.3.2 Si-doped ZnO (SZO)

An initial research has been done on heavily doped ZnO with silicon in which it was observed that 2 wt% of heavily silicon-doped ZnO films have high carrier concentration, mobility and lower resistivity in comparison with those of undoped ZnO films (Figure 2.3)[28]. The high carrier concentration in Si-doped ZnO films is attributed to the contribution from Si^{4+} in substitutional sites of Zn^{2+} ions, and from interstitial silicon in the ZnO lattice.

ZnO or Al-doped ZnO targets are commercially available, but pressed pellets prepared from Si-doped ZnO powders have not been produced. The full details of Si-doped ZnO target preparation can be seen in the Appendix. Preparation of ceramic targets for laser ablation involves grinding

and pressing of the powders followed by calcination to remove volatile impurities. This is followed by sintering of the pressed pellets, often repeatedly to obtain a high density and mechanically robust target. A sintering temperature of approximately 0.5–0.7 T melt is generally recommended to promote densification and to facilitate atomic diffusion throughout the target, but to prevent decomposition lower temperatures should be used [1].

Figure 2.3 shows the variation of resistivity, carrier concentration and Hall mobility of Si-doped ZnO films grown by pulsed laser deposition as a function of silicon content. It can be observed from Figure 2.3 that the resistivity decreased rapidly with increase of silicon concentration up to 2 wt%; thereafter the resistivity increased gently. The decrease in resistivity is because of the small amount of silicon provides a large number of free electrons in the film. When the silicon content is greater than 2 wt%, non conducting silicon oxide phase due to the extra silicon atoms is formed. Equilibrium between the silicon atoms contributing conduction electrons and those producing silicon oxides is reached. For very high silicon concentration, the conductivity would be expected to decrease again as a result of the large amount of non-conductive silicon oxide in the film.

Figure 2.3 illustrates that the carrier concentration first increases rapidly up to 2 wt% and then decreases for higher silicon concentrations. Up to 2 wt% silicon, it provides donors only, whereas above 2wt% silicon segregation at the grain boundaries also takes place.

It also can be observed from Figure 2.3 that mobility increases with an increase in silicon content, whereas decreases for the silicon content greater than 2 wt%. Silicon atoms in the films produce not only conduction electrons but also ionized impurity scattering centres. It may also occupy interstitial positions and deform the crystal structure. Scattering by the ionized impurities and defects in the crystal will result in a lower value of mobility. Such a behaviour has been observed by Aktarduzzaman *et al.* [26].

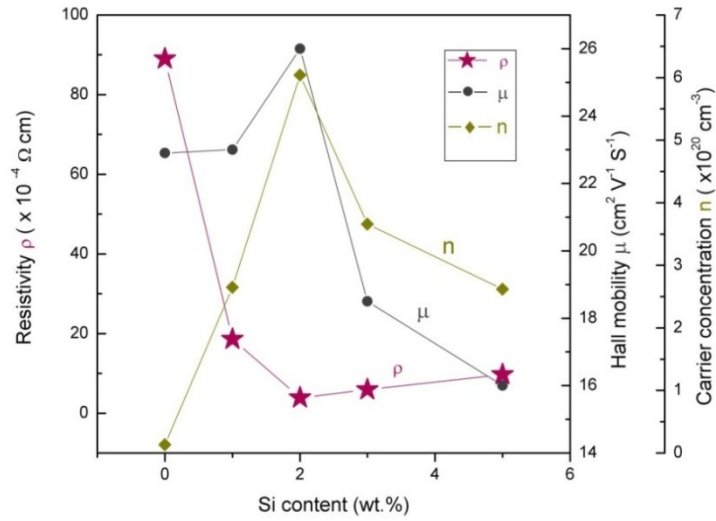
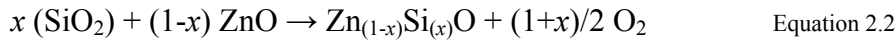


Figure 2.3 Dependence of carrier concentration (n), Hall mobility (μ) and resistivity (ρ) on silicon content (wt %) in ZnO films [28]

The possible reactions for formation of $\text{Zn}_{(1-x)}\text{Si}_{(x)}\text{O}$ is:



where x is the percentage of Silicon doping. The binary Zn_2SiO_4 compound exists in the SiO_2 – ZnO system. The melting point of the eutectic is 1,507 °C on the ZnO-rich side, and it is 1,432 °C on the SiO_2 -rich side

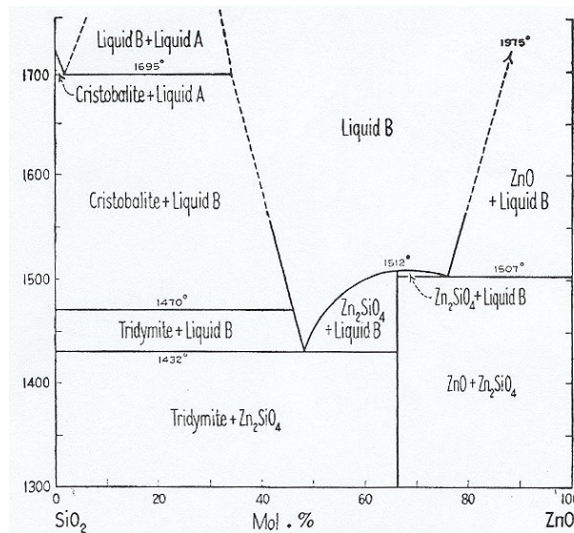


Figure 2.4 System ZnO-SiO (1930) Phase Diagrams for Ceramists. In Levin EM, Robins CR, McMurdie HF (eds) The American Ceramic Society, 1964, Fig. 302 (after Bunting EN, Phase equilibrium in the system SiO_2 – ZnO . J Am Ceram Soc 13(1):5) [29]

2.1.3.3 P-type Doping

It would be expected that the group I elements Li, Na, or K are superior acceptors on the Zn site [5, 30, 31]. Indeed Li, Na, K, and also the Ib elements Cu and Ag are recognized to form acceptors [4]. Several research currently focuses on p-type doping with the group V elements N, P, As and even Sb on O sites. After numerous inadequately reproducible results and other problems summarized by, e.g. Look *et al.* [32], there were lately consistent reports on p-type doping in ZnO with N, As or P [5, 33-35].

2.1.4 Optical Properties of ZnO

Most of the applications of ZnO films are certainly related to its optical properties. Since the band gap energy of ZnO is 3.37 eV at room temperature, it is transparent in both the visible and near ultraviolet-visible wavelength region. The exciton binding energy is quite high (60 meV), and it luminesces in the ultraviolet (UV) region (around 380 nm) making ZnO a possible future contender for UV and blue-light-emitting devices. This large exciton binding energy permits excitonic recombination above room temperature, and, as a result, optically pumped lasing has been observed in epitaxial or polycrystalline ZnO thin films [36, 37].

The optical absorption coefficient α can be calculated through $I = I_0 e^{-\alpha t}$, where I and I_0 are the intensity of transmitted light and incident light, correspondingly, and t is the film thickness, bearing in mind that the thickness of the films studied vary significantly. In the direct transition semiconductor, α obeys the following relationship with optical energy band gap

$$\alpha \propto C (h\nu - E_g)^{1/2}, \quad \text{Equation 2.3}$$

where h is Plank's constant, C is a constant, and ν is the frequency of the incident photon [38].

Figure 2.5 shows the plot of $(\alpha h\nu)^2$ vs. $h\nu$ (photon energy) for ZnO-In₂O₃ films as a function of doping level. The optical band gap is determined by the extrapolation method.

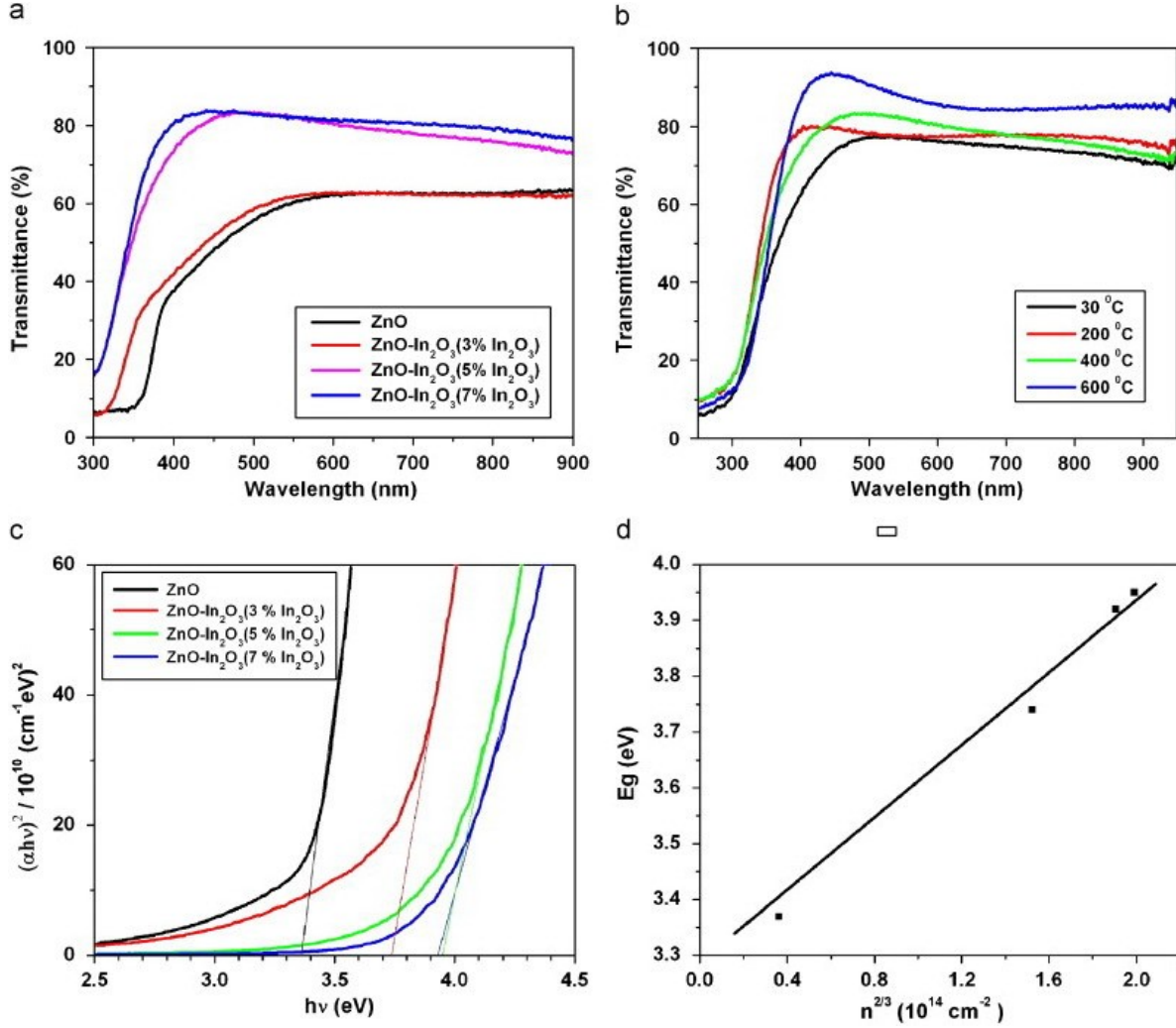


Figure 2.5 Transmittance spectra of ZnO–In₂O₃ films as a function of doping level (a), and substrate temperature ZnO– 5% In₂O₃films (b). (c) Plot of $(\alpha hv)^2$ against $h\nu$ of ZnO– In₂O₃ films as a function of doping level. (d) Plot of band gaps (E_g) as function of $n^{2/3}$ (n being the carrier concentration) for ZnO– 5% In₂O₃films [39].

This shift of the optical band gap of TCO films by varying growth conditions can be explained by the Burstein-Moss model [40, 41] due to the different carrier concentration of these films. They explained that the band gap would rise with increasing carrier concentration. The Burstein-Moss shift ΔE_g is given by

$$\Delta E_g = \left(\frac{h^2}{2m_{vc}^*} \right) (3\pi^2 n)^{2/3} \quad \text{Equation 2.4}$$

Where ΔE_g is the shift of the doped semiconductor with respect to the undoped semiconductor, m_{vc}^* the reduced effective mass ($1/m_{vc}^* = 1/m_c^* + 1/m_v^*$: $m_c^* = 0.38m_0$ and $m_v^* = 1.8m_0$), n carrier concentration and h is the Plank's constant [42]. Figure 4.23, according to this equation shows that, the band gap increases with increasing carrier concentration.

2.2 ZnO Thin-Film Growth by PLD

2.2.1 Pulsed Laser Deposition (PLD)

Pulsed laser deposition is often described as a three-step process consisting of vaporization of target materials, transport of the vapour plume, and film growth on a substrate. These three steps are repeated thousands of times during the deposition. Laser pulses seldom remove material in a layer-by-layer and clean style. Instead, target surfaces become malformed both chemically and physically. Morphological changes catch the shape of periodic structures like ripples, ridges, and cones [43]. A basic thermal cycle is illustrated in Figure 2.6.

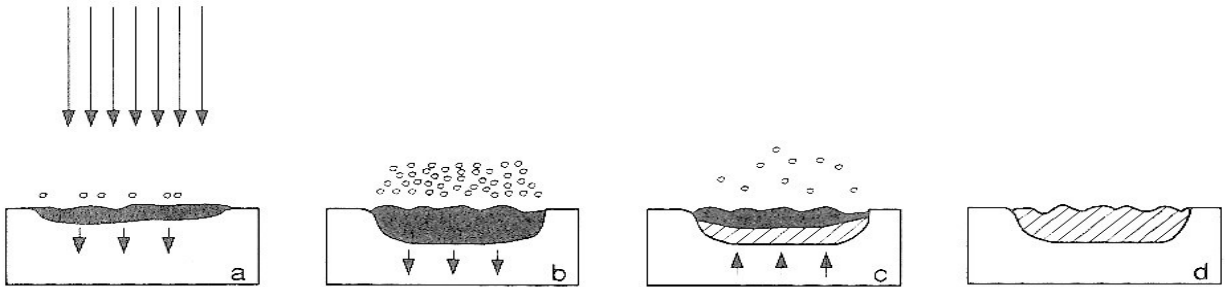


Figure 2.6 Schematic of the basic thermal cycle induced by a laser pulse. (a) laser pulse is absorbed, melting and vaporization begin (melted material showed by shaded area, arrows indicate motion of the solid-liquid interface). (b) Melt front propagates into the solid, accompanied by vaporization. (c) Melt front recedes (cross-hatched area indicates resolidified material). (d) Solidification complete, frozen capillary waves alter surface topography. The next laser pulse will interact with some or all of the resolidified material [43].

There are few intrinsic restrictions placed on the targets used in a PLD system. Targets can be in various forms such as sintered and pressed powder pellets, single crystals, cast material, and metal foils. The main distinction between these various target morphologies is in the creation of particulates and the nature of the target erosion. The best films can be produced by high-density and highly homogeneous targets. However, all the targets should be sanded flat after each

deposition or at regular intervals to retain their optimum performance levels. In terms of uniform target erosion, the target should be rotated during the deposition.

The laser beam may also be scanned over the surface to provide uniform erosion. The disc-shaped targets are generally mounted by silver paste onto a target holder in order to achieve good thermal contact between target and mount [43].

2.2.2 Advantages of PLD for ZnO Films

PLD supplies a number of advantages compared to the other thin film growth techniques. The composition of the target used in PLD and the grown films are quite close. PLD films crystallize at lower substrate temperatures proportionate to other physical vapor deposition (PVD) techniques as a result of the high kinetic energies of the ejected atoms and ionized species in the plasma (>1 eV) [44]. Due to the low crystallization temperature, some researchers reported the growth of ZnO films on flexible substrates at low temperatures, which is necessary for production of flexible flat-panel displays [45-47]. Another advantage of PLD for the growth of ZnO films is an extremely smooth film surface compared to films grown by other physical vapor deposition techniques [48].

2.2.3 Optimum PLD Conditions for ZnO Films

The first researches upon laser sputtering of ZnO were employed using a tunable dye laser by Nakayama *et al.* [49, 50]. PLD of ZnO films was reported for the first time using a pulsed CO₂ laser to evaporate a ZnO target [51]. ZnO films were smooth, transparent, and highly textured with the (002) planes parallel to the substrate, indifferent to the type of substrate. Films deposited at low oxygen pressure had lower resistivity than those deposited at oxygen pressure about 10^{-2} mbar which were found to be highly insulating.

Using the KrF laser (248 nm) was a major step in the development of the PLD of ZnO. Ianno *et al.* [52] reported the optimum laser fluence of $2-3$ J/cm² for the deposition of ZnO films, while the oxygen pressure should be around $2-3 \times 10^{-3}$ mbar to achieve low resistivity and highly

oriented films, dependent on the target–substrate distance used. Employing a KrF laser 248 nm PLD system, Craciun *et al.* [53, 54] deposited high-quality ZnO films on glass and silicon substrates and studied the effect of the deposition parameters, such as oxygen pressure, substrate temperature and laser fluence, on the properties of the grown films. The electrical resistivity of the films was strongly dependant to the oxygen pressure due to the controlling influence of Zn interstitials or O vacancies on electrical conductivity of ZnO films.

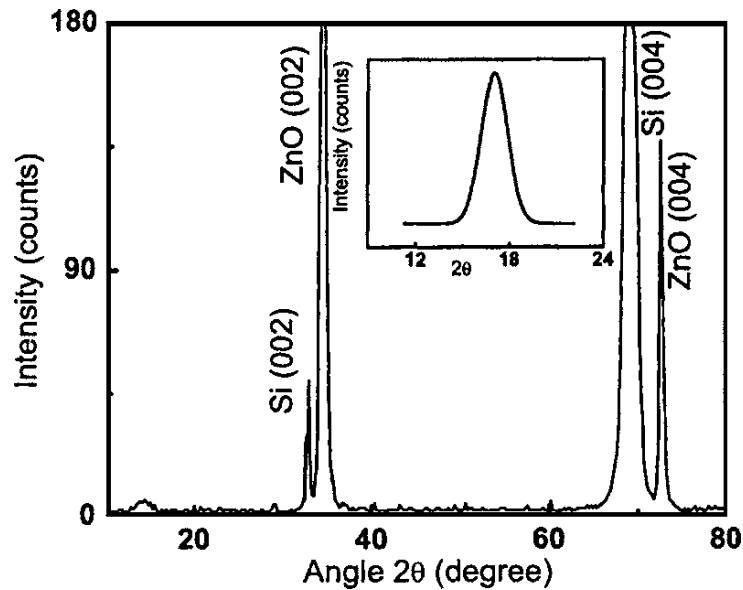


Figure 2.7 XRD pattern of a ZnO thin film deposited under optimized conditions (KrF laser 248 nm, fluence 2.1 J/cm^2) on a Si substrate at 350°C under an oxygen pressure of 2.5×10^{-3} mbar. The rocking curve recorded for the (002) line is shown in the inset [54].

Figure 2.7 illustrates that, ZnO films deposited at these conditions with a substrate temperature of 350°C , oxygen partial pressures from 1 to 3 mTorr, and a laser fluence of around 2 J/cm^2 , exhibited a full-width at half-maximum (FWHM) of the rocking curve around 2° at 16.99° . The film deposited at these conditions showed transparency of above 85% in the visible region of the spectrum [54].

Among the doped ZnO films with Group III elements such as barium, aluminium, indium, and gallium, aluminium-doped ZnO (AZO) films exhibit the lowest electrical resistivity [55, 56].

AZO films have low resistivity of $1-4 \times 10^{-4} \Omega\text{cm}$ [55, 57], which is similar to that of ITO films [58].

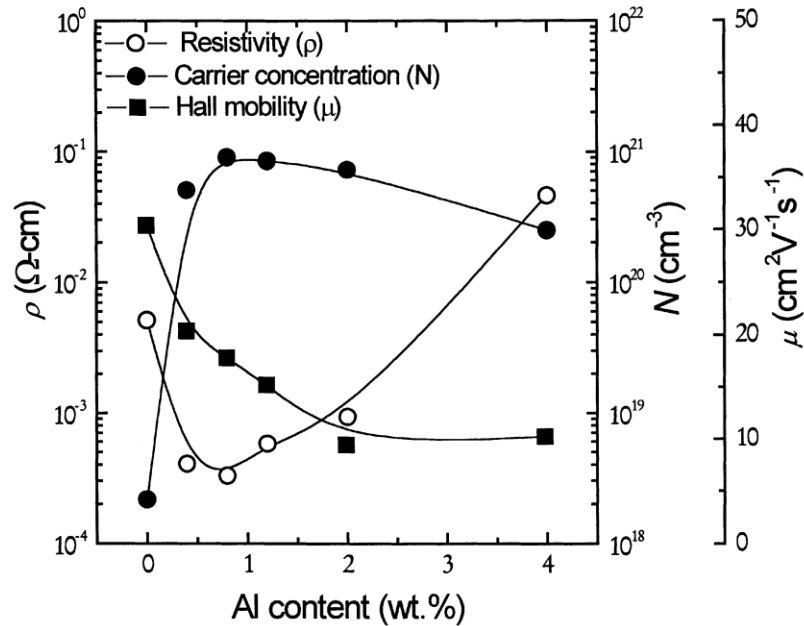


Figure 2.8 Dependence of electrical resistivity, carrier density and Hall mobility on the Al content in the targets used to deposit the AZO films. All films were deposited at 200 °C in 5 mTorr of oxygen [59].

Figure 2.8 shows the typical variation of resistivity, carrier concentration and Hall mobility of Al-doped ZnO films grown by pulsed laser deposition as a function of Al content. It can be observed from Figure 2.8 that the resistivity decreases initially with increase of Al concentration up to 0.8wt%; thereafter the resistivity rises slowly with a further raise in the Al content up to 4wt%. The initial increase in carrier concentration is because of the incorporation of Al ions in interstitial positions or the replacement of Al^{3+} ions at Zn^{2+} cation sites. When the Al content is greater than 0.8 wt%, non conducting Al_2O_3 clusters due to the extra Al atoms is formed causing crystal disorder. It's also clear from Figure 2.8 that the Hall mobility of the AZO films reduces with rising Al content. This decrease in mobility is also due to the observed reduction in grain size of the Al-doped ZnO films [26, 57, 59].

Effect of oxygen pressure on the surface morphology of ZnO films was examined in Kim and Lee's work [60]. The film grown at the high O₂ pressure of 5×10^{-1} Torr consisted of much larger grains and exhibited a rougher surface than the film grown at 5×10^{-4} Torr (Figure 2.9). More oxygen is incorporated into the ZnO film lattice when increasing the O₂ pressure. Film lattice is more likely to expand, when oxygen is markedly incorporated as a result of high O₂ pressure. Crystallinity of the film may be also influenced during deposition by the kinetics of atomic arrangement.

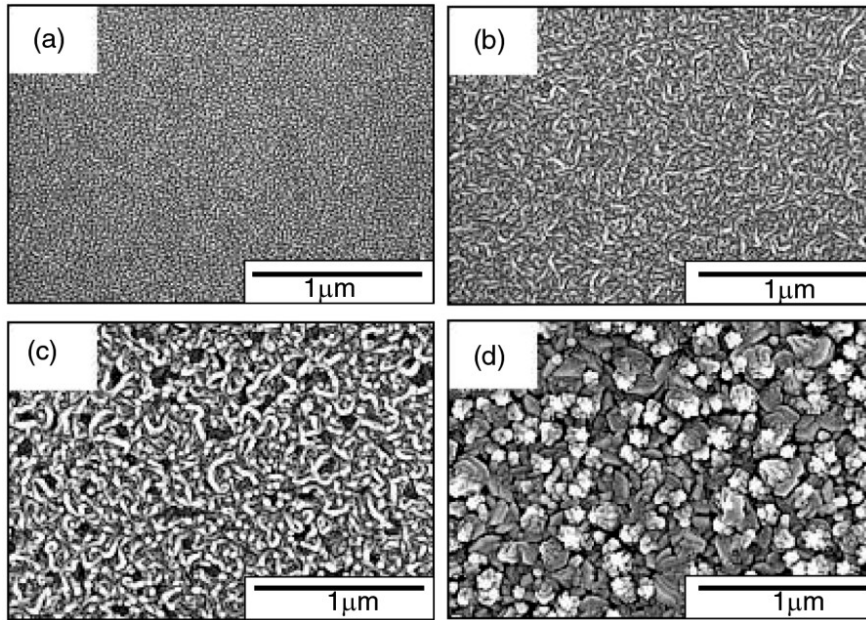


Figure 2.9 SEM images of the pulsed laser deposited ZnO films grown at various oxygen pressures: (a) 5×10^{-4} ; (b) 5×10^{-3} ; (c) 5×10^{-2} and (d) 5×10^{-1} Torr [60].

Kim *et al.* reported that the resistivity decreased rapidly as the oxygen pressure was decreased from 6.6 to 0.66 Pa. because of a raise in the number of oxygen vacancies in the films which brought about a raise in the carrier concentration and a fall in resistivity of the films. However the raise in carrier concentration also produces a fall in the optical transmittance owing to a raise in free carrier absorption. Minimum resistivities of $3.9 \times 10^{-4} \Omega \text{ cm}$, $4 \times 10^{-4} \Omega \text{ cm}$ were obtained for the Al-doped and Ga-doped ZnO films [61].

When studying the effect of substrate temperature on the resistivity of Al doped ZnO films, Matsubara *et al.* [62] recorded that, as the substrate temperature increased from room

temperature to 550°C the resistivity also rose from $3 \times 10^{-4} \Omega\text{cm}$ to $6 \times 10^{-4} \Omega\text{cm}$ and for higher substrate temperatures, the carrier concentration was reported to be lower. This might be due to the incorporation of excess oxygen into the film at the higher substrate temperatures. This was confirmed by the fall in mobility that was obtained at 550°C, with the suggestion that the overload oxygen existed at grain boundaries and thus formed an electrical obstacle.

Optical transmission is of great significance in display screen applications, and is influenced by both temperature and pressure. The effects of pressure and temperature on optical properties basically disagree. As oxygen pressure rises, carrier concentration is seen to fall resulting in a raise in optical transmittance [18] but as temperature rises carrier concentration also increases, but is coordinated by a raise in transmission. It can be implied that an increase in temperature decreases point defects. Such defects can be responsible for scattering photons and resulting decreased transmission. Increased temperature also improves the stoichiometry and, as such results in increased transmission. Increased temperature will lead to increased oxygen absorption which will predictably improve stoichiometry through the elimination of oxygen vacancies.

Based on the work by Ismail [63], as oxygen pressure enhanced, film thickness fell due to increased collision of the deposited ZnO particulates during deposition with oxygen. Rao *et al.* [64] observed that the crystalline quality of the films improved and the grain size increased as the thickness increased. It was attributed to decreased tensile strain as thickness increased.

Chrissey [44] found that in pulsed laser deposition of thin films, as the pressure increased, the number of particles found in the ablated film rose. This was ascribed to condensation of the flux before impact on the substrate. The mean free path at a pressure of 1 mTorr was established to be around 5 cm, at a pressure of 100 mTorr decreasing to 0.05 cm. Therefore, if high pressure depositions are essential then a very short target-to-substrate distance would be necessary to minimize the number of particulates in the grown film. This would propose that more smooth surface morphology can be achieved by grown at lower oxygen ambient pressures at a constant target-to-substrate distance. The mean free path also has an influence on film thickness. The collision of plume particles forms the particulates, but these are not the only condensations that may happen during ablation.

Dong *et al.* [38] suggested that the surface morphology of AZO transforms from hillocky to cratered with increase in film thickness. The hillocky appearance was attributed to the vertical growth of grains for films thinner than 100 nm. However, when the thickness was more than 120 nm, the crystal grains tended to grow laterally. The growth mode transition was attributed to the reduction of interfacial stress in the grains with the increase in thickness.

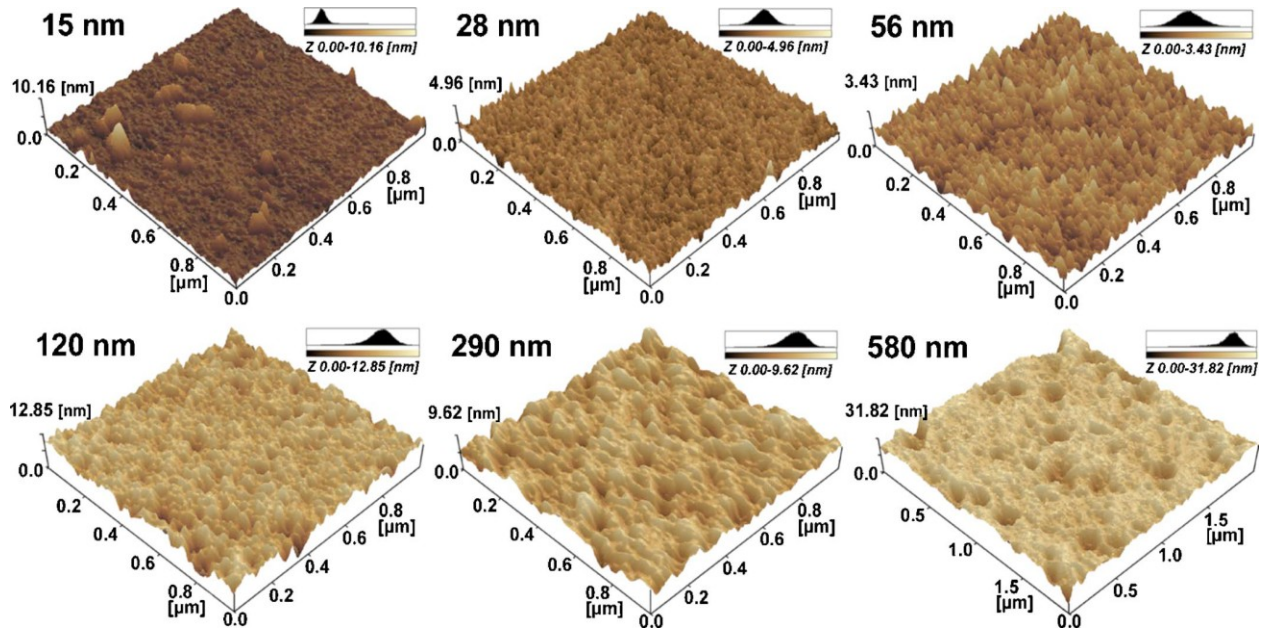


Figure 2.10 AFM images of AZO films with different thickness. The height distribution of corresponding AZO surface is displayed at right top of every image.

2.3 Other Thin Film Fabrication Methods

Various deposition techniques such as CVD [65-67], Spray pyrolysis [68-70], sputtering [71-73], evaporation [74, 75], etc can be employed for the growth of ZnO films. The significant features related to these diverse techniques are as follows[7]:

- (i) Spray pyrolysis can be used to grow low-cost films for large-area applications where uniformity is not the most important obligation.

(ii) Ion-assisted growth technique is mainly appropriate for deposition on polystyrene-like materials where substrate heating is not achievable.

(iii) Sputtering and chemical vapour deposition (CVD) have been extensively used to grow reproducible device quality films as they permit better control of film composition and thickness especially in sputter deposition technique.

(iv) Techniques, for instance vacuum evaporation, dip coating and electroless deposition are only of academic interest.

2.4 Applications of ZnO Films

There is an expanding demand for TCO materials in the field of flat-panel displays including liquid crystal displays (LCD) and organic light-emitting diodes (OLED). Few studies have focused on developing new anode materials like ZnO as alternatives to ITO for OLED devices [76-81]. The Al-doped ZnO (AZO) films grown by PLD have also been used as an anode contact to fabricate OLEDs [57]. The Zr-doped ZnO (ZZO) films grown by PLD have been productively used as an anode material for OLED devices [76].

In another work, Masuda *et al.* has used ZnO as an active channel layer in a transparent thin-film transistor (TFT) that can operate in the presence of visible light [82]. An attractive point associates to PLD-grown (002)-oriented ZnO films on amorphous substrates. Such textured films on fused silica substrates were used as alignment layers for the growth of c-axis oriented GaN films [83]. Besides, in the production of photonic devices, these semiconducting ZnO buffer layers can also be employed as transparent electrodes for GaN. A great deal of work has been implemented on the photoluminescence properties at 1.54 μm of Er-doped semiconductors [1]. However, the low efficiency of luminescence at room temperature prevents any real applications. The optical properties of Er-doped ZnO have, therefore, been studied [84, 85] considering light wave communication devices such as LEDs, laser diodes, or optical amplifiers.

3 Methodology

3.1 Pulsed Laser Deposition (PLD)

Transparent conductive SZO films were prepared by pulsed laser deposition on borosilicate glass, silicon and sapphire substrates of thickness 1.1 mm by pulsed laser deposition of a ZnO target doped with 2wt % silicon. Usual substrate size is 10×10 mm, in order to match the sample size limit for some measurements like AFM, Hall measurements and etc.

The Target was radiated at high temperatures at low ambient oxygen pressures by a laser beam (energy of 90-240 mJ). The laser source was a KrF excimer laser (Lambda physics LPX 300), which emitted pulses with frequency of 10 Hz at a wavelength of 248 nm (0.18 ns in length).

12 different powders from Zinc oxide (purity, 99.99%) and 0-8 wt.% SiO₂ (purity 99.99%) were studied to increase the solubility of Si in the target. Powders were mixed in acetone and then fired at 800°C or 1100 °C in Ar or air for 8-hour period, ground, and fired at the same temperature for a further 8 hours in the same atmosphere. Finally, the powder 2wt% Si-doped ZnO calcined for 8 hours at 750°C in air, ground and calcined 8 hours at 850°C in air, was chosen to make disk-shaped targets, 25 mm in diameter with 2 mm thick by standard pellet press (10-25 ton), and then sintered at 800°C for 6 hrs in air to produce mechanical strength in the target. A full description of the target preparation is contained in the Appendix.

The SZO films were produced by ablating a ZnO target containing 2 wt.% SiO₂, onto a borosilicate glass and Si substrate placed simultaneously at 70, 60 and 50 mm away from the target. Films were grown typically with 5000 laser shots and a repetition rate of 10 Hz. Before the growth process, the substrates were prepared for deposition, rinsed in an ultrasonic bath using hydrochloric acid (35%), acetone, ethanol, and finally distilled water. Substrates were dried in flowing air before mounting. The substrates were mounted on the substrate heater using silver paint (Agar scientific Ltd) to make sure a good thermal contact. The deposition chamber was

primarily evacuated to 10^{-6} mTorr using a turbo molecular pump which takes up to 6 hours to reach that pressure and then oxygen gas was introduced into the chamber. The pressure can be controlled at fixed temperature. The target was pre-ablated by 1000 pulses if the deposition was the first usage of that target and 500 pulses for used target to decrease the probability of sample contamination, followed by the number of chosen ablation pulses. During both the pre-ablation and ablation, the target was rotated at 29°s^{-1} , moving 10° about the beginning position with a raster velocity of 10°s^{-1} . After ablation samples were allowed to cool down to 60°C at the deposition pressure before removing from the chamber.

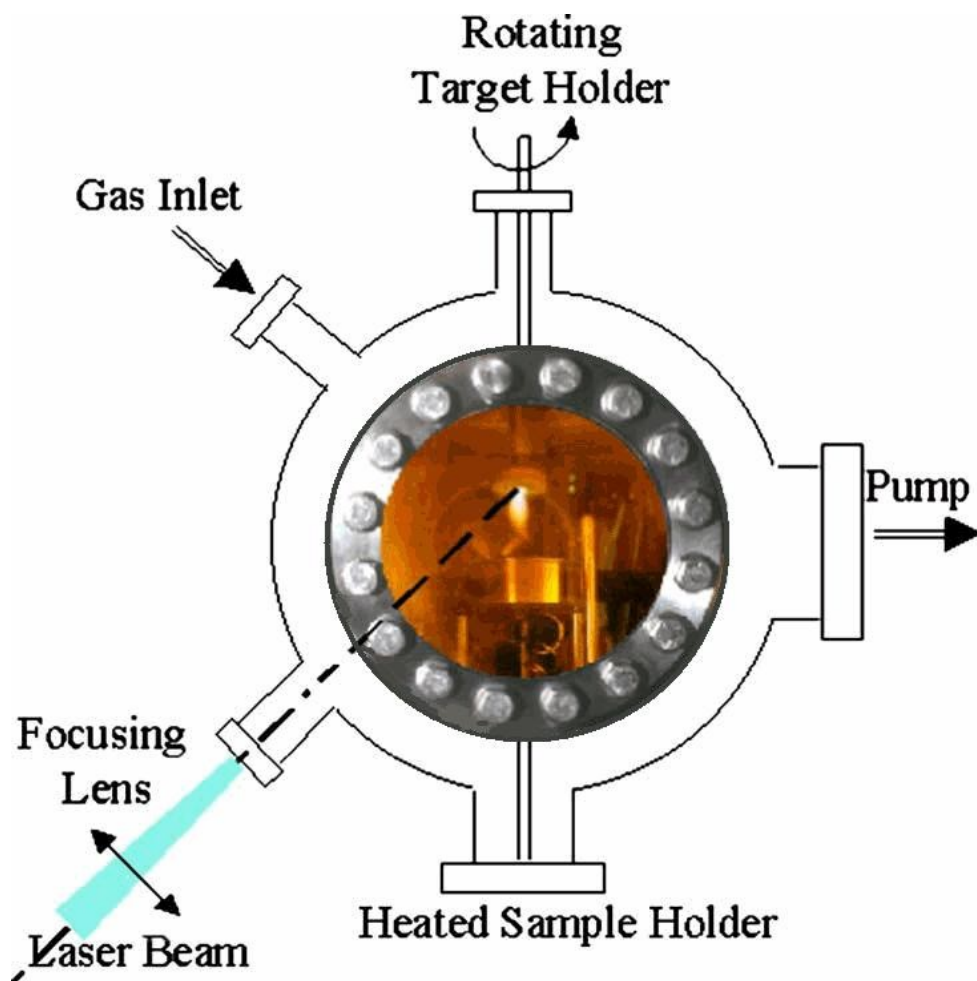


Figure 3.1 A schematic of pulsed laser deposition chamber [86]

3.2 X-ray Diffraction (XRD)

X-rays are a radiation source with wavelengths which interact with crystals containing symmetrical arrays of atoms within rows or planes to form constructive and destructive interference, i.e. diffraction results. This occurs when X-rays of a specified frequency hit an atom, leading to an interaction with its electrons causing them to vibrate with the same frequency as the incident X-ray beam. This results in the vibrated electron radiating the X-ray with no change in its frequency, in all directions. Diffraction occurs within favourable orientated planes of atoms according to Bragg's law [14]:

$$n\lambda = 2d \sin \theta \quad \text{Equation 3.1}$$

Where d is the vertical spacing between planes of atoms, λ is the wavelength of the source, n is an integer and θ is the angle of the incident radiation.

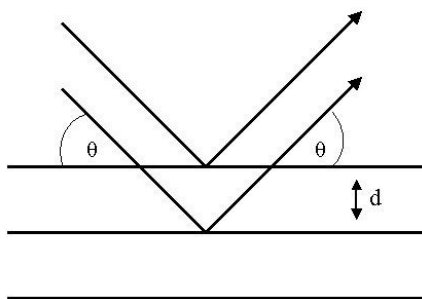


Figure 3.2 Interaction of x-rays with planes of atoms

Using monochromatic Cu-K α of wavelength 1.54 Å, diffraction patterns for each sample were measured by X-ray diffraction. A tube current of 40 mA was utilized, with a tube voltage of 40 kV. Rocking curve of each sample was obtained from the 2 θ scan (2 θ =20-100°) with scan step size of 0.02° using a Philips Xpert set for 2 θ scan.

3.3 Atomic Force Microscopy (AFM)

Atomic force microscopy (AFM) is predicated on mapping local variations in the intermolecular and interatomic forces between the tip and the sample being scanned [87]. In AFM, a typically pyramidal silicon nitride tip is positioned over a sample. The relative motion between the tip and sample is controlled by a piezoelectric scanner. The reflection of a laser focused onto the back of the AFM tip is monitored on a four-quadrant position sensitive photodiode (PSPD). As the AFM tip is raster-scanned over the sample surface, variations in tip-sample interactions result in (vertical and lateral) deflection of the tip. This deflection is reflected in movement of the laser spot on the PSPD and is used to produce a three-dimensional topographical image of the surface [88].

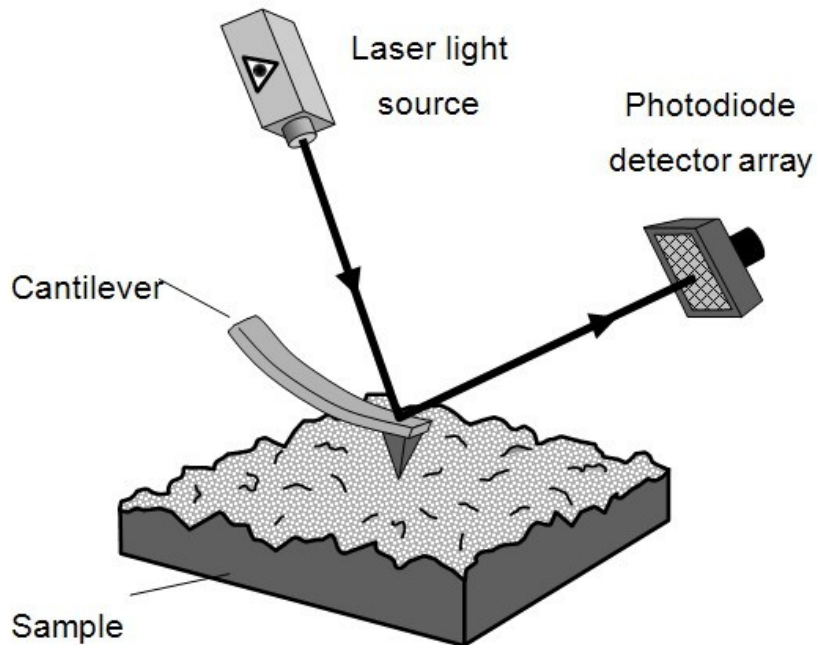


Figure 3.3 An AFM probe raster-scan over a sample surface

There are three different classes of AFM: contact mode, tapping mode and non-contact mode. Usually, surface morphology was investigated by contact and tapping mode on ZnO thin films. The typical resolution of the images is 5 to 10 nm, depending on the sample material.

Contact AFM— Measures topography by sliding the probe's tip across the sample surface and operates in both air and fluids.

Tapping Mode™ AFM— Measures topography by tapping the surface with an oscillating tip. This eliminates shear forces which can damage soft samples and reduce image resolution. Tapping Mode is available in air and fluids

3.4 Scanning Electron Microscope (SEM)

In scanning electron microscopes, a beam of highly energetic electrons is used to study objects on a very small size. In a SEM, when a sample is struck by an electron beam, generates a large number of signals. Secondary electrons are formed when an incident electron strikes an electron in the sample and loses part of its energy in the procedure. The excited electron travels to the sample surface and, if adequate energy remains, the surface will be excited and is called a secondary electron (non-conductive can be coated with a conductive material to increase the number of the secondary electrons that will be emitted with energies less than 50 eV). In this study, a scanning electron microscopy (JEOL 7000) equipped with energy dispersive X-ray. According to the microscope specifications, resolution up to 3.5 nm (in high vacuum mode) are ensured, while magnification is reported to be in the range of 8X - 300,000X; though, these data is dependant on the characteristic of each sample, it can be different depending on the sample components like samples with heavier elements lead to obtaining much more accurate analysis.

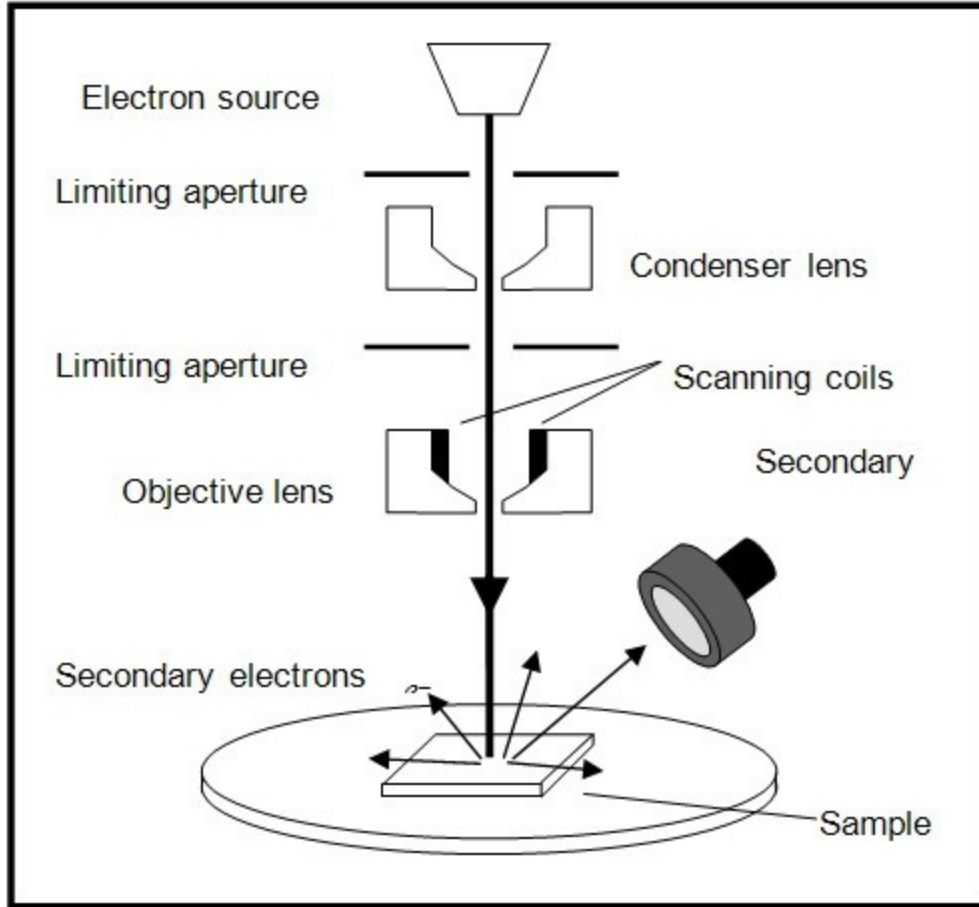


Figure 3.4 Schematic diagram of an SEM set-up [88]

3.5 Thickness Measurement

The thickness of SZO thin films were measured by three methods:

3.5.1 Film Thickness Measured Using an Optical Laser Microscope

Film thickness measurements were collected using an Olympus LEXT OLS3100 mounted on a anti-vibration table. The microscope uses a 408 nm class II ultra-violet laser source and has a plane resolution (X & Y) of 120 nm and a space pattern (Z resolution) of 10 nm. First it was focused on the outer surface, then the lower surface. Using the refractive index found in literature for ZnO thin films, the distance between the 2 surfaces was calculated.

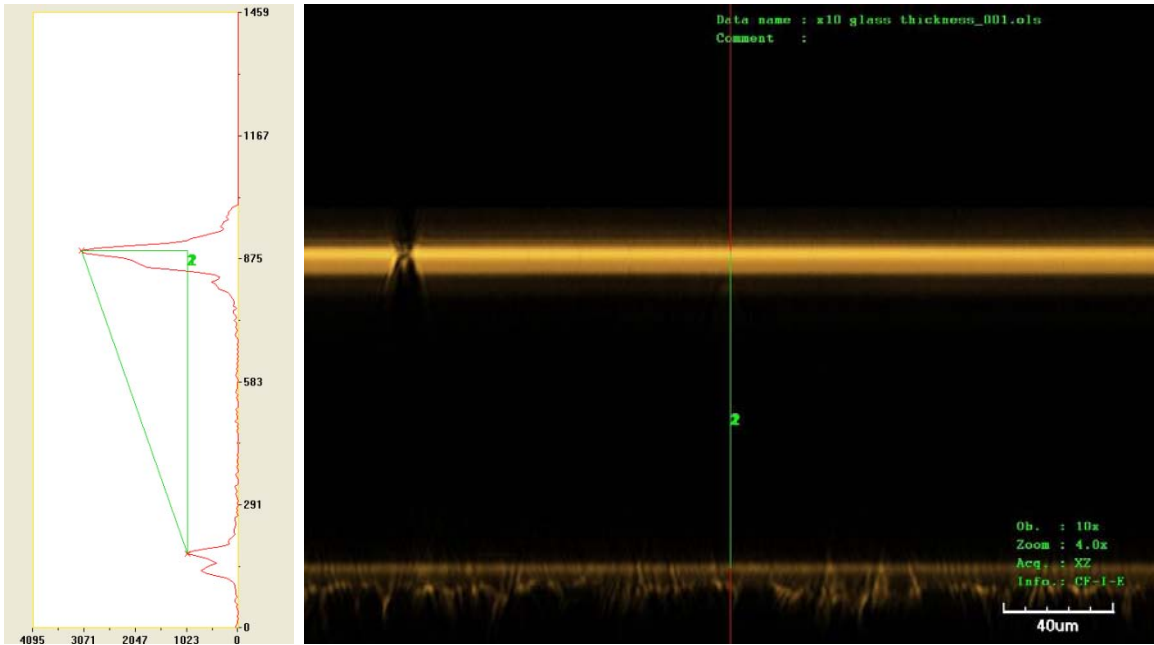


Figure 3.5 Thickness measurement using an optical laser microscope. Based on the reflection of the inner and outer surface of the film, the distance between the 2 surfaces was calculated.

3.5.2 Film Thickness Measured Using an Ellipsometer

An ellipsometer enables the measurement of the thickness of semi-transparent films. A multi-spectroscopic ellipsometer was employed that emitted light from a xenon bulb of wavelengths 250-800 nm at 10nm intervals. Ellipsometer is dependant on the statement that the polarization of light causes the reflection at a dielectric interface while the transmission of light through a transparent sample alters the incoming wave's phase conditional on the material's refractive index [89].

3.5.3 Film Thickness Measured Using SEM

Thickness can be measured by breaking the samples and coating with gold for nonconductive substrates. SEM micrographs of the cross-section for SZO films were obtained at a tilt angle of 80 degrees where the sample was mounted with the surface of the film on top using silver paint.

3.6 Optical Transmittance

Optical transmission measurement of the Si-doped ZnO on borosilicate glass substrates were carried out using a Unicam UV 500 UV-Visible spectrophotometer. Ultraviolet and visible light can cause electronic transitions. When a molecule absorbs energy, it excites an electron into a higher empty orbital. Therefore energy absorbance can be plotted versus the wavelength to obtain a UV-Visible spectrum. Both the shape of the peak(s) and the wavelength of the maximum absorbance (λ_{max}) give information about the structure of the sample. UV light has a wavelength of 200~400 nm and visible light has wavelengths of 400~800 nm. Also the optical band gap can also be ascertained from the spectra graph. The wavelength was varied between 320-1000 nm at 1nm intervals. The optical band gap dependence of the absorption coefficient α is given by the following equation:

$$(\alpha h\nu)^2 = A(h\nu - E_g) \quad \text{Equation 3.2}$$

where A and E_g are constant and optical band gap, respectively. The extrapolations of the linear part of the curve to the $h\nu$ axis can determine the E_g [39]. The absorption coefficient (α) was determined from:

$$I = I_0 \exp(-\alpha t) \quad \text{Equation 3.3}$$

Where I is the transmitted intensity at a particular wavelength, t is the thickness of the film and I_0 the maximum transmitted intensity (assumed to be 100%).

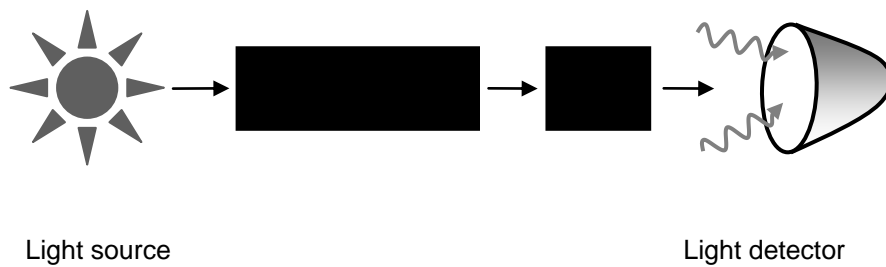


Figure 3.6 Block diagram of a spectrophotometer [88].

3.7 Electrical Measurements

3.7.1 Hall Effect

To determine the carrier concentration and carrier mobility, Hall measurements are required in combination with electrical conductivity measurements.

The Hall Effect was discovered in 1879 by Edwin Hall [90] and it refers to the potential difference that occurs across an electrical conductor by applying a magnetic field perpendicular to the electrical current flow. Resistivity and Hall Measurements were made by the van der Pauw method [91, 92]. Samples were mounted on a board and attached at 4 contacts by soldering.

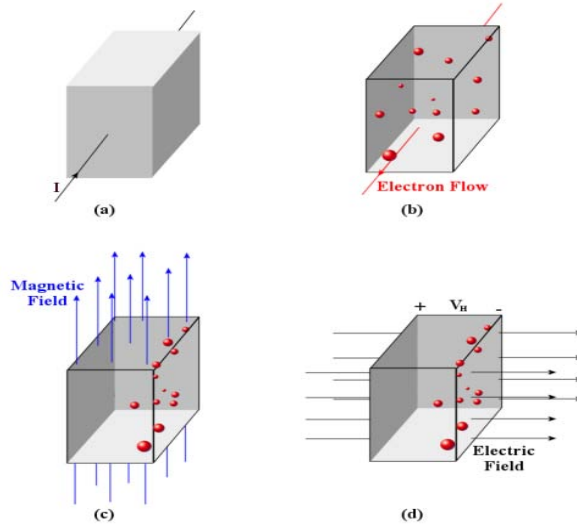


Figure 3.7 The Hall effect as it is used for the van der Pauw method. (a) - a current flowing through a piece of semiconductor material, (b) - the electrons flowing due to the current, (c) - the electrons accumulating at one edge due to the magnetic field, and (d) - the resulting electric field and Hall voltage V_H (Appendix shows more information) .

3.7.2 Four-Point Probe:

Using a Hall Four-Point measurement probe, electrical resistance of each sample was obtained. Six resistance readings were noted at 1 mm divisions about the middle of the sample. The resistivity of the sample was measured by taking average of these 6 readings using the formula below:

$$\rho = Rt \frac{\Pi}{\ln 2} \quad \text{Equation 3.4}$$

Where t is sample thickness (cm) and R is the calculated average resistance (Ω) for each sample.

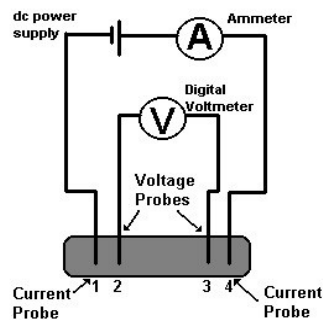


Figure 3.8 Schematic of Four-Point Probe [93].

4 Results and discussion on SZO depositions

4.1 Effect of PLD Conditions on Si-doped ZnO Films

The deposition parameters were varied to minimise the resistivity, and maximise the optical transparency. The substrate temperature and oxygen background gas pressure are typical deposition conditions that can be easily controlled during deposition to obtain Si-doped ZnO (SZO) films with high electrical conductivity and optical transparency. Other PLD parameters that are under experimental control are film thickness (number of pulses) and varying the target-to-substrate distance. From previous work done on the same PLD equipment, the optimized deposition circumstances were found to be at a substrate temperature of 300°C and an oxygen pressure of 5 mTorr [94]. The full details of SZO target preparation and other deposition conditions, such as incident energy and other substrate material can be found in the Appendix.

4.1.1 Influence of Substrate Temperature on SZO Films

The substrate (borosilicate glass) temperature is found to have a significant effect on the electrical and optical properties of ZnO films doped with Silicon. Several researchers have studied the influence of deposition temperature on ZnO and doped ZnO films [20, 95-98]. The decrease in resistivity with an increase in the substrate temperature can be explained by the fact that the grain size raises significantly with increasing growth temperature, thus decreasing the grain boundary scattering and increasing the conductivity. This increasing in grain size with increasing substrate temperature from room temperature to 300°C, also increases the optical transmittance in the visible range (400–700 nm). To study the dependence of SZO films on deposition temperature, all other deposition parameters were fixed; Table 4.1 shows the summary of SZO films grown by varying T_s .

Table 4.1 Summary of SZO deposition results by varying T_s (Target No. 4)

Target No.4 PO_2 (oxygen pressure)= 5 mTorr, D_{T-S} (Target-to-substrate distance) = 70 mm, E (incident energy) = 180 mJ, Number of pulses = 5000, 10 hz									
Substrate temperature °C	Thickness nm	Resistivity ρ ($\times 10^{-4} \Omega \text{ cm}$)	Hall mobility μ ($\text{cm}^2 \text{V}^{-1} \text{S}^{-1}$)	Carrier concentration n (cm^{-3})	Transparency %	002 height (a.u.)	FWHM	RMS (nm)	Crystal size (nm)
23	206	10.29	17.52	3.46E+20	76	908	0.58	0.11	14.28
150	208	7.02	19.05	4.27E+20	80.86	8945	0.34	1.69	24.15
250	216	6.53	20.8	4.6E+20	85	46888	0.22	1.44	37.96
300	220	4.12	23.86	6.35E+20	85.2	111218	0.20	1.78	40.76
350	245	4.8	26.32	4.94E+20	85.7	128655	0.20	1.81	42.44
450	275	36.01	7.01	2.47E+20	86	116248	0.22	2.78	37.65
500	194	60.02	6.51	1.60E+20	78.8	117350	0.21	3.82	40.19

4.1.1.1 Structural Properties of SZO Films by Varying Substrate Temperature

XRD patterns of SZO films (Figure 4.1) show clearly that crystallinity increases as substrate temperature (T_s) increases. As T_s is increased to 350°C the preferred orientation of (002) exhibits a further raise in the peak intensity, while the FWHM (full width half maximum) of the (002) peak decreases. When T_s exceeds 350°C, the film comes to be less oriented, with resulting decrease in the (002) peak intensity as well as a slight increase in FWHM. Shan *et al.* [99] observed the same trend indicating that the T_s is crucial. Low temperatures leads to low surface migration of adatoms, whereas, the high T_s re-evaporates the adatoms from the surface.

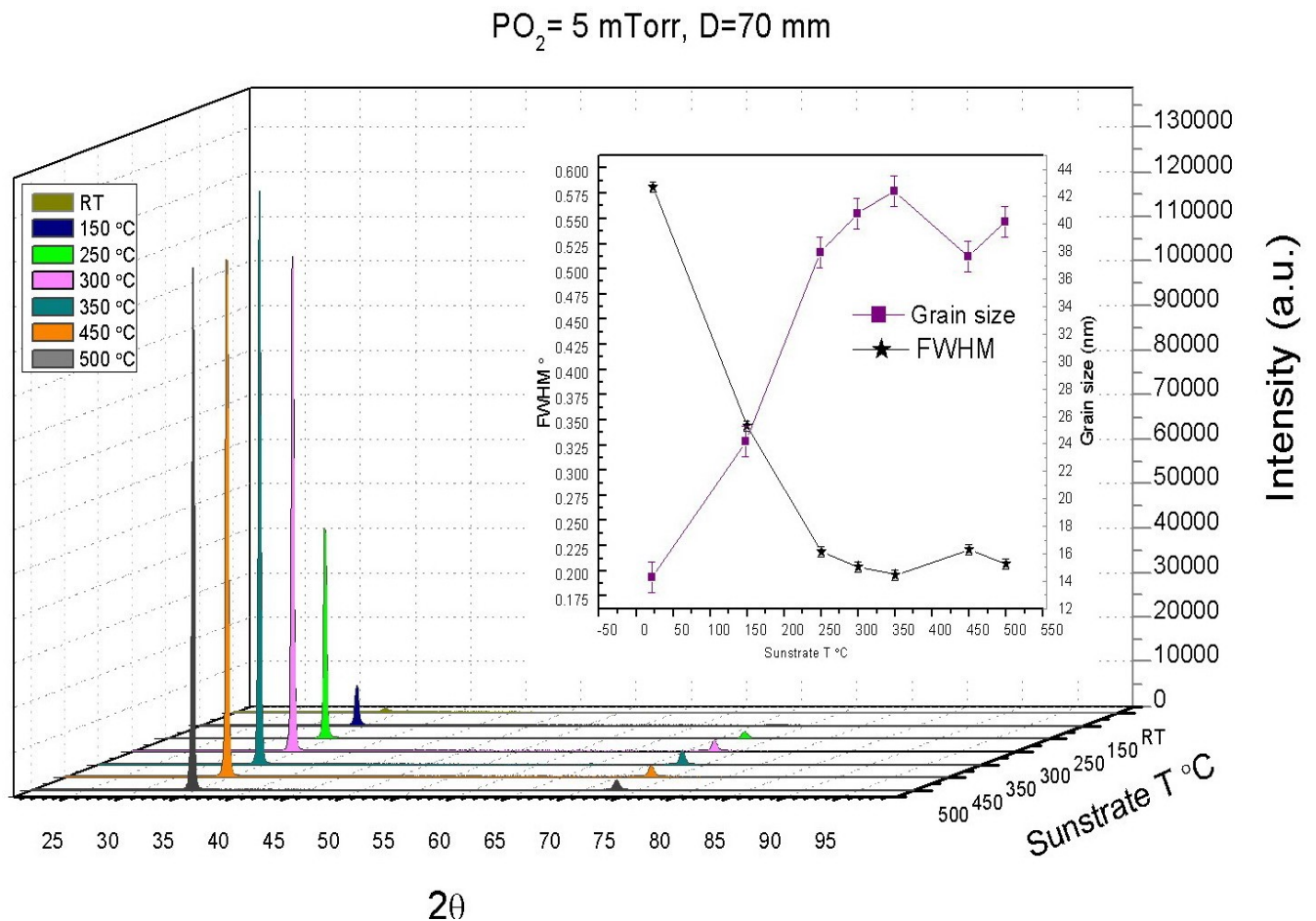


Figure 4.1 Variation of XRD pattern with substrate temperature for SZO films; the inset shows the dependance of FWHM (deg.) for (002) peaks and grain size (nm) of SZO films on substrate temperature; other used deposition parameters can be found in Table 4.1.

The (004) peak is identifiable at T_s higher than 250° . Figure 4.1 also indicates that all films deposited at T_s higher than 150°C have a polycrystalline structure, with (002) preferred orientation, while an amorphous nature can be seen for the film deposited at room temperature (RT). The XRD results indicate that the c-axis of the grains become uniformly at a 90 degree angle to the substrate surface at the optimized temperature. It is suggested that the surface energy of the (002) plane is the lowest in the ZnO crystal [14]. Because (002) plane has the minimum surface free energy, the surface of the ZnO films deposited onto amorphous substrates like glass tends to be (002) plane [12]. As the film deposition continues, grains with the lower surface energy become larger and the (002) crystallographic orientation develops, because it has the minimum surface energy.

This increase in intensity of the (002) peak also brings about a decrease in full width half maximum (FWHM) and an increase in the L , the mean size of the crystalline domains, which might be equivalent or smaller than the grain size calculated by the well known formula of Scherrer:

$$L = \frac{0.9 \lambda}{\beta \cos \theta} \quad \text{Equation 4.1}$$

where ' β ' is the experimental angular full width at the half maximum intensity (FWHM) of the peak. ' λ ' is the X-ray wavelength (1.5406\AA for Cu $K\alpha_1$) and ' θ ' is the Bragg's angle [14].

The temperature dependence of the film quality can be mainly interpreted by the particles mobility at diverse temperatures. At lower temperatures, the low mobility of the particles restricts the crystallisation of thin films as the low-surface-mobility particles will be sited at random orientations onto the substrate [100].

4.1.1.2 Electrical Properties of SZO Films by Varying Substrate Temperature

Silicon doped zinc oxide (SZO) films, like other transparent conducting films, show a dependence of electrical properties on substrate temperature. Figure 4.2 shows the dependence of resistivity, carrier concentration and Hall mobility on substrate temperature for Si-doped ZnO films prepared by pulsed laser deposition.

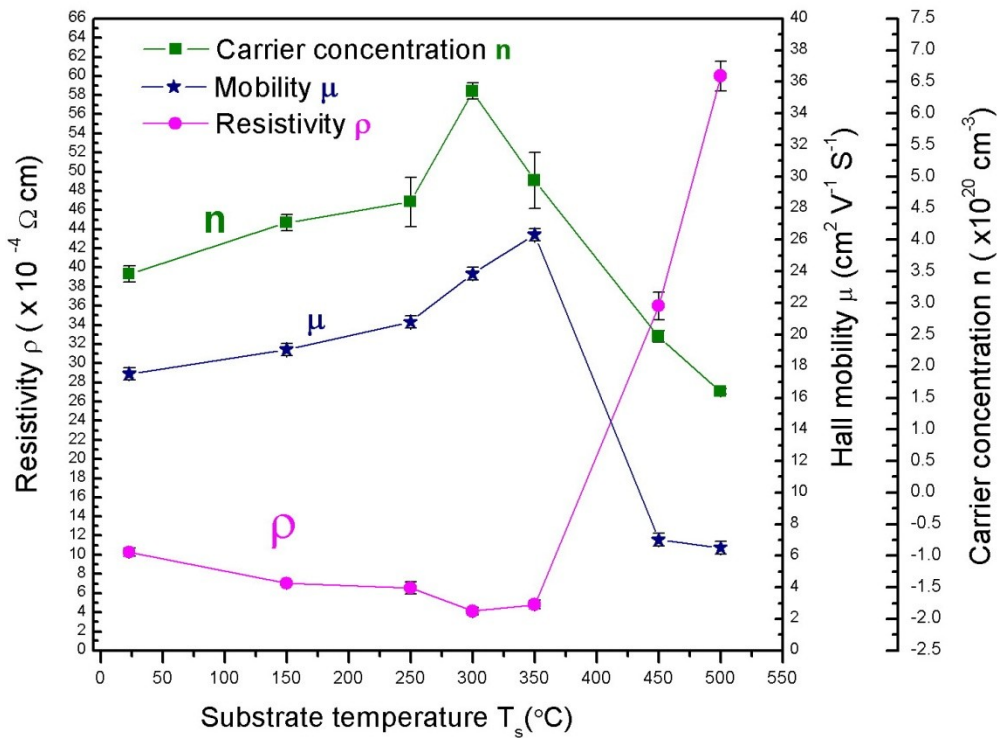


Figure 4.2 Variation of resistivity, carrier concentration and Hall mobility with substrate temperature for SZO films, deposition condition can be seen in Table 4.1.

It is clear from Figure 4.2 that resistivity decreases gradually to a minimum at 300°C, before increasing dramatically at 450 °C. The film of lowest resistivity, $4.12 \times 10^{-4} \Omega \text{ cm}$, was grown at a temperature of 300 °C. There is a slight difference between the resistivity of the films grown at 300 and 350 °C. The film of highest resistivity, $36.01 \times 10^{-4} \Omega \text{ cm}$ was grown at a temperature of 450 °C. When calculating resistance measurements, the result significantly incorporates any errors encountered whilst measuring thickness.

The gradual decrease in the value of resistivity with increase in substrate temperature up to 300°C is mainly related to the increase in mobility. The increase in mobility with increase in T_s up to 300 °C is due to an improvement in crystallinity in these films. This improvement in crystallinity has been confirmed using XRD studies shown above. The two predominant diffraction peaks of (002) and (004) reflections specify that the film has a preferred orientation along a c-axis direction normal to the sample's substrate. Figure 4.1 shows the dependence of intensity and full width half maximum (FWHM) of diffraction peak corresponding to (002) on the substrate temperature for SZO films. A similar behaviour has been observed by Park *et al.* [101] and Shan *et al.* [99] for Ga-doped ZnO and pure ZnO films, respectively.

The mobility increase also is associated to grain boundary scattering. With an increase in substrate temperature, the grain size increases causing a decrease in grain boundary potential and hence an increase in mobility. The increase in grain boundary potential is also responsible for an increase in carrier concentration with substrate temperature[7].

There are assumed to be a number of methods in charge of determining the conductivity of the thin films. It can be observed from Figure 4.1 that as temperature rises, the grain size increases resulting in a decrease in grain boundary scattering and hence resistivity falls. It can be observed that resistivity decreases as temperature is risen from 150 °C to 300 °C, hence assumed theory holds true. However, it rises at 450°C to $36.05 \times 10^{-4} \Omega\text{cm}$. The same trend has been reported by Kim *et al.* [58] for indium doped tin oxides.

Consequently temperature must be responsible in increasing resistivity. From a work reported by Matsubara *et al.* [62], more oxygen was incorporated into AZO (Al-doped ZnO) films as temperature rose, increasing resistivity by filling oxygen vacancies. An overall increase in resistivity was observed for temperatures higher than 300°C as a result of an improvement in (002) texture caused by increase in grain size outweighing the filling of oxygen vacancies. As Figure 4.2 shows, carrier concentration achieves its highest at 300 °C then falls radically above 350 °C. At temperatures in surplus of 350°C, it is also probable that, the thermal energy is adequate to permit the two additional electrons exist in the lattice around the silicon atoms to ionise one oxygen atom, and therefore reduce carrier concentration.

4.1.1.3 Optical Properties of SZO Films by Varying Substrate Temperature

Figure 4.3 and Figure 4.4 illustrate well that optical transmittance in the visible range (400–700 nm) rises slightly with increasing the substrate temperature from room temperature (RT) and reaches a maximum at 450°C, and falls subsequently as the temperature increases to 500°C, and this again is contributed to the raise in grain size of the films with rising substrate temperature.

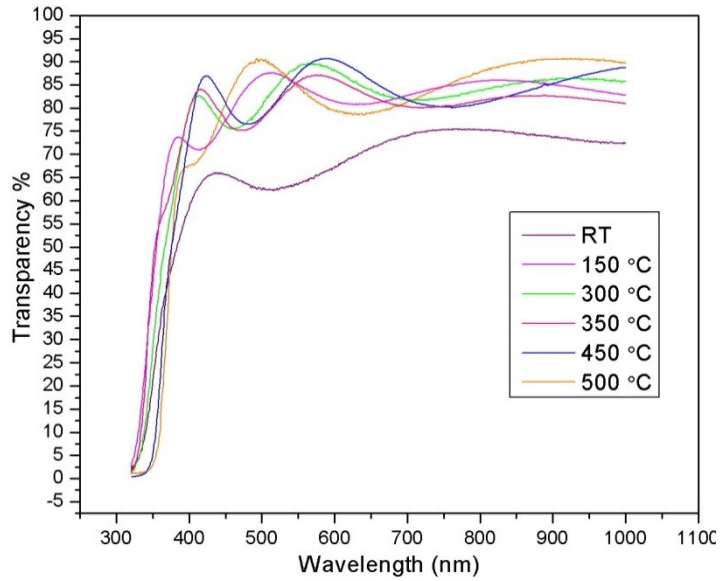


Figure 4.3 Transmittance spectra of SZO films as a function of substrate temperature. Table 4.1 shows the other used deposition parameters.

In addition, a decrease in defect concentration due to increased T_s , thus a reduction in grain boundaries, caused by rising grain size, serves to improve transmittance. Scattering photons by grain boundaries may result in a decrease in transmittance.

Deposition temperature also affects other properties of SZO films such as direct bandgap. The values of bandgap were estimated from the plots of $(\alpha h\nu)^2$ vs. $h\nu$ (photon energy) for SZO films

(Figure 4.5) vary from 3.37 to 3.61 eV. This shift of the bandgap can be explained by the Burstein-Moss model [40, 41] in which the absorption edge shift towards upper energy with a raise of carrier concentration[102].

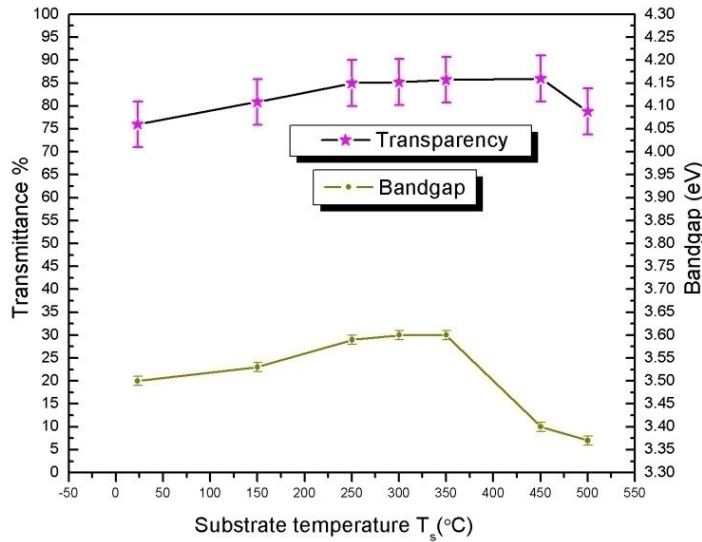


Figure 4.4 Variation of Transparency (at wavelength 635 nm) and bandgap of SZO films with substrate temperature.

It can be observed from Figure 4.6 that the bandgap varies linearly with carrier concentration, indicating that the Burstein-Moss model can explain the results on SZO films. This increase in the direct bandgap with an increase in substrate temperature up to 300 °C is due to an increase in carrier concentration, which falls subsequently as temperature increases to 500°C due to the decrease in carrier concentration. Similar results have also been reported by Caporaletti, Nisha and Kim *et al.* [102-104].

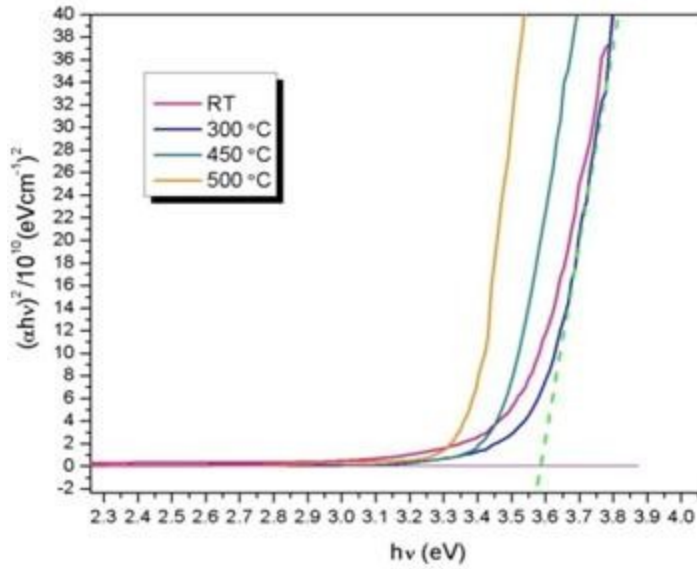


Figure 4.5 Plot of $(\alpha h\nu)^2$ vs. $h\nu$ (photon energy) for SZO films deposited by varying T_s (Method of calculating the bandgap from the transmittance for the SZO film deposited at a substrate temperature 300 °C.).

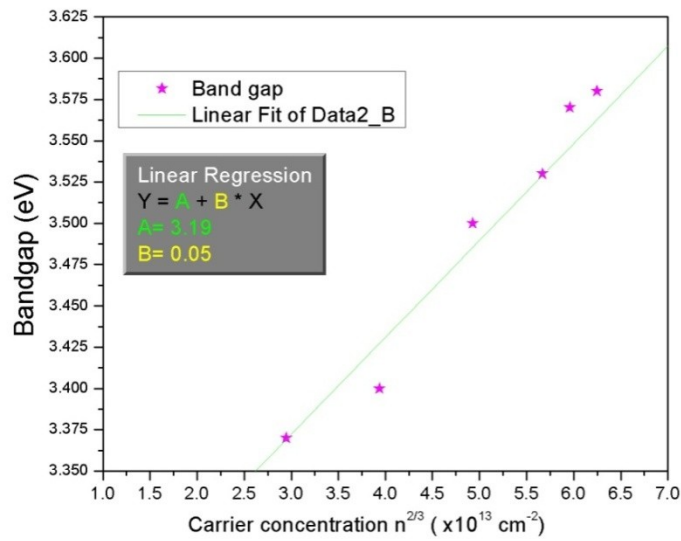


Figure 4.6 Variation of Bandgap with carrier concentration for SZO films deposited at different temperatures.

4.1.1.4 Surface Morphology of SZO Films by Varying Substrate Temperature

Figure 4.7 shows the RMS surface roughness of the films as a function of substrate temperature taken from AFM images. Figure 4.8 to 4.13 show the AFM plan view and 3D view of the films (The area from which the roughness measurements were extracted was $1 \times 1 \mu\text{m}^2$ for all substrate temperatures).

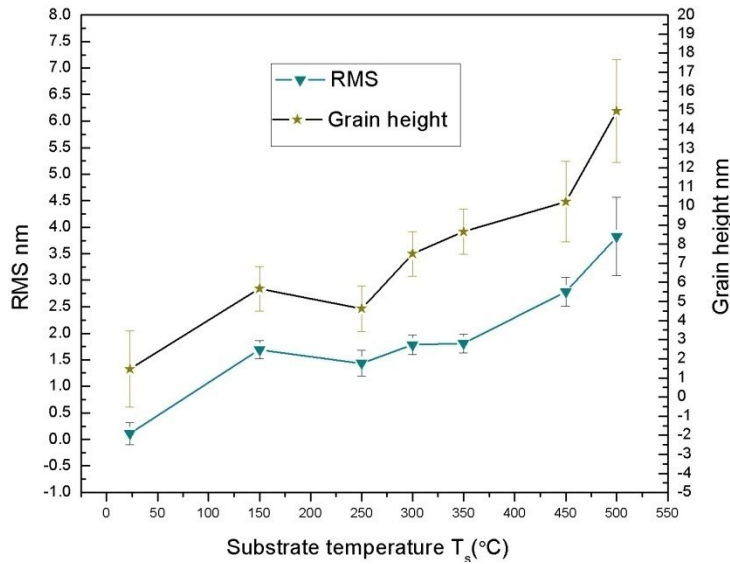


Figure 4.7 Variation of grain height and root mean square (RMS) of the Si:ZnO as a function of substrate temperature (T_s)

The roughness of SZO thin films increases as T_s increases. Figure 4.14, Figure 4.15 and Figure 4.16 are respectively the images of the surface morphology of the films deposited at 150, 300 and 450 °C using scanning electron microscopy (JEOL 7000).

With an increase in T_s from room temperature to 500°C the surface root mean square (RMS) roughness values increase from 0.11 nm to 3.82 nm. The same trend can be seen for the average grain height. At 500 °C T_s grain height reaches its maximum (14.92 nm).

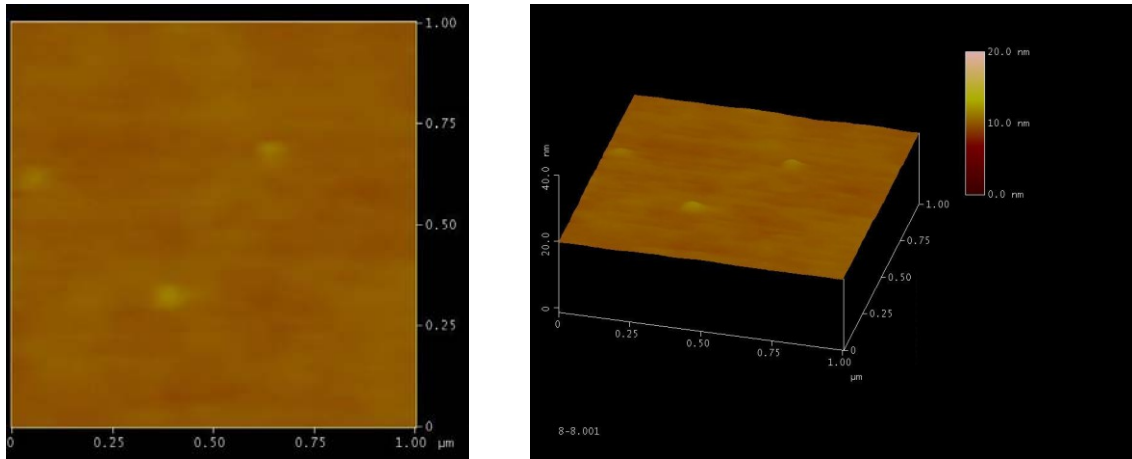


Figure 4.8 AFM (Left) Front and (right) 3D view images of the SZO films grown at room temperature.

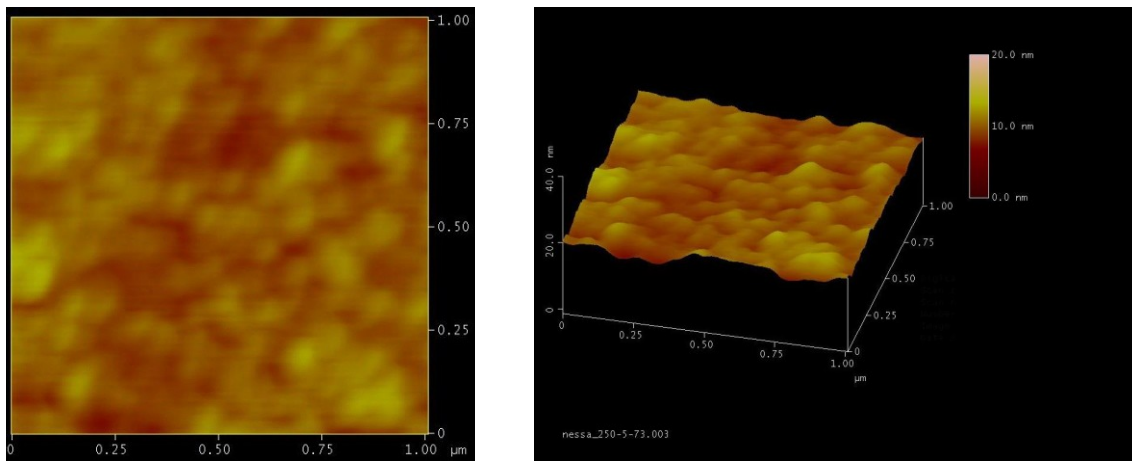


Figure 4.9 AFM (Left) Front and (right) 3D view images of the SZO films grown at 150°C.

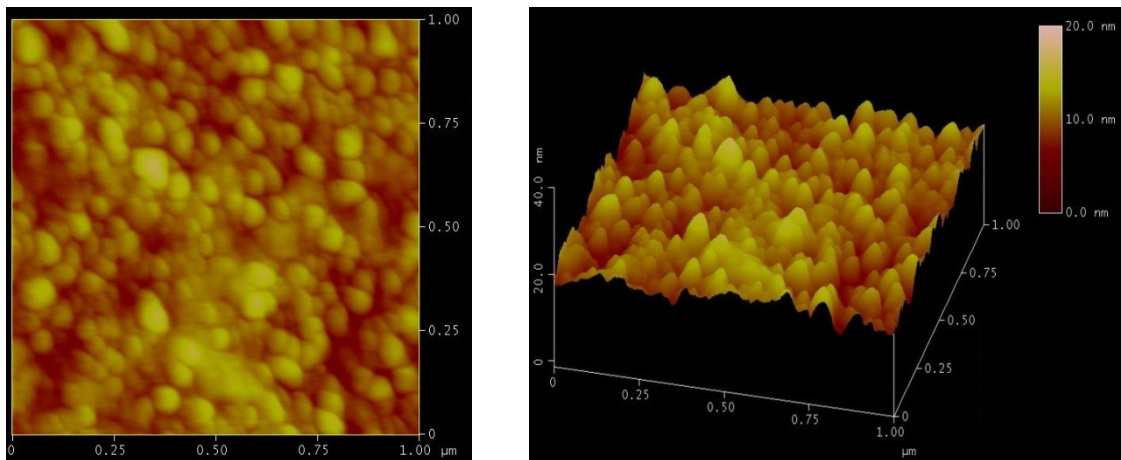


Figure 4.10 AFM (Left) Front and (right) 3D view images of the SZO films grown at 250°C.

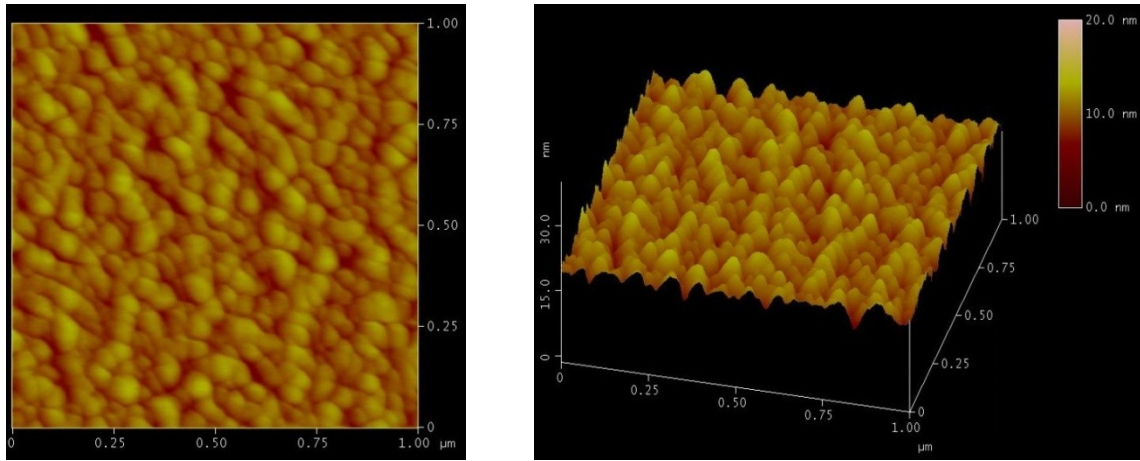


Figure 4.11 AFM (Left) Front and (right) 3D view images of the SZO films grown at 300°C.

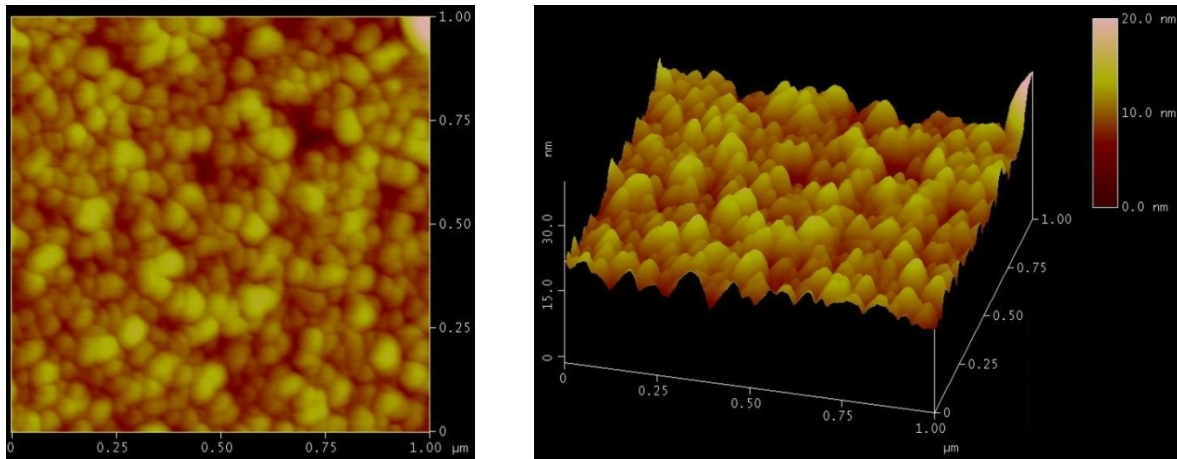


Figure 4.12 AFM (Left) Front and (right) 3D view images of the SZO films grown at 350°C.

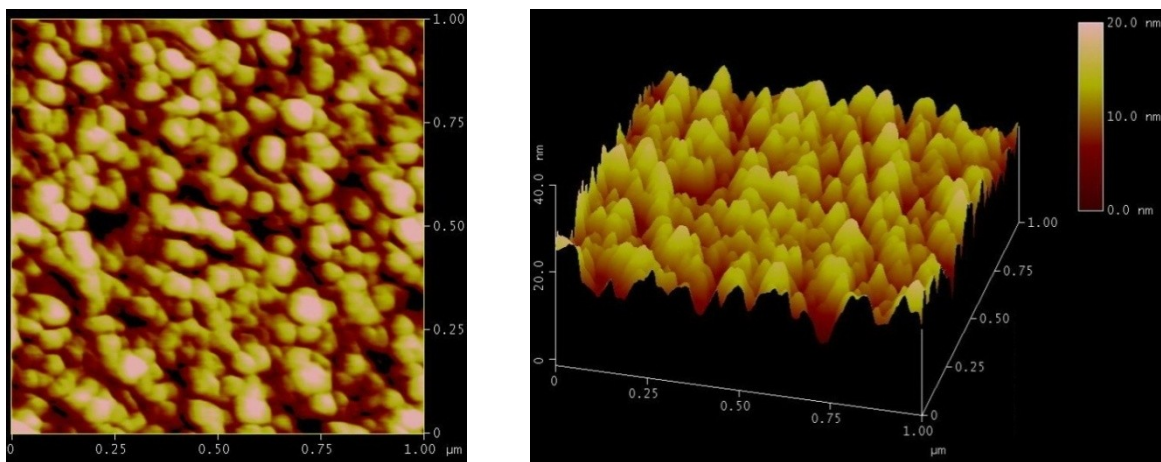


Figure 4.13 AFM (Left) Front and (right) 3D view images of the SZO films grown at 450°C.

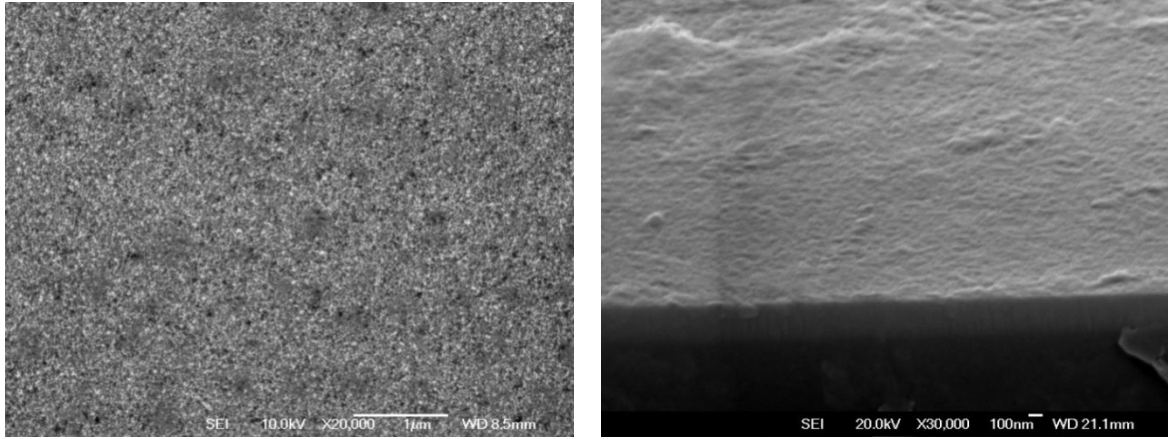


Figure 4.14 SEM image of the SZO film grown at 150 °C, (Left: front view and right: cross section). ($\times 20000$, 10 kv)

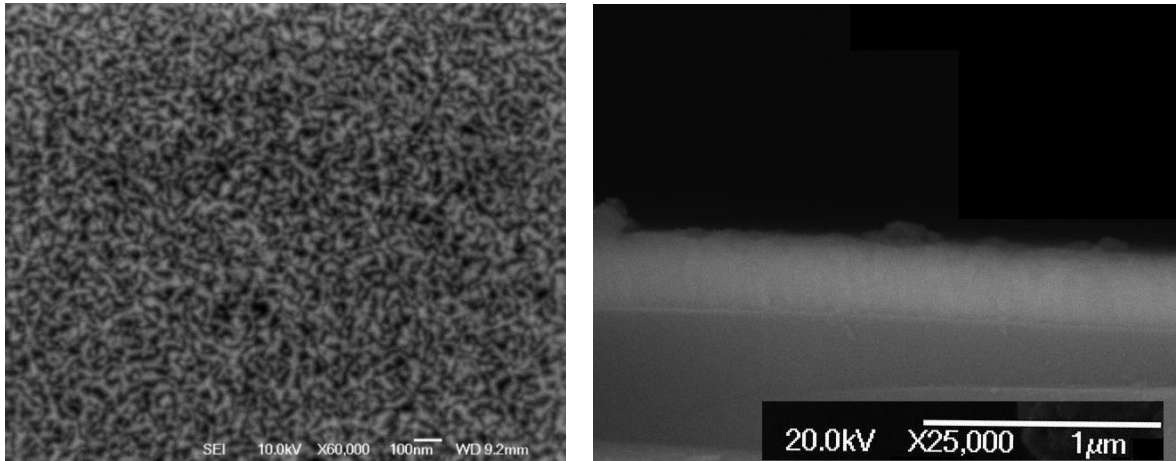


Figure 4.15 SEM image of the SZO film grown at 300 °C, (Left: front view and right: cross section) ($\times 60000$, 10 kv)

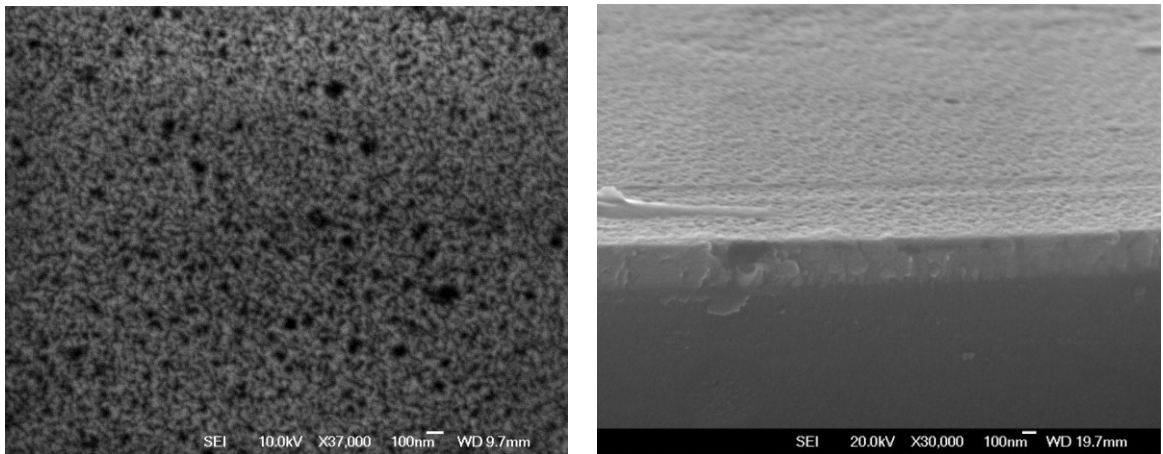
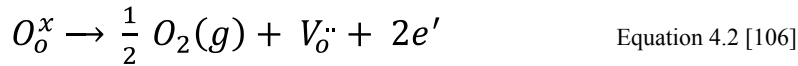


Figure 4.16 SEM image of the SZO film grown at 450 °C, (Left: front view and right: cross section) ($\times 37000$, 10 kv)

4.1.2 Influence of Oxygen Pressure on SZO films

The oxygen deposition pressure also affects the optical and electrical properties of the SZO films. The resistivity of SZO films can be minimized by increasing the free carrier concentration through doping and increasing oxygen vacancies. However, increasing the number of free carrier concentration leads to a decrease in the mobility of the films due to carrier–carrier scattering[105]. Hence, there is a trade-off between the mobility and the carrier concentration for attaining high conductivity. Each oxygen vacancy supplies two free electrons:



Oxygen vacancies rise as oxygen pressure reduces, which bring about a raise in carrier concentration and thus a drop in film resistivity. However, additional oxygen deficiency can lead to an increase in resistivity because of structural disorders.

To study the dependence of SZO films on deposition oxygen pressure by PLD, all other deposition parameters were fixed; Table 4.2 and 4.3 show the summary of SZO films by varying PO_2 (Partial oxygen pressure) respectively for target number one and four.

Table 4.2 Summary of SZO deposition results by varying oxygen pressure (Target No. 1)

Target No.1 Substrate temperature= 300 ° C D_{T-S} (Target-to-substrate distance) = 70 mm, E (incident energy) = 180 mJ, Number of pulses = 5000, 10 hz									
Oxygen pressure mTorr	Thickness nm	Resistivity ρ (×10 ⁻⁴ Ω cm)	Resistance Ω	Transparency %	002 height	FWHM	RMS nm	Grain height nm	Crystal size nm
0.01	402	9.7	5.3202	75.7	23389	0.38	1.24	4.77	22.15
2	396	7.3	4.0694	80.4	85855	0.23	1.15	2.81	35.90
5	389	6.4	3.6312	88.1	215289	0.18	0.86	2.53	46.18
6	370	8.4	4.9998	88.1	292757	0.19	1.85	6.91	43.53
8	361	7.5	4.5662	87.3	220877	0.19	2.08	11.73	44.47
11	350	18.6	11.752	80.5	48929	0.26	2.14	10.43	31.86
14	348	17	10.8038	80	26936	0.28	5.15	15.62	29.28
50	209	70.4	70	76	3805	0.35	6.20	18.00	23.80
500	175	12234	15300	73	1013.5	0.40	6.80	38.00	20.00

Table 4.3 Summary of SZO deposition results by varying oxygen pressure (Target No. 4)

Target No.4 Substrate temperature= 300 ° C D_{T-S} (Target-to-substrate distance) = 70 mm, E (incident energy) = 180 mJ, Number of pulses = 5000									
Oxygen pressure mTorr	Thickness nm	Resistivity ρ (×10 ⁻⁴ Ω cm)	Hall mobility μ (cm ² V ⁻¹ S ⁻¹)	Carrier concentration n (cm ⁻³)	Transparency %	002 height	FWHM	RMS (nm)	Crystal size nm
0.5	290	6.1	25.17	2.14E+20	73.7	23389	0.38	1.90	22.15
2	289	4.44	26.29	6.12E+20	76.4	85855.5	0.23	1.83	35.83
5	276	4.12	26.61	6.35E+20	89	86534	0.21	1.40	40.76
8	210	6.07	23.3	5.8E+20	89	109005	0.21	1.13	40.00
11	198	14	9	8.6E+19	87	49037	0.30	5.15	27.72

4.1.2.1 Structural Properties of SZO Films by Varying Oxygen Pressure

The strong diffraction peak of the (002) plane can be observed from Figure 4.17 for the SZO films grown at 5 mTorr to 8 mTorr. The crystal size of the SZO film prepared at 0.01 mTorr raises from 22.15 nm (using Scherrer's formula) to 46.18 nm for the film grown at 5 mTorr oxygen pressure and then decreases down to 20 nm as oxygen pressure reaches 50 mTorr. The same results were reported by Park *et al.* [101]. Their results also confirmed that the improved texture and larger crystal size was observed for the films grown at 5 mTorr oxygen pressure.

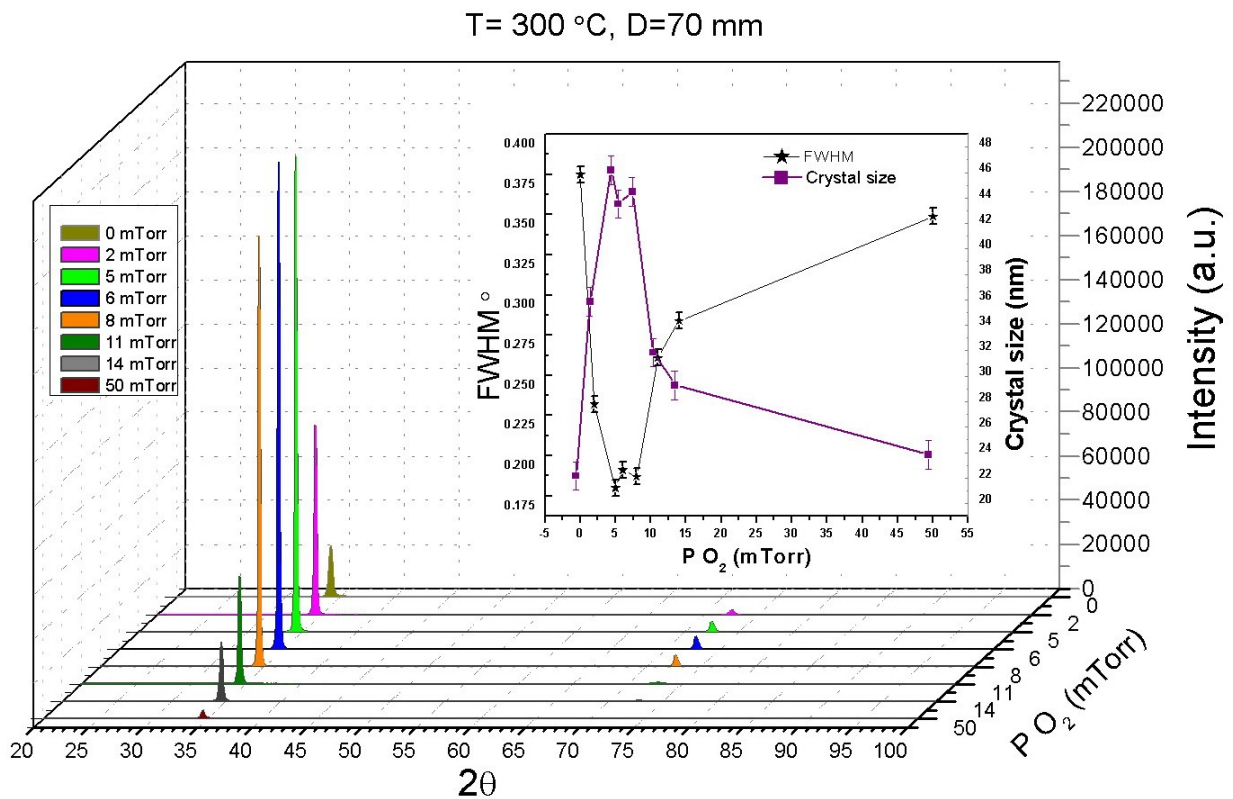


Figure 4.17 Variation of XRD pattern with oxygen deposition pressure for SZO films; The inset shows the dependance of FWHM (deg.) and crystal size (nm) on oxygen deposition pressure for SZO; films other used deposition parameters can be found in Table 4.2 The oxygen pressure varies from 0 mTorr to 50 mTorr.

It is clear from Figure 4.17 that the crystallinity of the films improves when the ambient oxygen pressure increases to 6 mTorr and then decreases for the sample prepared at 11 mTorr. It can be implied that the excess oxygen might induce defects and improve the films stoichiometry, which has a great impact on the growth and nucleation of the films, and leading to the deterioration of the crystallinity. A fall in mobility and a raise in carrier concentrations is observed for ratios O and Zn more than the optimized oxygen pressure of 5 mTorr, it can be because of the effect of excess oxygen on changes in growth mode and crystal quality [101]. The mobility of adatoms is dependent on their energy which is related to the oxygen ambient pressure. In higher oxygen pressures, the scattering of the ejected species from the target will be decreased due to decrease in their energy. At the oxygen pressure below 2 mTorr, energetic particles will bombard the growing film and may cause structure disorder ascribed to severe oxygen deficiency[107].

All the SZO films grown in the PO_2 regime of 0.01-14 mTorr are predominantly c-axis oriented in normal to the substrate direction. Though, the ZnO film grown at 0.01 mTorr is mostly randomly oriented and shows weaker ZnO peak intensity, confirming its low crystallinity.

The kinetics of atomic arrangements may also influence the film crystallinity during deposition. To achieve well textured film, there must be adequate time for deposited atoms to diffuse into the thermodynamically stable sites of the surface before deposition of next layer on top of it. There are some factors like the deposition flux energy and substrate temperature which determine the kinetics of this arrangement. The mean energy of atoms in the flux is about 10 eV, and is decreased by the ambient gas collision [43]. Therefore, the energy of the PLD plume is determined by means of the ambient gas pressure; higher pressure causes lower deposition energy [60].

4.1.2.2 Electrical Properties of SZO Films by Varying Oxygen Pressure

The resistivity of SZO films is highly sensitive to the ambient oxygen pressure. Figure 4.18 illustrates the effect of oxygen pressure on the resistivity of SZO films. The minimum resistivity observed for both targets was at a deposition pressure of 5 mTorr. It appears that at 5 mTorr sufficient oxygen vacancies exist in the film to reach the minimum resistivity of $4.12 \times 10^{-4} \Omega \text{ cm}$. At lower ambient oxygen pressure the resistivity is slightly higher than that of the sample prepared at 5 mTorr due to higher number of defects which leads to the lower mobility produced by increase in ion scattering by the defects. With increasing oxygen content of SZO films from 5 mTorr, the carrier concentration decreased and the resistivity increased. This can be explained by the fact that diffusion of the oxygen in films decreases the number of oxygen vacancies which are responsible for the generation of free electrons [63].

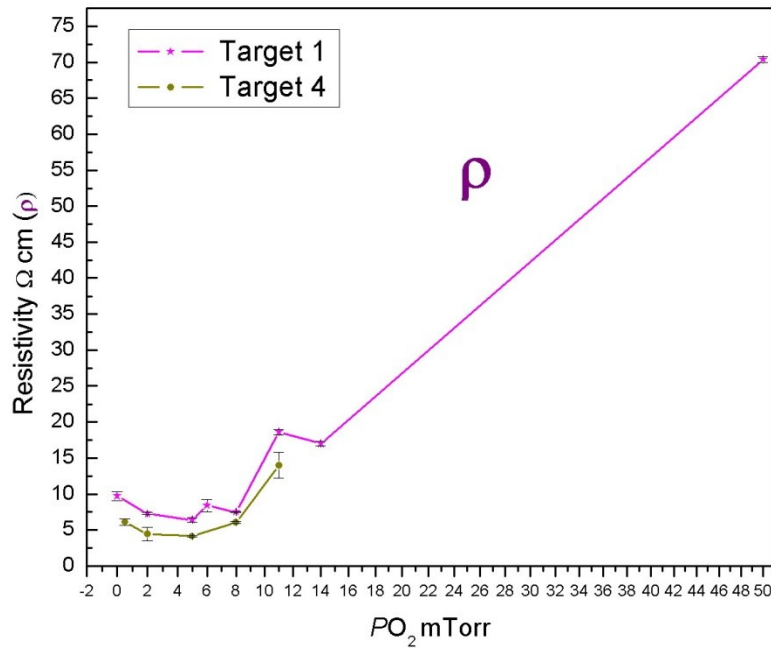


Figure 4.18 Resistivity at room temperature of SZO films grown by targets number one and four versus oxygen partial pressure during PLD film growth. The lines directly connected the measured points. The other deposition parameters can be observed in Table 4.2 and 4.3.

Park *et al.* [101] observed a gradual decrease in the carrier concentration as the PO_2 was increased. Using the Van der Pauw method, Hall measurements have been carried out at room

temperature (Figure 4.19). A maximum in the carrier concentration and carrier mobility was observed for an oxygen pressure of 5 mTorr. The carrier mobility reduces for the oxygen pressure higher than 5 mTorr. Carrier mobility and carrier concentration thus decrease with increasing oxygen pressure from 5 mTorr as the ratios of O and Zn increases resulting in crystallinity and growth mode changes by the excess oxygen. Higher mobility can be achieved due to an improved crystallinity. At fixed substrate temperature and incident laser energy, the oxygen ambient pressure is the dominant factor to control the atomic kinetic energy. Thus, at an optimised oxygen pressure, 5 mTorr, adatoms can move quickly to grow on the lowest energy sites and structure the lowest energy plane which is (002) orientation for ZnO films [14] and improve the crystallinity. When the ambient oxygen pressure surpasses 5 mTorr, the (002) shows weaker intensity and larger FWHM values, which shows degradation in crystalline quality. From one point of view, the kinetic energy of atoms in the plasma plume is reduced by collision with the ambient gas. Therefore, the possibility for formation of the lowest energy surface is decreased by the energy decrease of atoms. On the other hand, thinner films will be generated by collision between ambient gas and the atoms in the flux. So the crystallinity is degraded [60]. Therefore, there is an optimum oxygen pressure, which is 5 mTorr, in these experiments for both targets.

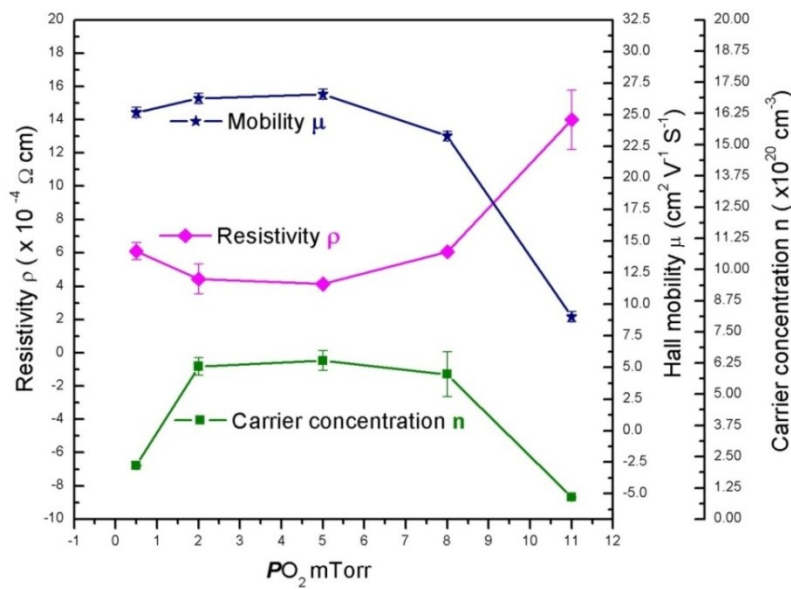


Figure 4.19 Carrier concentration, Hall mobility and resistivity of SZO films grown by target number 4 versus oxygen partial pressure during PLD film growth. Table 4.3 shows the other deposition parameters.

4.1.2.3 Optical Properties of SZO Films by Varying Oxygen Pressure

Optical transmittance is observed to improve significantly as pressure rises. This might be as a result of an enhancement in stoichiometry, owing to the filling of oxygen vacancies, which may lead to a fall in the concentration of defects and a following improvement in transparency. It also can be ascribed to an increase in the grain size of SZO films, as noticed in the XRD spectra (Figure 4.17). Figure 4.20 and Figure 4.21 illustrate well that optical transmittance in the visible range (400–700 nm) increases dramatically with increasing the oxygen partial pressure from 0.01, reaches to its maximum 88 % at 5mTorr, and stays almost constant to oxygen pressure 8 mTorr and falls subsequently as PO_2 increases to 50 mTorr, and this again is related to the change in the grain size of the films varying ambient oxygen pressure.

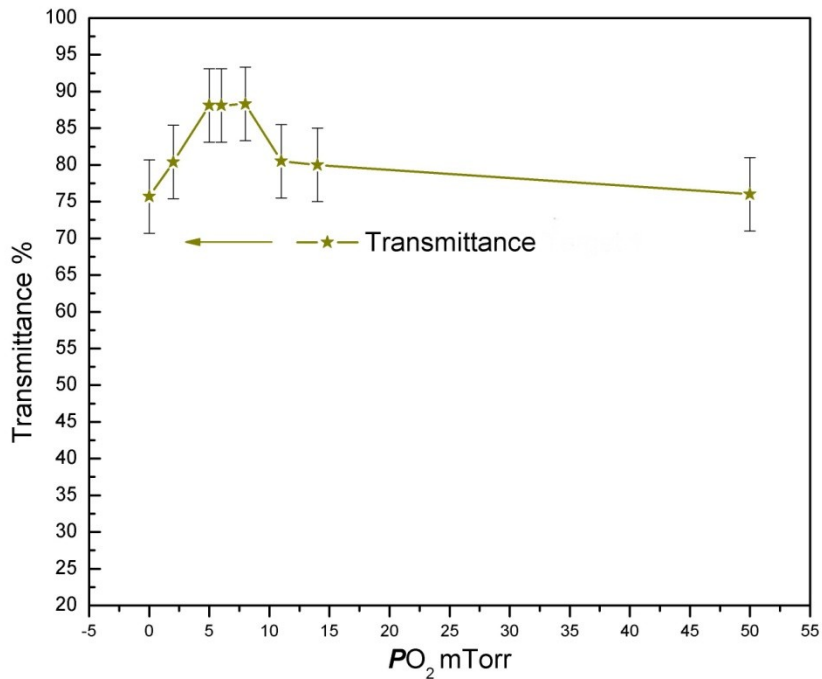


Figure 4.20 Transmittance of SZO films grown by targets number one as a function of oxygen partial pressure (at wavelength 635 nm). The other deposition parameters are available in Table 4.2 and 4.3.

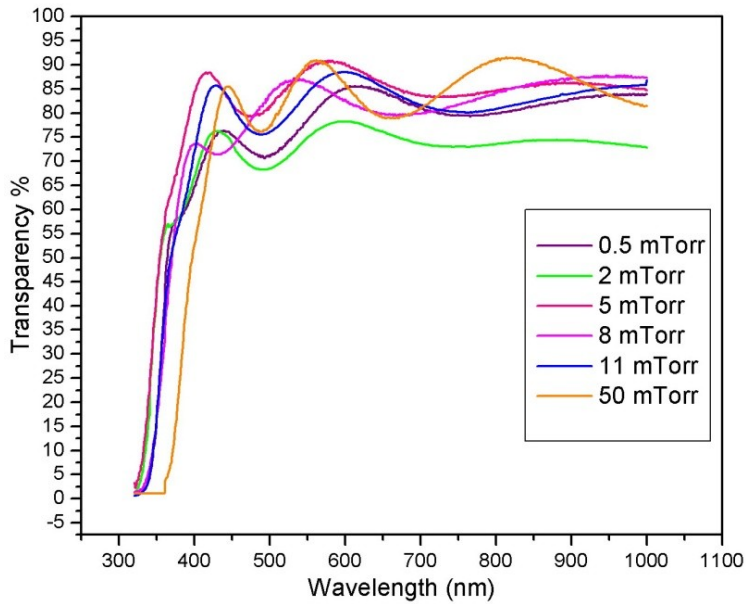


Figure 4.21 Transmittance spectra of SZO films as a function of ambient oxygen pressure.

The optical band gap of the films was measured from the plot of $(\alpha h\nu)^2$ vs. $h\nu$ (photon energy) as presented in Figure 4.22. The optical band gap of the films varied gradually from 3.65 to 3.15 eV by increasing PO_2 from 5 to 50 mTorr (Figure 4.22) by the relaxation of built-in strain [101].

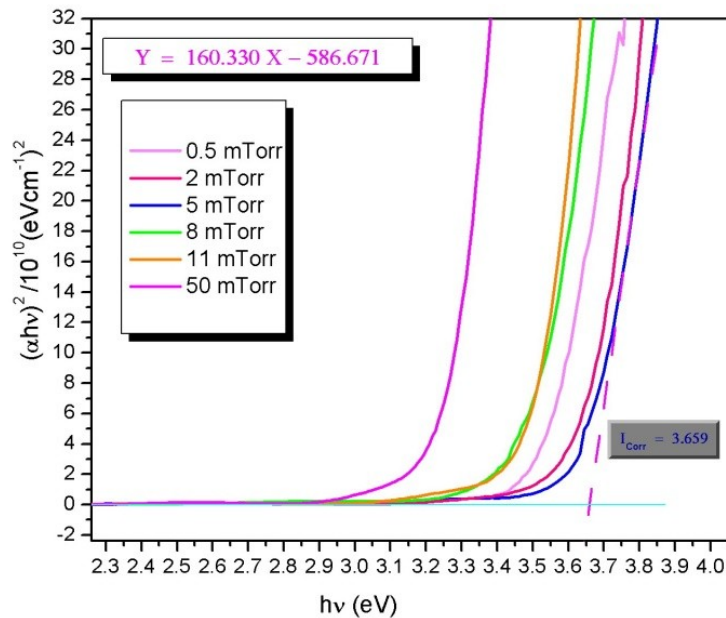


Figure 4.22 Plot of $(\alpha h\nu)^2$ vs. $h\nu$ (photon energy) for SZO films deposited by varying PO_2 (Method of calculating the bandgap from the transmittance for the SZO film deposited at oxygen pressure of 5 mTorr)

This shift of the optical band gap of SZO films by varying oxygen partial pressure can be explained by the Burstein-Moss model [40, 41] due to the filling of conduction band electronic states resulting in higher carrier concentration of these films.

Figure 4.23 shows that, band gap increases with increasing carrier concentration. Carrier concentration decreases gradually from 6.35×10^{20} to $8.6 \times 10^{19} \text{ cm}^{-3}$ when oxygen partial pressure increases from 5 to 11 mTorr (Table 4.3). Park *et al.* [101] observed the same results for Al doped ZnO films.

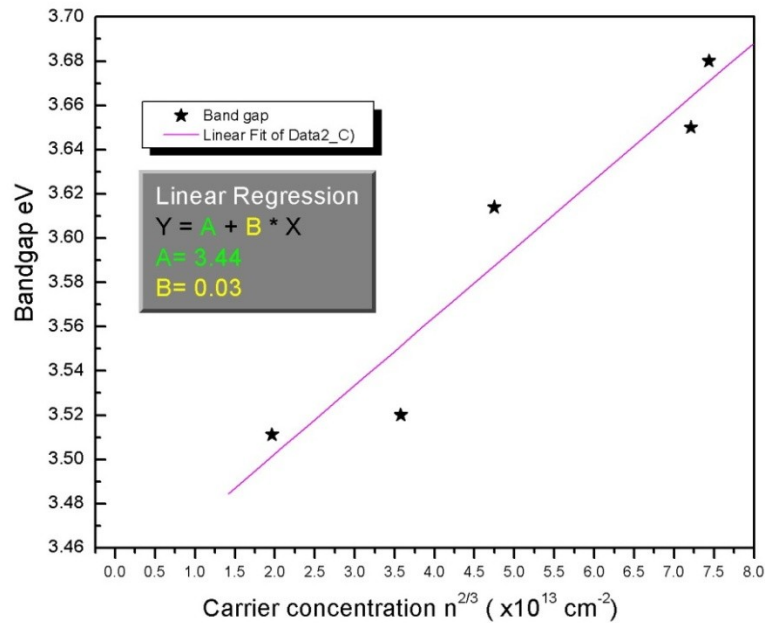


Figure 4.23 Band gap dependence of carrier concentration for the SZO films growing at different oxygen pressure.

4.1.2.4 Surface Morphology of SZO Films by Varying Oxygen Pressure

The surface morphology of the SZO films grown at various oxygen pressures was investigated using AFM and SEM. The surface morphology of SZO films is dramatically dependent on the oxygen pressure when the other deposition parameters are fixed. The root mean square (RMS) roughness values of the films, measured by AFM (area of $1 \times 1 \mu\text{m}^2$), versus oxygen partial pressure (0.01 to 50 mTorr) for SZO films can be observed in Figure 4.24. This tendency is similar to Kim *et al.*[60] and Kumar *et al.*[27].

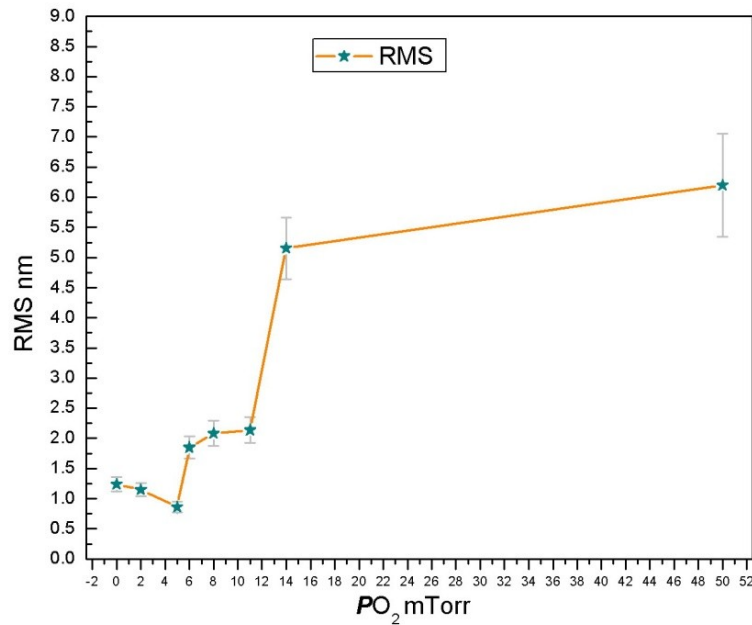


Figure 4.24 Variation in the RMS roughness of the SZO films as a function of ambient oxygen pressure. Other parameters kept constant during deposition (Table 4.2).

The RMS roughness of the film grown at $PO_2 = 5$ mTorr is as low as 0.86 nm. However, the RMS roughness increases up to 6.8 nm for the film grown at 50 mTorr. This increase in surface roughness with increasing oxygen pressure may be attributed to an improved particulate

construction in the laser induced flux, which is a usual characteristic of high-pressure laser deposition [60]. The crystallinity and alignment of the SZO films are dependent on the oxygen pressures used during film growth.

Typical AFM images of the SZO films are displayed in Figure 4.25 to Figure 4.31. It is obvious that relatively different surface morphologies are developed depending on O₂ pressure during film growth. As shown in the Figure 4.31, the film grown at the high O₂ pressure of 50 mTorr consists of much larger grain height and shows a rougher surface than the film grown at the low O₂ pressure 5 mTorr.

The effect of ambient oxygen pressure on the crystal structure of SZO films has been discussed before. Figure 4.17 shows that the crystallinity of the films improved when the ambient oxygen pressure increased to 5 mTorr and then decreased for further increase in oxygen partial pressure. The AFM images are consistent with the XRD patterns of SZO films. Figure 4.25 shows the less oriented film grown at 0.01 mTorr oxygen pressure. Smoother surface with higher crystallinity was produced at 5 mTorr ambient oxygen pressure.

SEM images of SZO films (Figure 4.32 to Figure 4.35) grown at different oxygen pressure, are correspondent to the AFM results and XRD patterns. The SZO films with smaller crystal size deposited at 0.01 and 2 mTorr oxygen ambient are more voided, less dense and non-stoichiometric compared to 5 mTorr deposited SZO films. The initial increase in crystal size with increasing oxygen pressure from 0.01 to 5 mTorr might be because of the variation in kinetic energy of the adatoms which leads to increase in the diffusion of growth species on the film surface. With further increase in oxygen pressure from 5 to 50 mTorr, the kinetic energy of the reactive particles in the flux decreases which limits surface diffusion of the deposited atoms leading to reduction in the crystal size and degradation in the film quality [27].

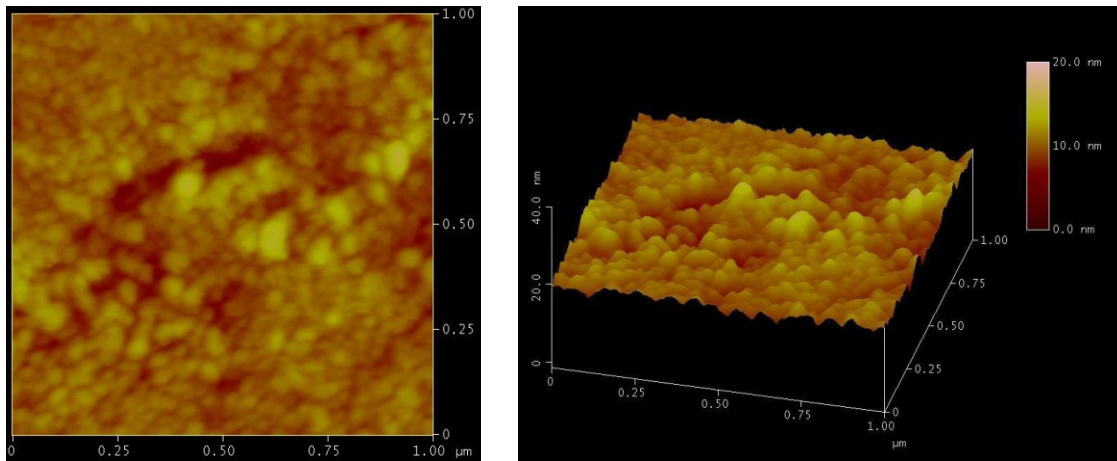


Figure 4.25 (Left) Front and (right) 3D view AFM images of the SZO film grown at 0.01 mTorr oxygen partial pressure.

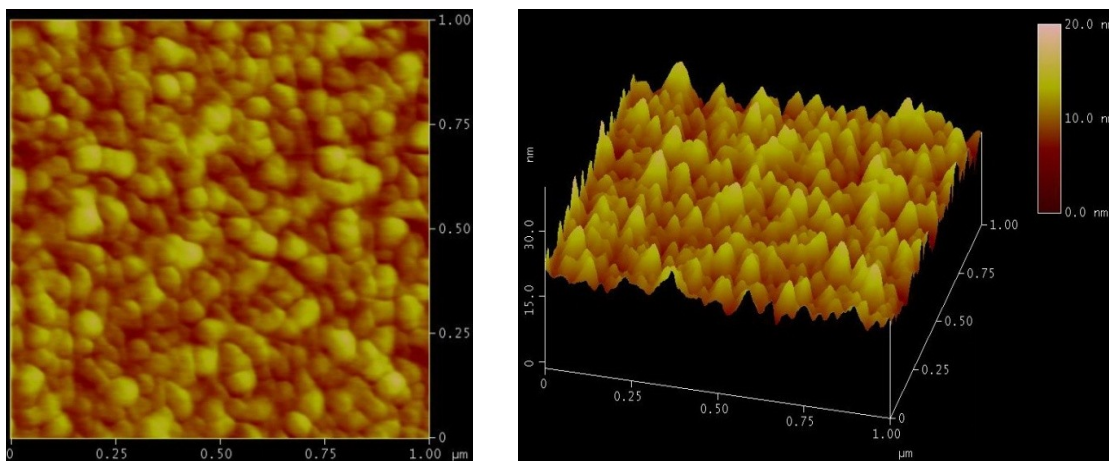


Figure 4.26 (Left) Front and (right) 3D view AFM images of the SZO film grown at 2 mTorr oxygen partial pressure

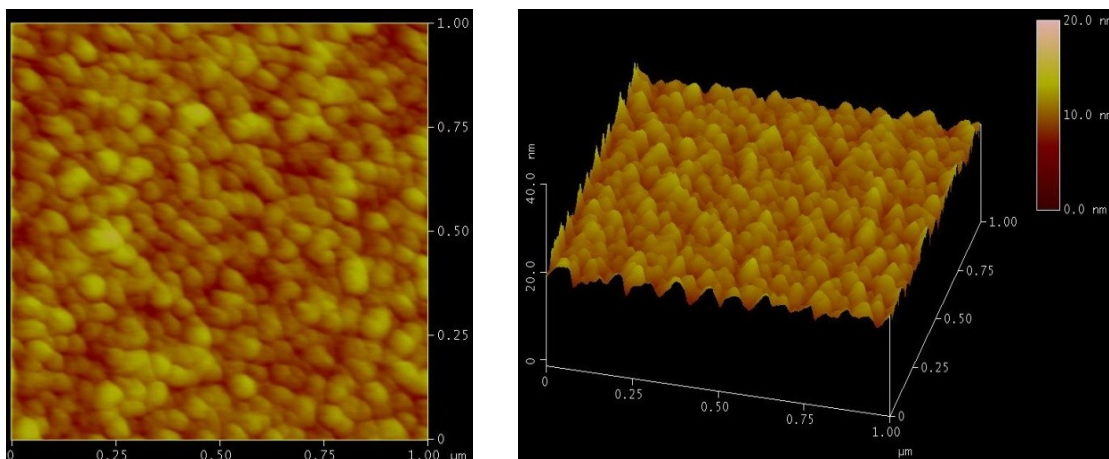


Figure 4.27 (Left) Front and (right) 3D view AFM images of the SZO film grown at 5 mTorr oxygen partial pressure

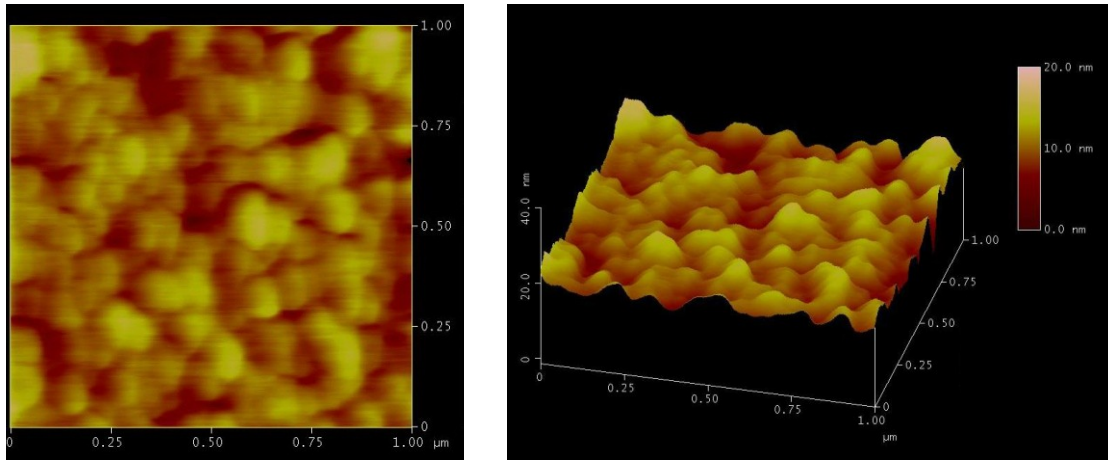


Figure 4.28(Left) Front and (right) 3D view AFM images of the SZO film grown at 8 mTorr oxygen partial pressure

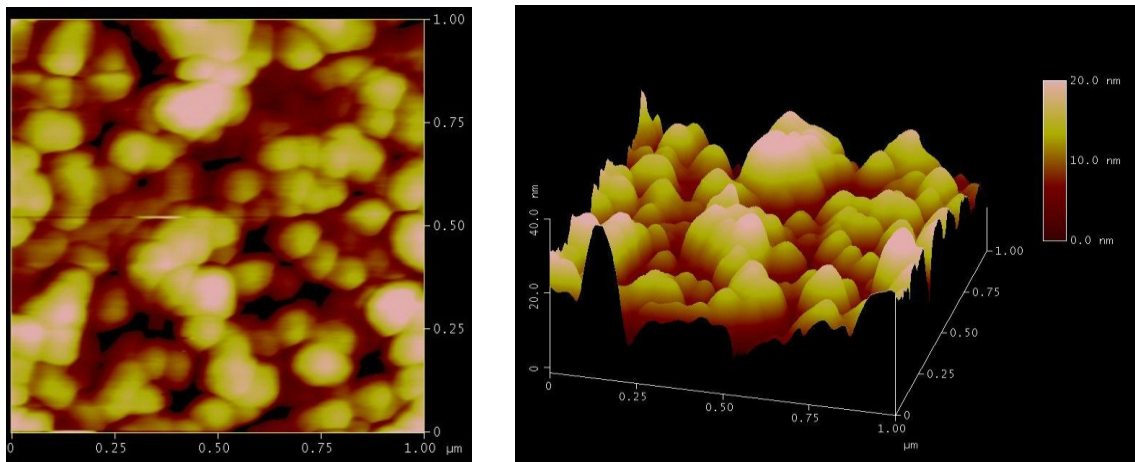


Figure 4.29 (Left) Front and (right) 3D view AFM images of the SZO film grown at 11 mTorr oxygen partial pressure

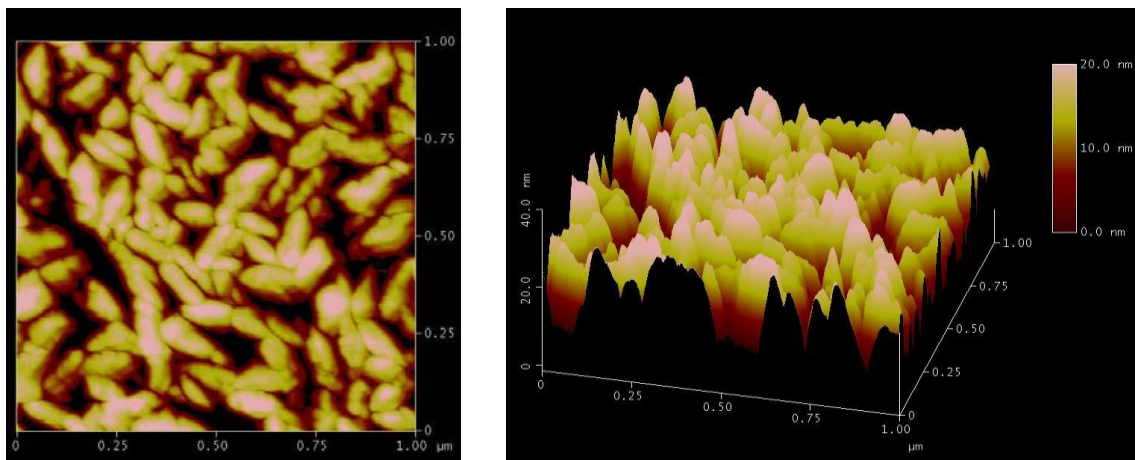


Figure 4.30(Left) Front and (right) 3D view AFM images of the SZO film grown at 50 mTorr oxygen partial pressure

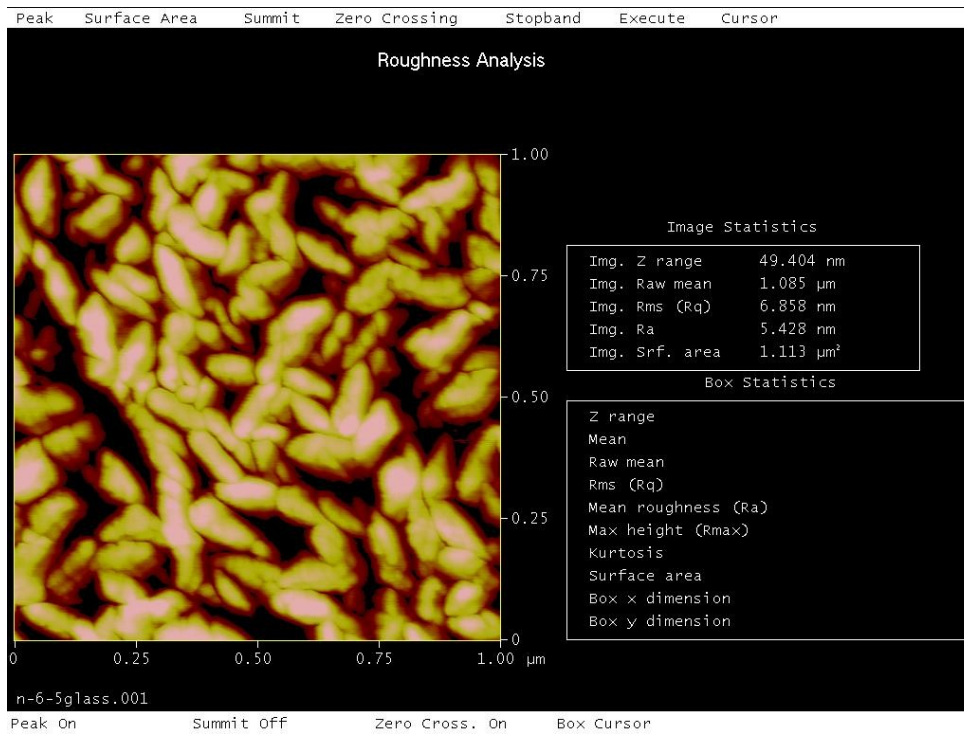


Figure 4.31 AFM roughness analysis of SZO film grown at 50 mTorr oxygen pressure.

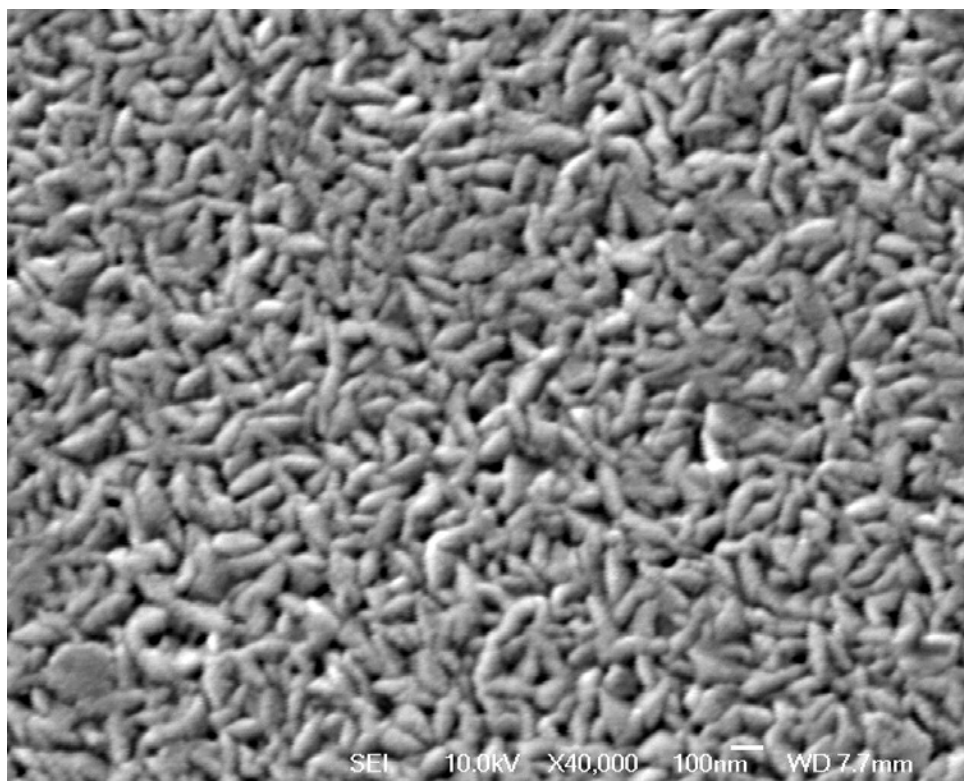


Figure 4.32 SEM image of the SZO film grown at 50 mTorr oxygen partial pressure at high magnification ($\times 40000$)

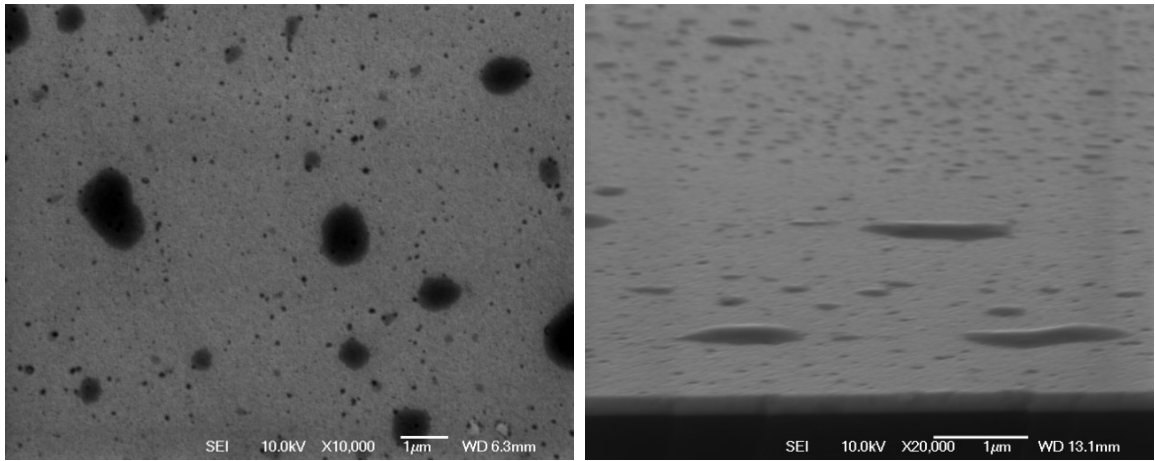


Figure 4.33 SEM (Left) Front and (right) cross section view images of the SZO film grown at 0.01 mTorr oxygen partial pressure

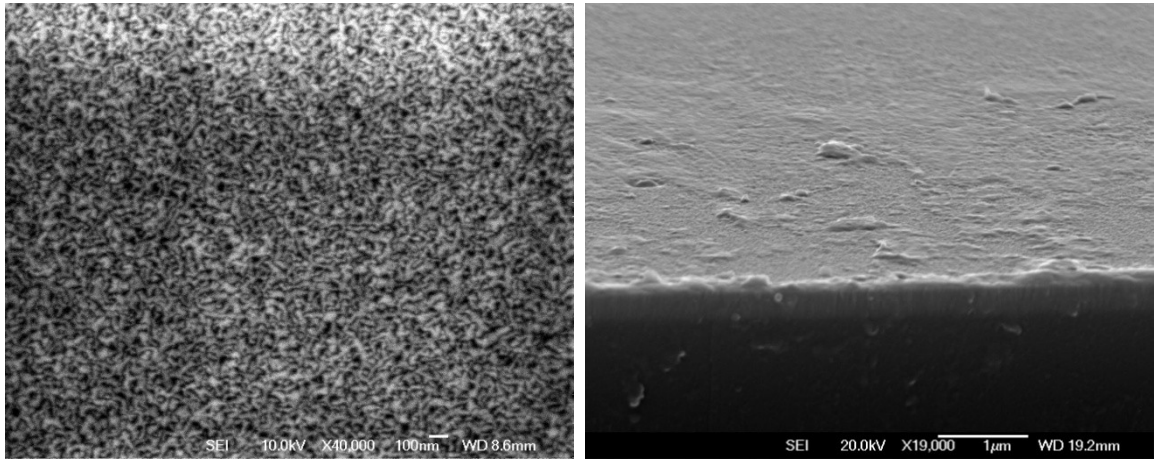


Figure 4.34 SEM (Left) Front and (right) cross section view images of the SZO film grown at 2 mTorr oxygen partial pressure

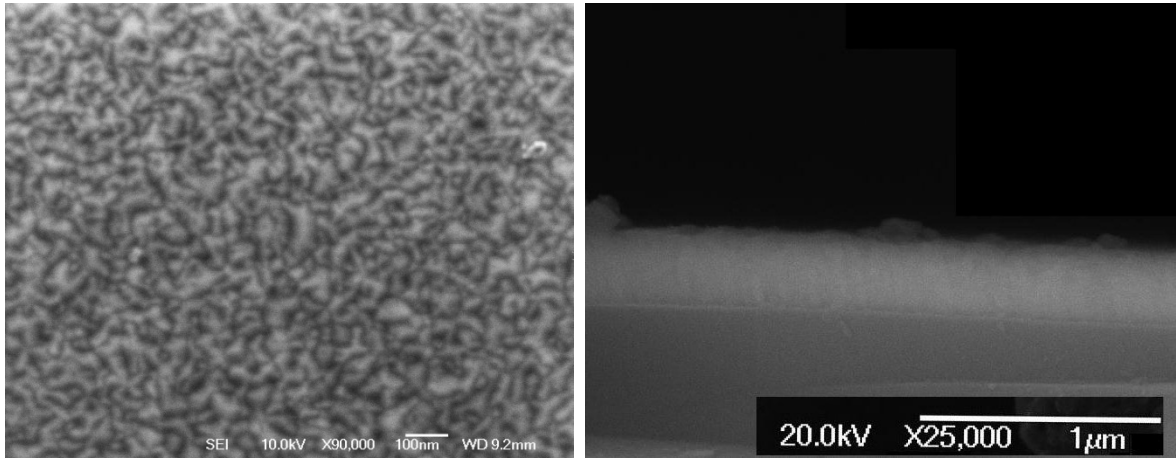


Figure 4.35 SEM (Left) Front and (right) cross section view images of the SZO film grown at 5 mTorr oxygen partial pressure

4.1.3 Influence of Target-to-substrate Distance on SZO Films

Deposition rate can be controlled by different parameters like laser fluence, oxygen partial pressure, and target-to-substrate distance D_{T-S} . The deposition rate increases with increasing fluence, decreasing the target-to-substrate distance, and decreasing oxygen partial pressure, and is linearly proportional to the laser fluence. It is well known that the laser pulse produces a plasma flux, and this flux is a crucial parameter for film growth. At a particular target-to-substrate distance, the flux loses its unidirectional velocity, scatters and thermalizes [108]. To produce high quality films, D_{T-S} should be optimized. As Castro *et al.* indicated [109], the velocity of the various species in the laser plume is higher ($>10^6$ cm/s) near the target, and reduces speed as a function of D_{T-S} (Target-to-substrate distance) due to collisions with O_2 . These energetic atoms and ions cause structural damage and stress in the film if the target is too close to the substrate. Conversely, if the target-substrate distance is too long, the deposition rate will not be quick enough resulting in poor crystallinity. At the optimal distance, a decent flux of moderately energetic atoms and ions can produce high-quality films due to the uniform velocity distribution on the substrate of the different species ejected from the target [110].

In practice, films with uniform thickness can be obtained by increasing the target-to-substrate distance to achieve optimal D_{T-S} which actually corresponds to a uniform velocity distribution of the different species ejected from the target on the substrate. As a result, the density of each species on the growing films will be equal. They can be incorporated and combine in the crystal structure resulting to form chemically homogenous thin films. In this section D_{T-S} is increased from 50 to 70 mm by 5 mm intervals and all the rest of the deposition parameters are fixed.

Table 4.4 Summary of SZO deposition results by varying target-to-substrate distance (Target No. 7)

Target No. 7 Substrate temperature= 300 ° C, Oxygen pressure = 5 mTorr, E (incident energy) = 170 mJ, Number of pulses = 5000, 10 hz									
Target-to-substrate distance	Thickness nm	Resistivity ρ ($\times 10^{-4} \Omega \text{ cm}$)	Hall mobility μ ($\text{cm}^2 \text{V}^{-1} \text{S}^{-1}$)	Carrier concentration n (cm^{-3})	Transparency %	002 height	FWHM	RMS (nm)	Grain size nm
50	442	4.29	21	5.16E+20	80.4	136148	0.31	3.57	26
55	367	4.99	23	4.46E+20	84	161846	0.24	2.75	35
60	303	5.75	27	4.03E+20	86	260323	0.22	1.09	38.3
65	272	6.5	22	3.86E+20	87	75950	0.23	0.85	36
70	235	7.03	21.9	3.14E+20	90.2	63987	0.26	0.83	31

4.1.3.1 Structural Properties of SZO Films by Varying Target-to-substrate Distance

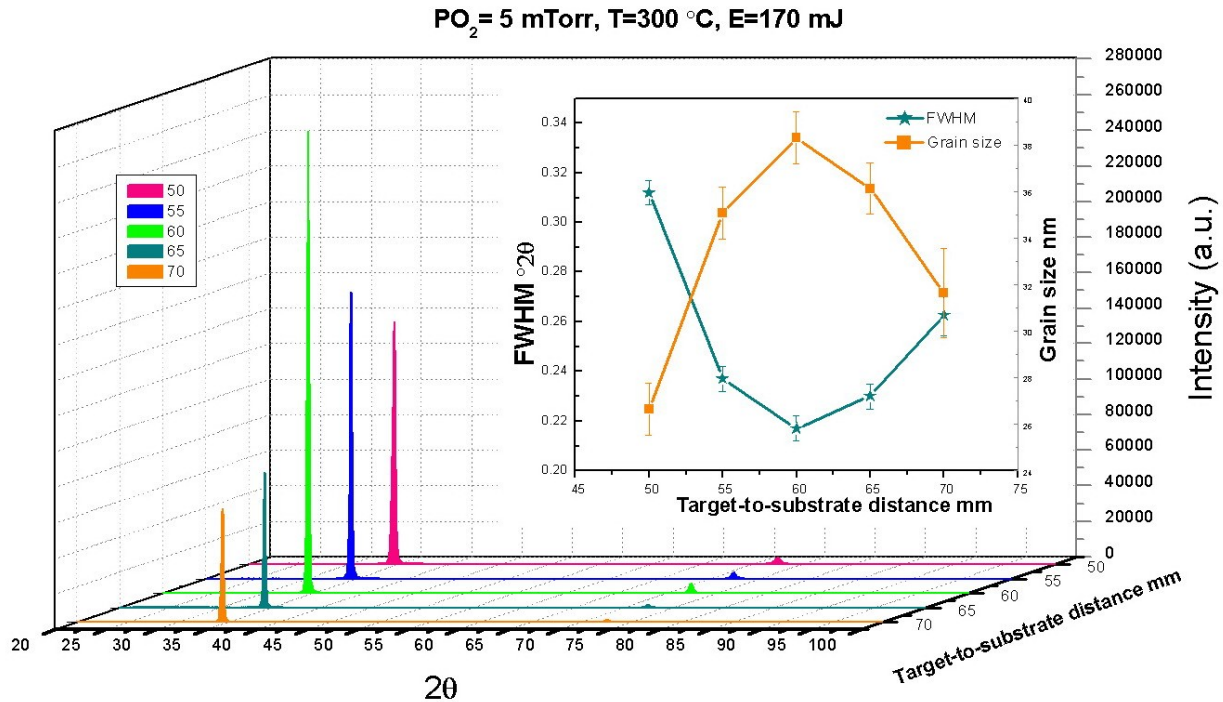


Figure 4.36 Variation of XRD patterns with target-to-substrate distance for SZO films; the inset shows the dependence of FWHM (deg.) and crystal size (nm) of SZO films on target-to-substrate distance; other used deposition parameters can be found in Table 4.4. The target-to-substrate distance varies from 50 mm to 70 mm .

Figure 4.36 shows the dependence of the structural properties on target-to-substrate distance for SZO films at a glass substrate temperature of 300 °C. All the films show a crystalline structure with a (002) preferred orientation. As the D_{T-S} increases the (002) peak shows an initial increase in intensity as well as (004) peak which is not as strong as (002) preferred orientation. The (002) peak continues to increase in intensity up to a D_{T-S} of 60 mm and falls sharply at 65 mm. From the figures obtained, it is clear that the optimum conditions for growth of a high quality film is at a D_{T-S} of 60 mm. Figure 4.36 also shows changes of FWHM from the (002) peak and the crystal size measured by the well known formula of Scherrer. The FWHM is decreased with the reduction of D_{T-S} up to 60 mm, indicating an improvement in the crystallinity of SZO films.

As shown in Figure 4.36 the crystal size the SZO films increases from 26 to 38.3 nm by increasing the target-to-substrate distance from 50 to 60 mm. However the crystal size decreases by further increase in the target-to-substrate distance up to 70 mm.

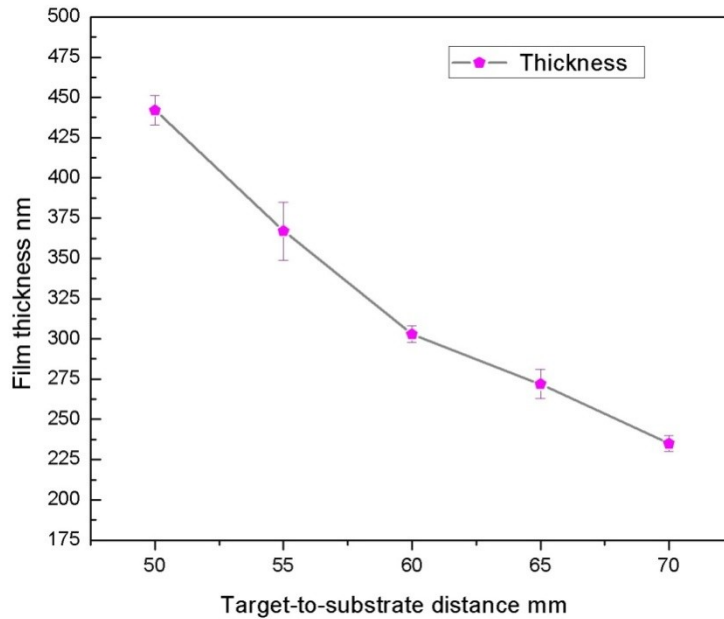


Figure 4.37 Effect of the target-to-substrate distance on the thickness for the SZO films. Other deposition parameters were kept fixed during the growth (Table 4.4) .

As can be seen from Figure 4.37, D_{T-S} (Target-to-substrate distance) has a significant impact upon film thickness. A remarkable decrease in thickness can be seen as D_{T-S} increases from 50 mm to 60 mm and it continues to decrease in thickness up to a D_{T-S} of 70 mm. The explanation could be that, less material can reach the substrate by increasing D_{T-S} .

Shim *et al.* [111] investigated the effect of the variation of film thickness on the optical and structural properties of ZnO thin films grown by PLD. They reported that increasing in film thickness enhanced the crystal quality of films, indicated by the decrease of FWHM values. Smaller the FWHM value means the larger grain size, and less grain boundaries. Grain boundaries are generally the best location for defects to be accumulated.

4.1.3.2 Electrical Properties of SZO Films by Varying Target-to-substrate Distance

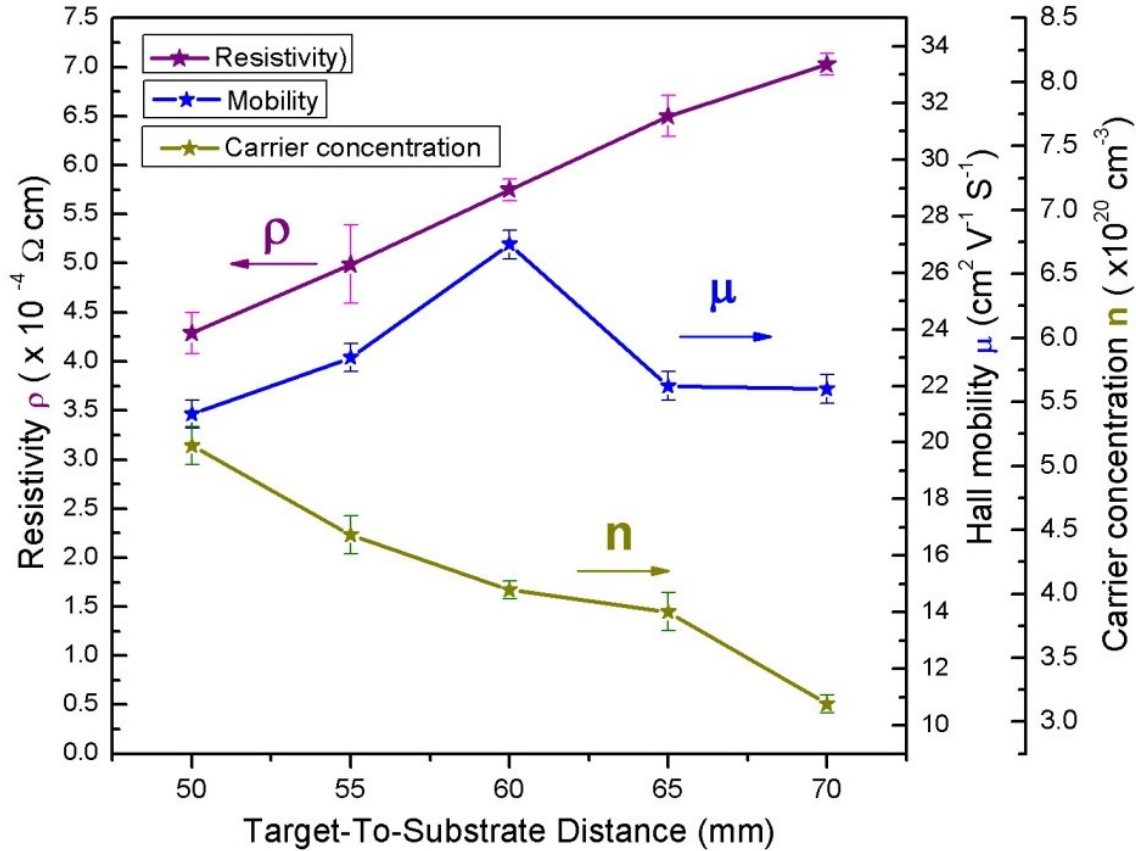


Figure 4.38 Carrier concentration, Hall mobility and resistivity of SZO films versus target-to-substrate distance during PLD film growth. Table 4.4 shows the other deposition parameters.

Figure 4.38 illustrates well that resistivity rises as D_{T-S} increases to 70 mm. However the resistivity falls with decrease in D_{T-S} , a decrease in mobility is observed for D_{T-S} from 60 to 50 mm. There is a trade-off between carrier concentration and mobility which can be explained by the XRD patterns of the deposited films. Figure 4.36 shows that, increase in D_{T-S} from 60 to 70 mm also brings about an increase in FWHM and a decrease in the grain size measured by the well known formula of Scherrer, which shows the lower crystallinity that could result in lower

mobility and consequently increase in resistivity. For the following decrease in D_{T-S} from 60 to 50 mm, however the resistivity falls and a decrease in mobility is observed. This decrease in mobility is compatible with the FWHM values of the (002) peak in SZO films. The observed decrease in resistivity and carrier concentration are consistent with the work of Shim *et al.*[111]. The bigger the grain sizes the less scattering by the grain boundaries. As discussed before the thicker the film, the better crystallinity but in the case of increasing thickness by decreasing the target-to-substrates distance, there is a threshold for the D_{T-S} , which is 60 mm for SZO film.

4.1.3.3 Optical Properties of SZO Films by Varying Target-to-substrate Distance

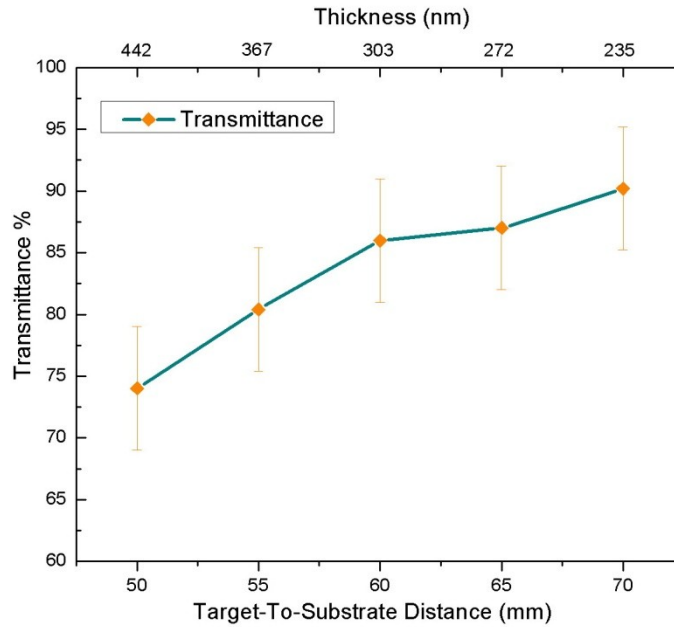


Figure 4.39 Optical transmittance measured at the wavelength 635 nm for SZO films by varying D_{T-S} and film thickness (nm). The other deposition parameters can be found in Table 4.4.

As can be observed from Figure 4.39, transparency rises with D_{T-S} . The average transparency at 50 mm is 74% increasing to 90.2 % at 70 mm. To examine the source of this low transmittance, the surface morphologies of the SZO films are investigated which will be mentioned in the next section. Based on the morphology results, the low value of transmittance in the visible range are as a result of scattering caused by the large grains on the film surface, which consecutively may have been generated by the lack of oxygen gas [112].

The transmittance of the films is decreased with increasing the film thickness due to the thickness effect.

It was mentioned before that as the D_{T-S} decreases, the resistivity continuously decreases due to an increase in carrier concentration. However the transmittance at the wavelength of 635 nm is only 74% and 80% for the SZO films obtained at the 50 and 55 mm D_{T-S} , respectively.

4.1.3.4 Surface Morphology of SZO Films by Varying Target-to-substrate distance

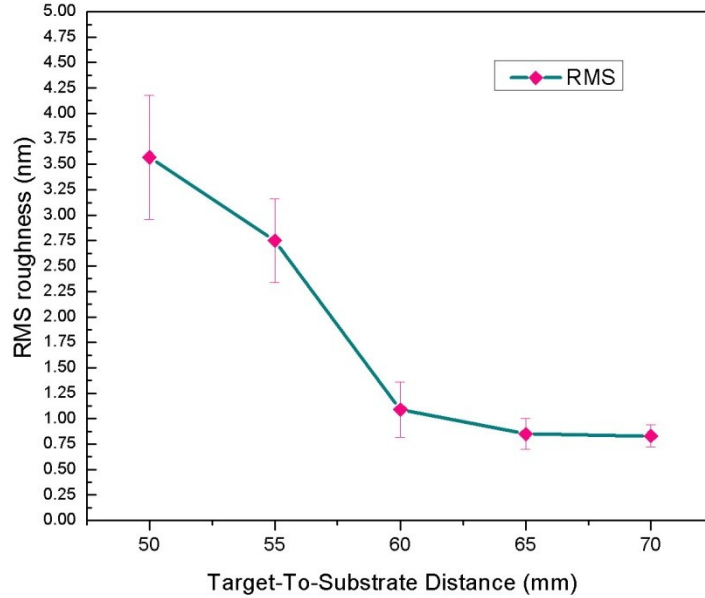


Figure 4.40 RMS surface roughness of the SZO films as a function of D_{T-S} ; D_{T-S} varies from 50 to 70 mm at 5 mm inc

Figure 4.40 illustrates well that RMS surface roughness of the films (area of $1 \times 1 \mu\text{m}^2$) falls as D_{T-S} increases. The AFM front and 3D view images of SZO films grown at various D_{T-S} are shown in Figure 4.41 to Figure 4.43. It is clear from the images that RMS roughness value and grain height of the films decrease monotonously with increase in D_{T-S} . This decrease in roughness can be attributed to fall in droplet formation on the surface as shown in the AFM 3D view images. As was discussed before, the maximum crystal size 38.3nm belongs to the film deposited at the D_{T-S} of 60 mm which decreases to 27 nm for the film deposited at 70 mm.

As could be seen from Figure 4.37, D_{T-S} has a significant impact upon film thickness. The SEM cross-section images of the SZO films grown at D_{T-S} of 50, 55, 60, and 70 mm are shown in Figure 4.44 to Figure 4.47.

Dong *et al.* [38] investigated the influence of film thickness on the roughness. The grain size was found to be continuously increased with the increase of film thickness. The increase of RMS roughness value with film thickness generally is attributed to the increase of grain size.

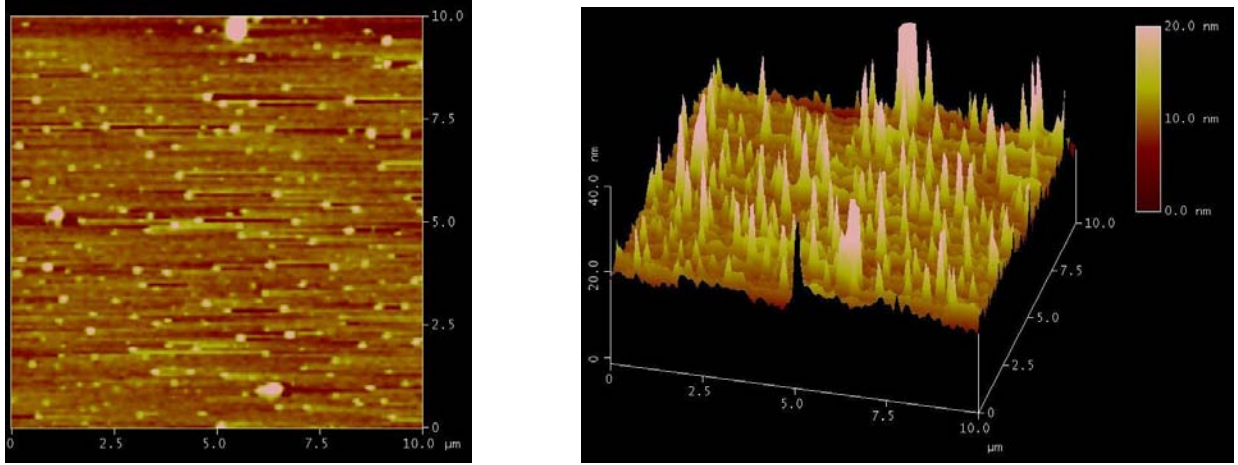


Figure 4.41 (Left) Front and (right) 3D view AFM images of the SZO film grown at D_{T-S} of 50 mm (area: $10\ \mu\text{m} \times 10\ \mu\text{m}$)

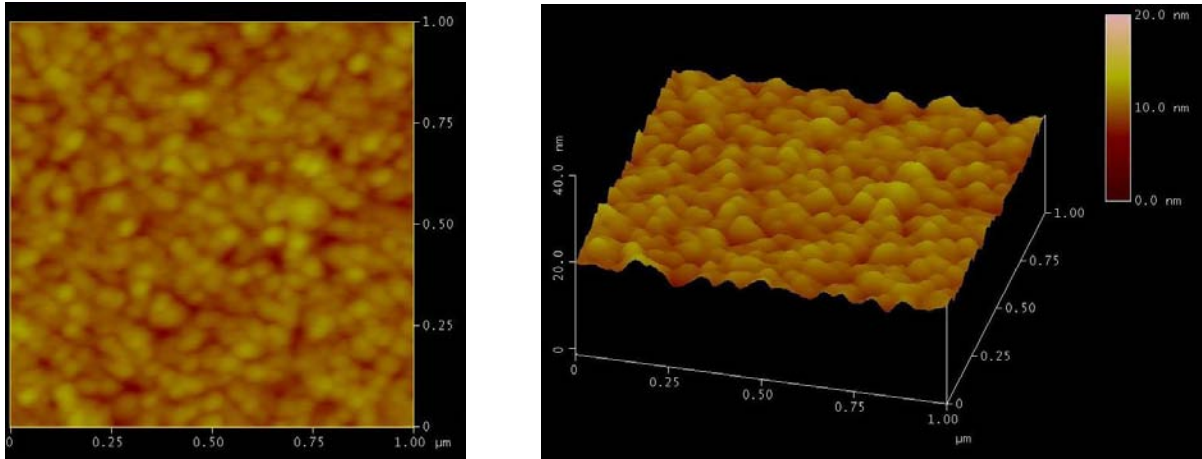


Figure 4.42 (Left) Front and (right) 3D view AFM images of the SZO film grown at D_{T-S} of 60 mm

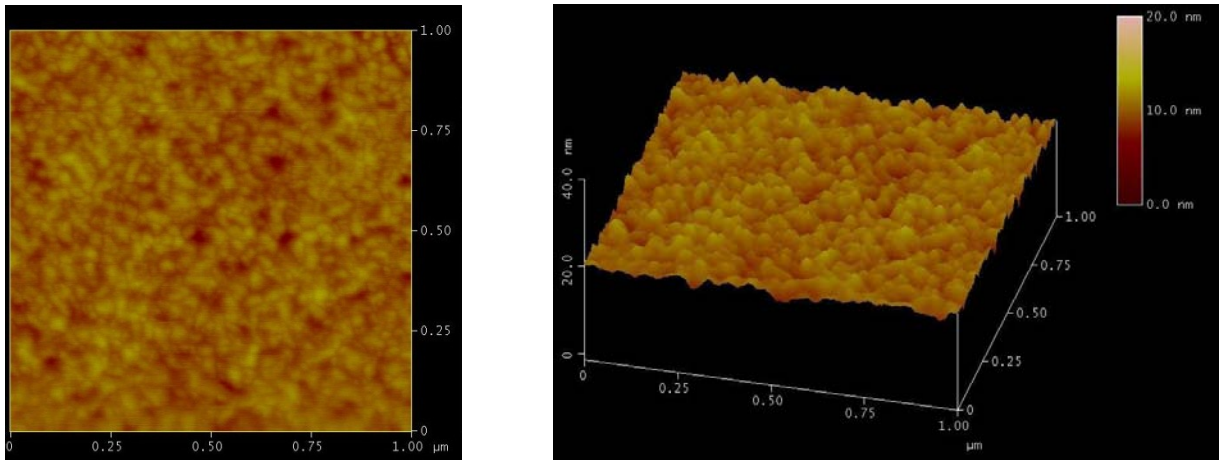


Figure 4.43 (Left) Front and (right) 3D view AFM images of the SZO film grown at D_{T-S} of 70 mm

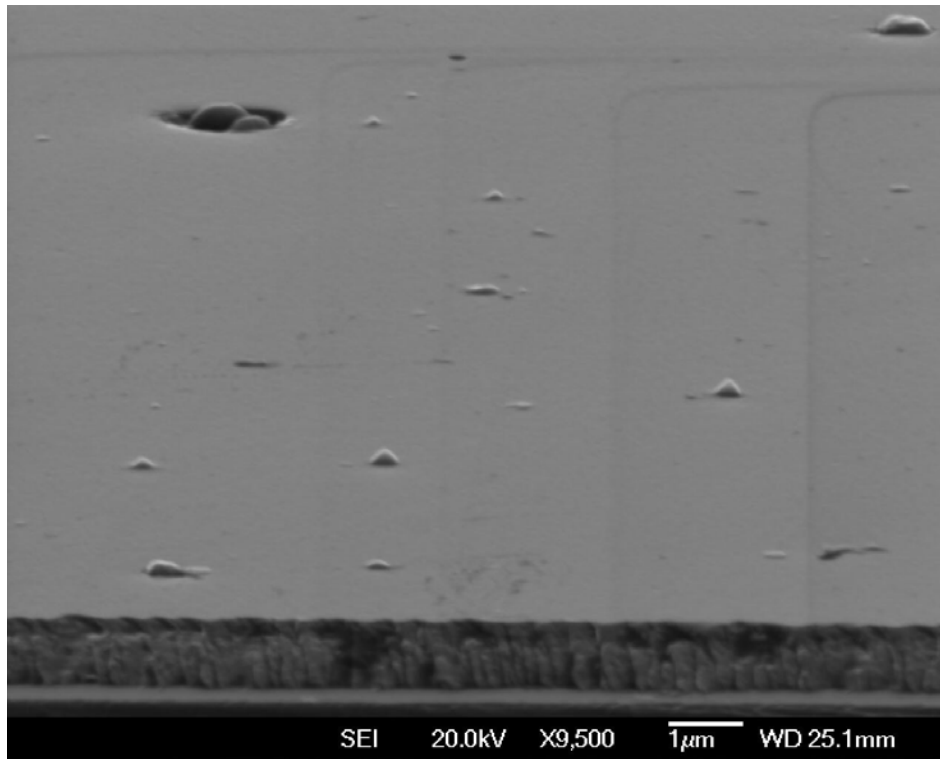


Figure 4.44 SEM cross-section image of the SZO film grown at $D_{T,S} = 50$ mm.

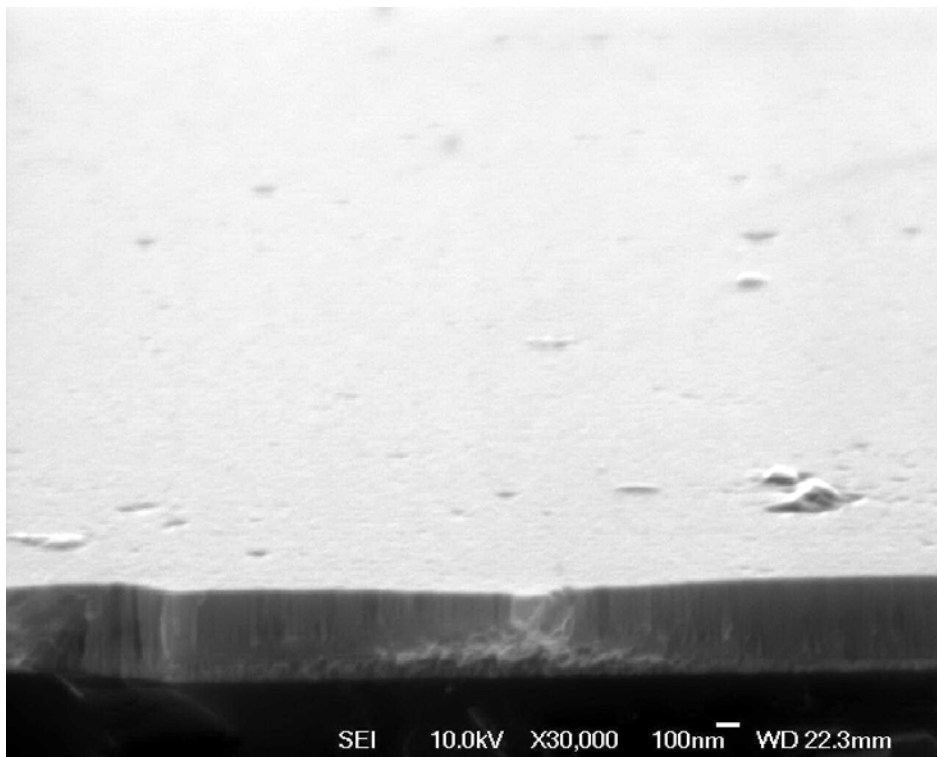


Figure 4.45 SEM cross-section image of the SZO film grown at $D_{T,S} = 55$ mm.

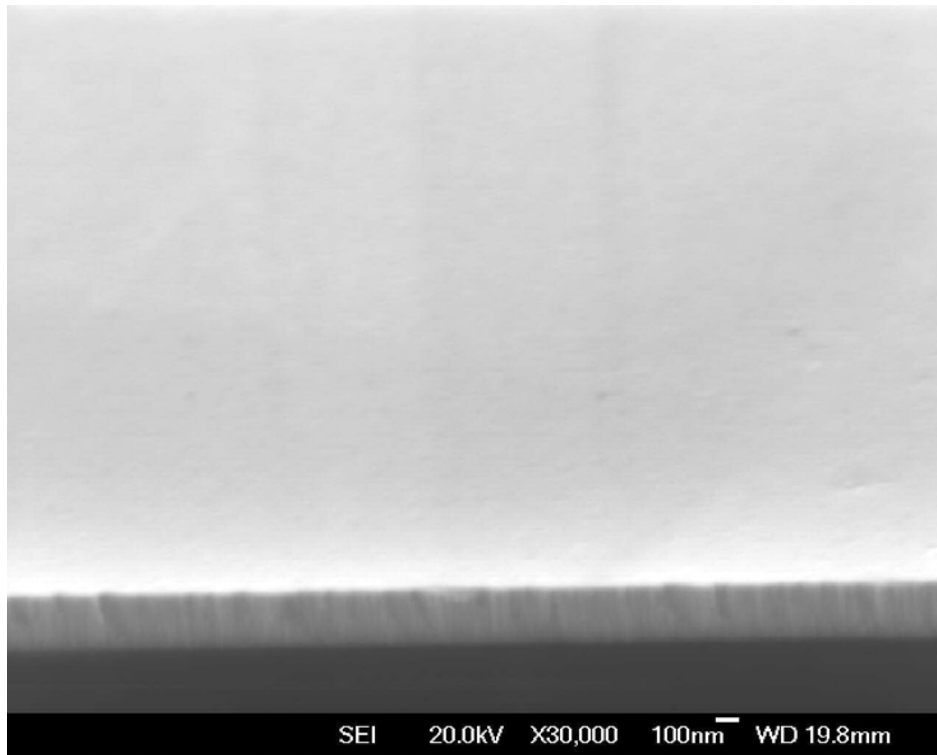


Figure 4.46 SEM cross-section image of the SZO film grown at $D_{T,S} = 60$ mm.

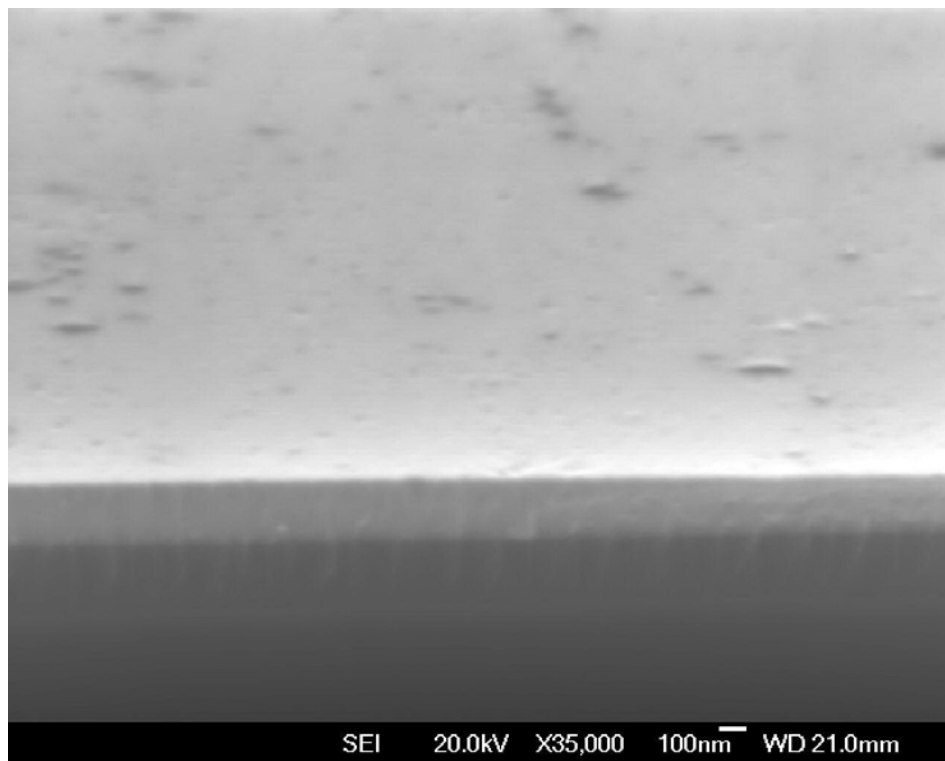


Figure 4.47 SEM cross-section image of the SZO film grown at $D_{T,S} = 70$ mm.

4.1.4 Influence of Number of Pulses on SZO films

Film thickness is also an important factor to control the properties of doped ZnO films, and film thickness is directly proportional to the deposition rate and time which at a certain target-to-substrate distance could be increased by the number of laser shots and deposition time.

The effect of film thickness on electrical properties of different TCO (Transparent Conducting Oxides) materials were studied by Hartnagel *et al.* [7]. A similar tendency was observed for tin oxide, indium tin oxide, and zinc oxide thin films. Thickness influences the electrical and structural properties of the films markedly. The grain size and thus crystallinity of the films improve with increasing thickness. The transmission properties of ITO and ZnO films are less sensitive to the film thickness.

Similar results were found for Al-doped ZnO films by Dong *et al.* [38]. When the film thickness was increased from 70 nm to 580 nm, the resistivity decreased from 2.6×10^{-4} to 1.8×10^{-4} Ω cm.

To study the effect of thickness on the film properties, the number of pulses is varied from 4000 to 6000 pulses. The other fixed deposition parameters during the film growth can be seen in Table 4.5.

Table 4.5 Summary of SZO deposition results by varying number of pulses.

Target No. 4 Substrate temperature= 300 ° C, Oxygen pressure = 5 mTorr, E (incident energy) = 170 mJ, Target-to-substrate distance = 70 mm									
Number of pulses	Thickness nm	Resistivity $\rho(\times 10^{-4}\Omega \text{ cm})$	Hall mobility μ ($\text{cm}^2\text{V}^{-1} \text{ S}^{-1}$)	Carrier concentration n (cm^{-3})	Transparency %	002 height	FWHM	RMS (nm)	Grain size nm
4000	313	6.48	26.3	3.03E+20	89	35468	0.40	0.71	14.4
5000	364	5.63	26.61	3.08E+20	87	96685	0.23	1.03	37.4
6000	439	5.3	28.7	4.1E+20	85.5	176751	0.22	1.36	46.9

4.1.4.1 Structural Properties of SZO Films by Varying Number of Pulses

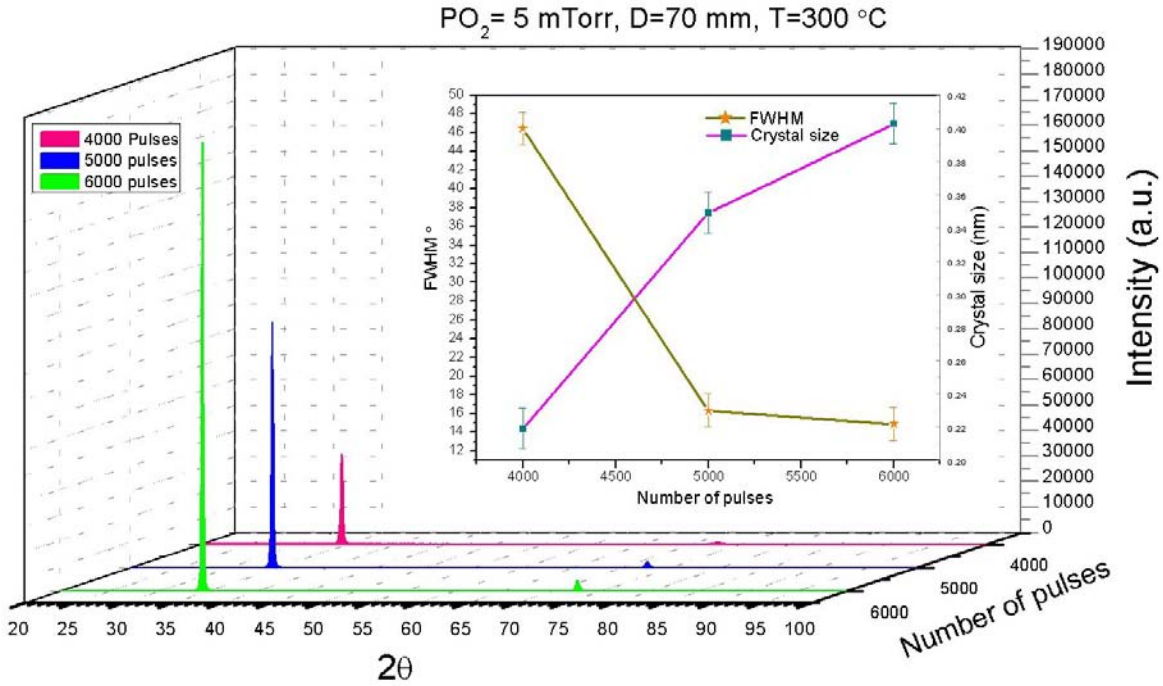


Figure 4.48 Variation of XRD patterns with number of pulses for SZO films; the inset shows the dependence of FWHM (deg.) for (002) peaks and crystal size (nm) of SZO films by varying number of pulses; the other used deposition parameters can be found in Table 4.5. The number of pulses varies from 4000 to 6000.

XRD measurements in Figure 4.48 indicate that the thicker films are more crystalline and have larger grains than thinner films. The FWHM (full width at half maximum) of the (002) peak values linked to the grain size of the film. Films with smaller FWHM have larger grain size resulting in better crystal quality.

Increasing the film thickness increased the crystal quality of film, indicated by the reduction of FWHM values as shown in Figure 4.49; the 313-nm-thick film has an average grain size of 14.4 nm and the 439-nm-thick film has an average grain size of 46.9 nm.

All the films exhibit a crystalline structure with (002) preferential orientation. As the number of pulses increased the (002) peak showed an increase in intensity as well as the (004) peak which is not as strong as (002) preferred orientation.

4.1.4.2 Electrical Properties of SZO Films by Varying Number of Pulses

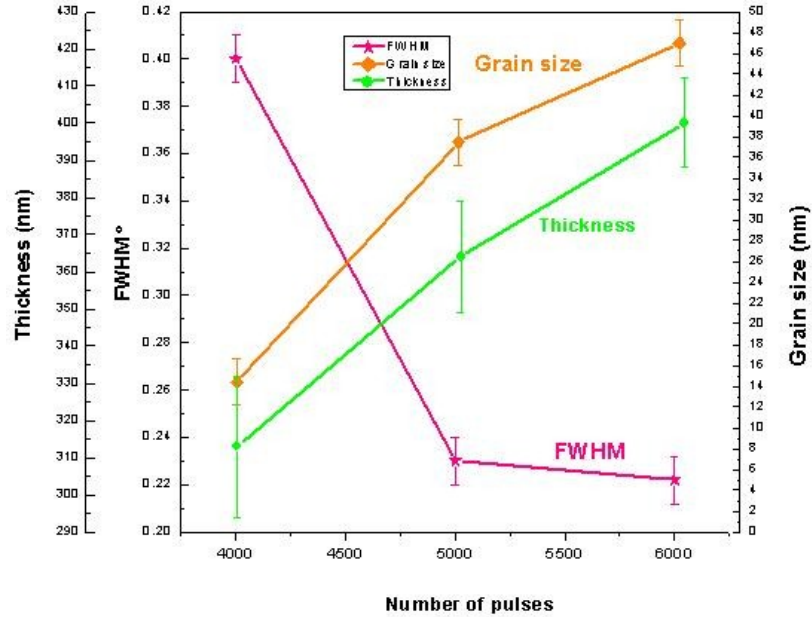


Figure 4.49 Dependence of thickness, grain size, and FWHM values of (002) peak on number of pulses in SZO films

As mentioned before, an increase in the film thickness leads to the higher crystal quality of film, because of an increase in FWHM values of the (002) peak as shown in Figure 4.49.

The dependence of the structural and electrical properties on film thickness for SZO films on glass substrate has been studied. Figure 4.50 illustrates that the resistivity of SZO films decreases with an increase in the film thickness which is in agreement with the result of Rao *et al.* [113]. In general, the electrical conductivity rises, as the film thickness increases, since the grain size rises with the thickness. Consequently grain boundary scattering is reduced by the increase of the grain size. It has been reported [114] that the carrier density increases with an increase in the film thickness, and the Hall mobility increases with increasing film thickness. Hence, the fall in resistivity can be attributed to a raise in both carrier density and carrier mobility of the films.

The results of XRD and Hall measurement data could be illustrated with the same method. Considering the smaller grain size for the film with thickness of 313 nm as shown in Figure 4.49,

decrease in mobility might be due to generated tensile stress at the grain boundaries with degradation in the crystalline quality [115].

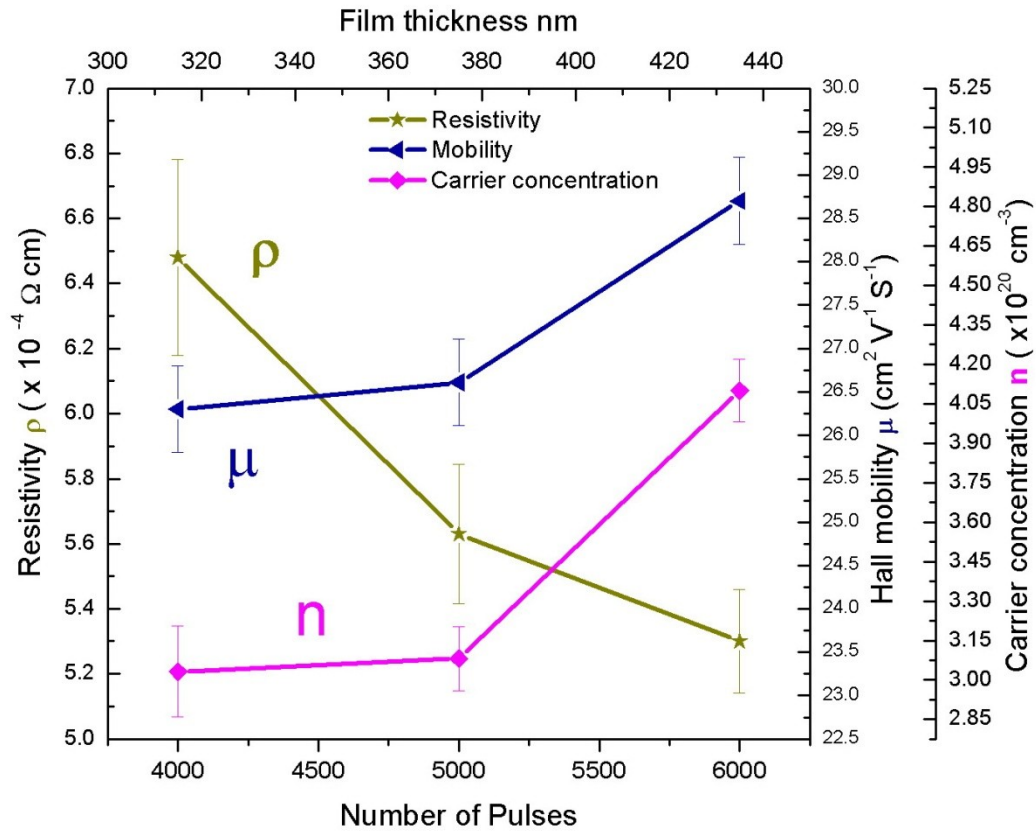


Figure 4.50 Variation of Carrier concentration n , Hall mobility μ and resistivity ρ as a function of number of pulses and film thickness nm for SZO films.

The XRD data shows an increase of grain size resulting from increasing film thickness. Generally, defects are accumulated on the grain boundaries. Films with small grains have large grain boundary. Therefore, the decrease of the grain size means increasing the defects in the film. The defects are donor type defects, so the degradation of the crystal quality causes the increase of electron concentration.

4.1.4.3 Optical Properties of SZO Films by Varying Number of Pulses

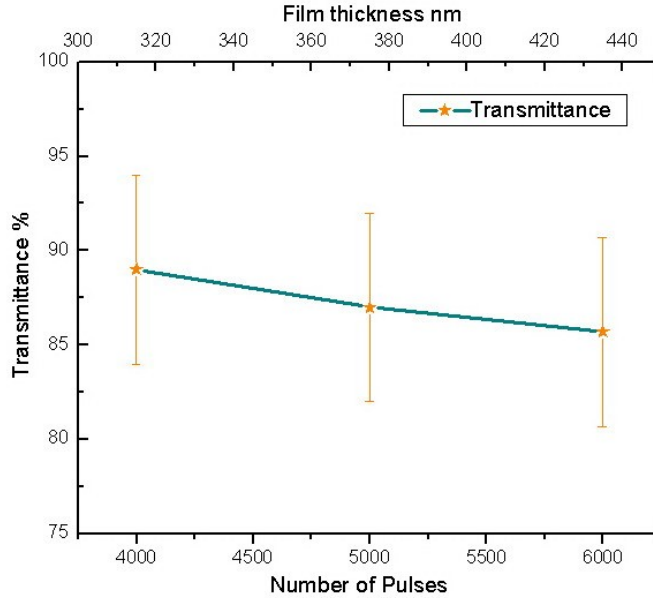


Figure 4.51 Transparency of the SZO films deposited by varying thickness and number of pulses at wavelength 635 nm. The other deposition parameters can be

Figure 4.51 and Figure 4.52 show the optical transmittance of as grown SZO films with different thickness by varying the number of pulses. The optical transmittance of all samples in the visible range is more than 85 % which shows the high crystal quality of the SZO films.

Figure 4.53 shows the plot of $(\alpha h\nu)^2$ vs. $h\nu$ (photon energy) for SZO films deposited by varying the number of pulses. The optical band gap is determined by the extrapolation method. The band gap energy of SZO films increases from 3.56 eV for the 313-nm-thick film to 3.65 eV for the 439-nm-thick film. As mentioned before, the variation of optical band gap with thickness can be explained by the Burstein-Moss model [40, 41] due to the higher carrier concentration of these films and filling of electronic states of the conduction band (Figure 4.54).

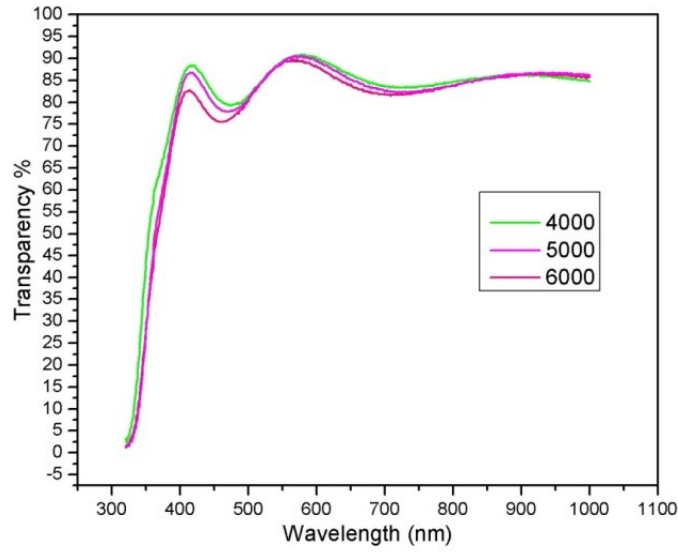


Figure 4.52 Transmittance spectra of SZO films as a function of number of pulses.

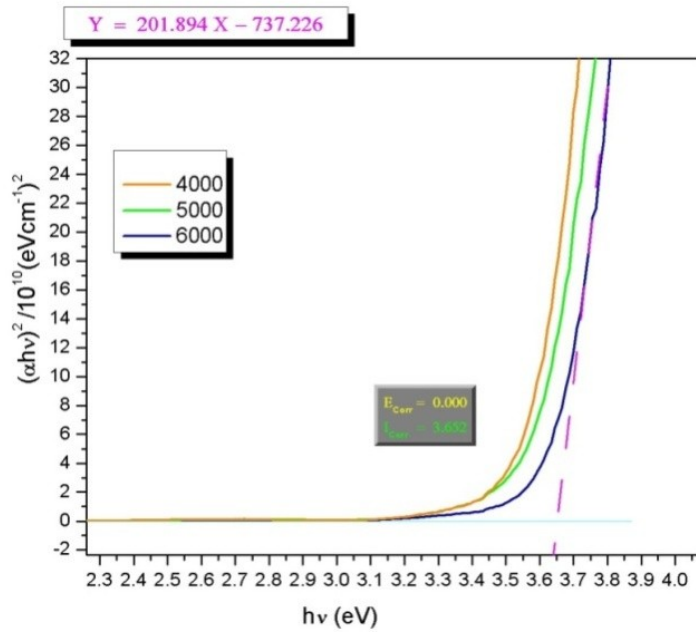


Figure 4.53 Plot of $(\alpha h\nu)^2$ vs. $h\nu$ (photon energy) for SZO films deposited by varying number of pulses (Method of calculating the bandgap from the transmittance for the SZO film deposited by 6000 pulses).

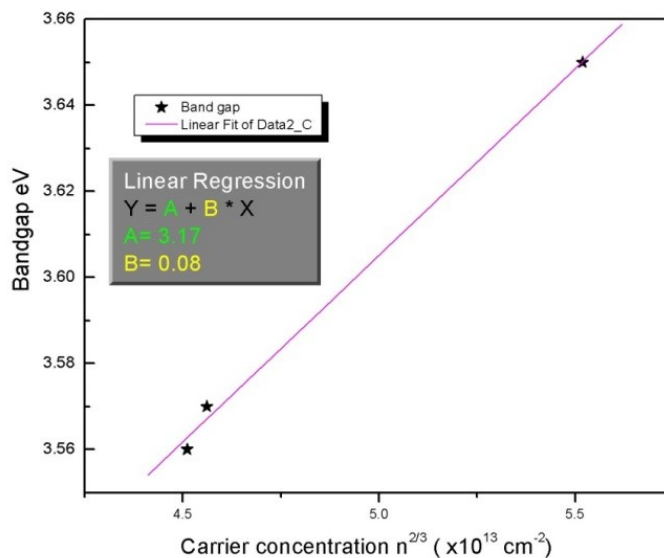


Figure 4.54 Band gap dependence of carrier concentration for the SZO films deposited by varying number of pulses

4.1.4.4 Surface morphology of SZO Films by Varying Number of Pulses

The surface morphology of the films deposited by different numbers of pulses changes gradually. Figure 4.55 to Figure 4.57 show the AFM plan and 3D view images of the SZO films with divergent thickness deposited by varying number of pulses.

During this research, however, the number of pulses was varied from 4000 to 6000 at intervals of 1000. In order to prove this theory a greater number of samples are required, to be deposited within a broader range of laser shot numbers.

SEM images of SZO films (Figure 4.60 to Figure 4.59) grown by different laser shot numbers, are correspondent to the AFM results and XRD patterns. The SZO 313-nm-thick film has smaller crystal size of 14 nm deposited by 4000 laser shots compared to the SZO 439-nm-thick film deposited by 6000 laser shots which has larger grain size of 46 nm.

As shown in Table 4.5 the RMS roughness gradually increases from 0.71 to 1.36 nm when the film thickness increases from 313 to 439 nm. The rise of RMS roughness value of SZO films with thickness is mainly attributed to the increase of grain size [115-117].

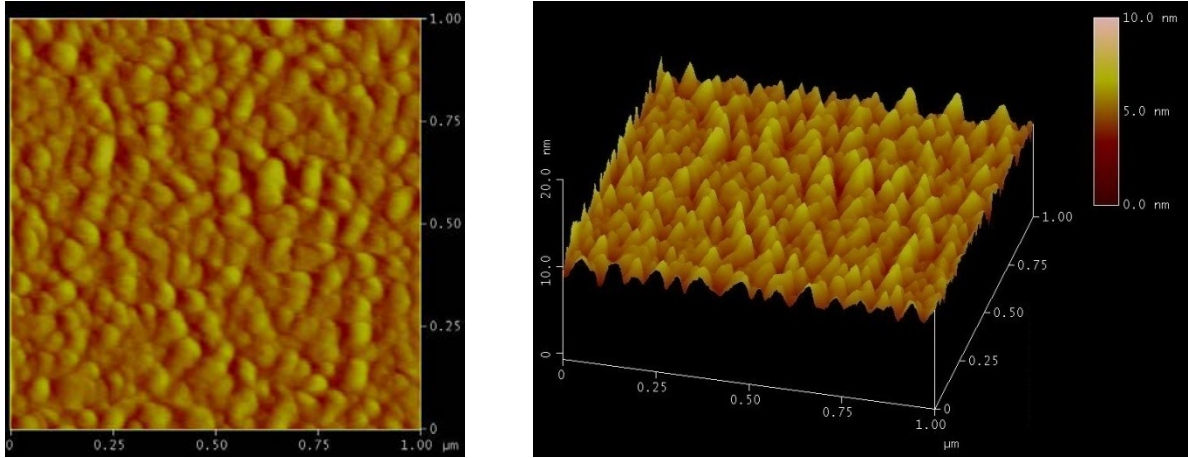


Figure 4.55 (Left) Front and (right) 3D view AFM images of the SZO film grown by 4000 laser shots.

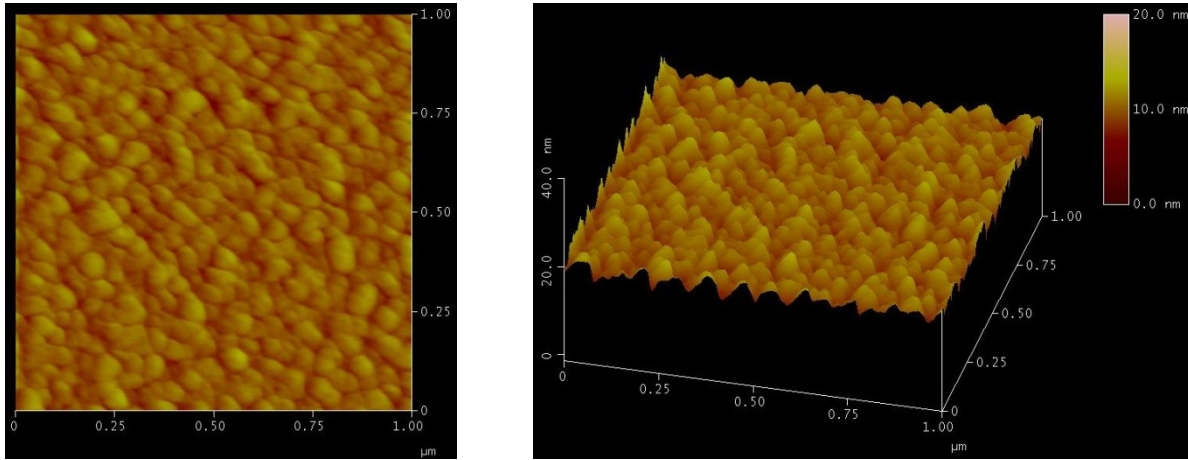


Figure 4.56 (Left) Front and (right) 3D view AFM images of the SZO film grown by 5000 laser shots.

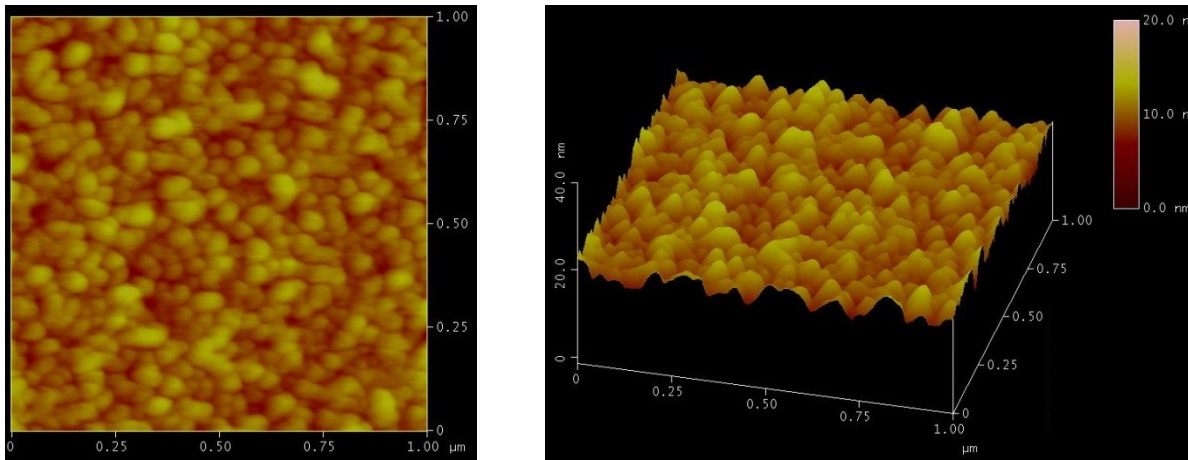


Figure 4.57 (Left) Front and (right) 3D view AFM images of the SZO film grown by 6000 laser shots.

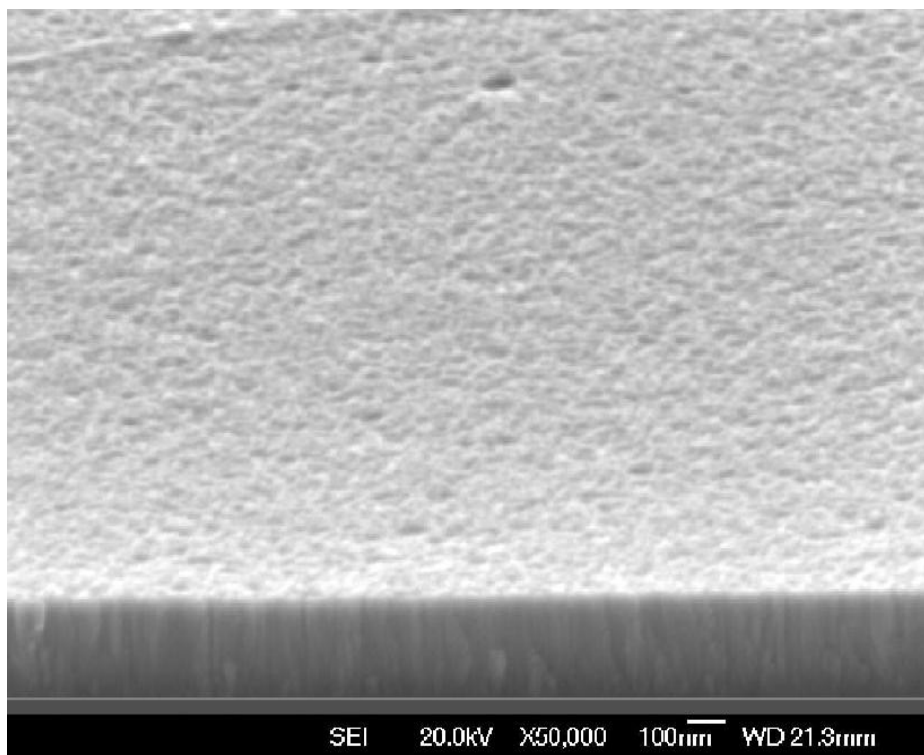


Figure 4.58 Cross section SEM image obtained for the SZO film fabricated by 4000 laser shots. Other parameters were fixed.

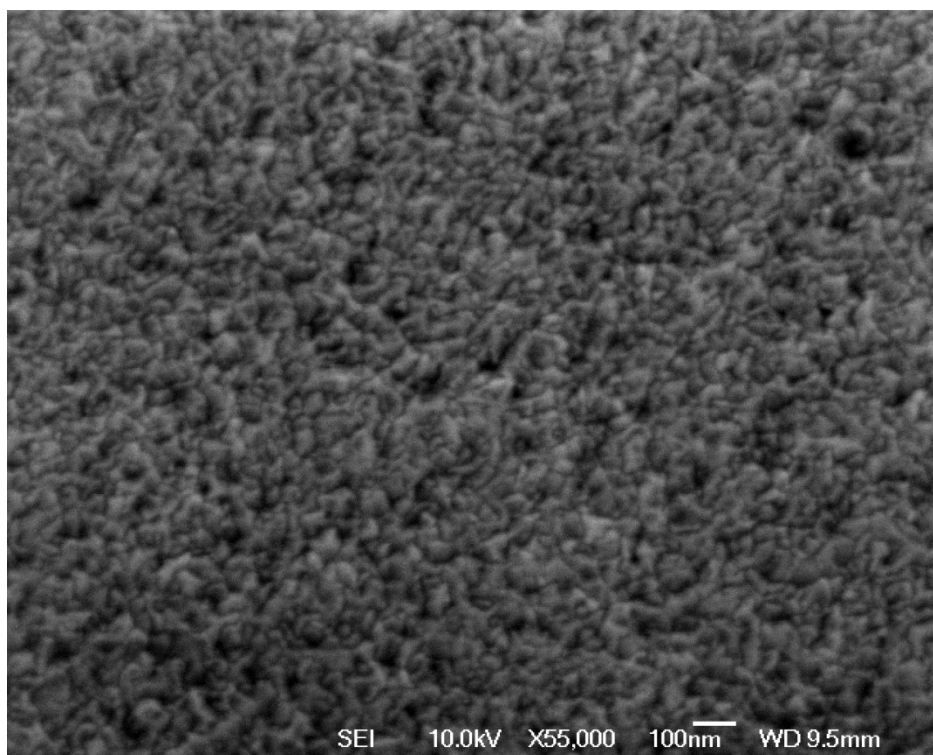


Figure 4.59 High-resolution SEM image obtained for the SZO film fabricated by 4000 laser shots.

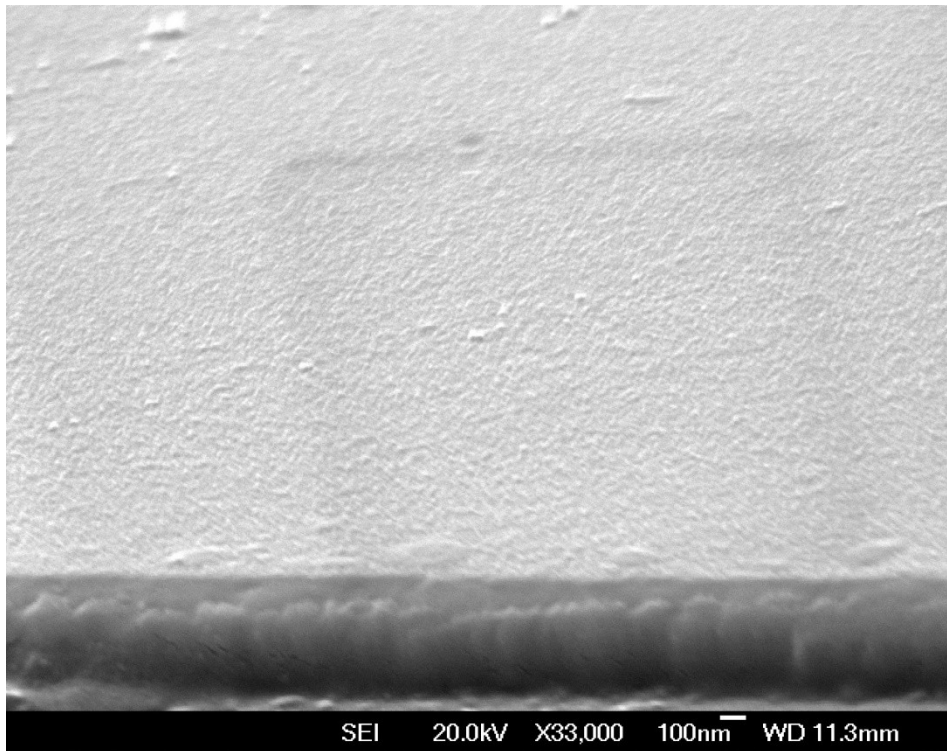


Figure 4.60 SEM cross-section image obtained for SZO film fabricated by 6000 laser shots. Other parameters were fixed.

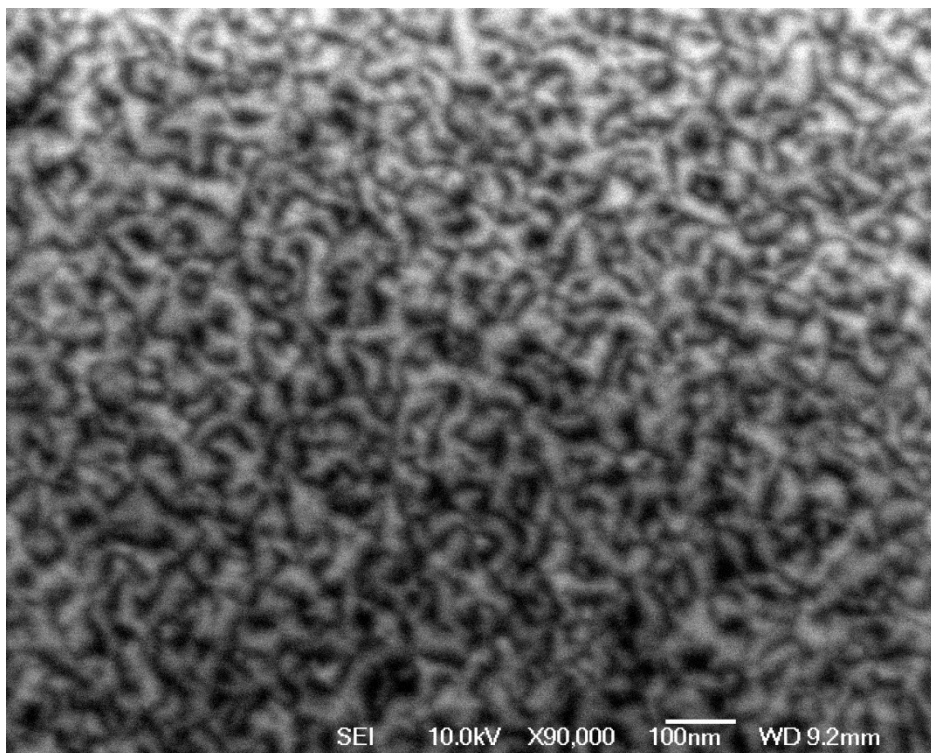


Figure 4.61 High-resolution SEM image obtained for the SZO film fabricated by 6000 laser shots.

5 Conclusion and Future Work

5.1 Conclusion

It has been established that, the structural, electrical, optical and morphological properties of transparent conducting Si-doped ZnO films depend on the main PLD parameters such as, the substrate temperature, oxygen pressure, target-to-substrate distance and the number of pulses. These involved parameters have been varied one by one and the influence of each parameter on the properties of the grown films has been studied and optimised. All films were found to be n-type.

Initially, it has been discussed that, resistivity decreases and transmission improves as substrate temperature increases to 300°C and then, both properties are adversely influenced by a further increase to 500°C. Increasing substrate temperature creates more oxygen vacancies and hence lower resistivity in these films. (002) texture rises constantly as temperature increases before it falls when temperature surpasses 350°C.

It was also found that as oxygen pressure rises to 5 mTorr at the fixed temperature of 300°C, resistivity initially falls to $4.1 \times 10^{-4} \Omega\text{cm}$ and then rises. The best compromise between surface pitting was found for the films deposited at 5 mTorr. Particulate concentration found out to increase pressure rises. The transmittance of the films deposited at oxygen pressure below 5 mTorr fell due to the reduction in grain size of the films.

The optimum target-to-substrate distance was obtained at 60 mm. The lower resistivity was obtained for the films deposited at target-to-substrate distance of 55 and 50 mm, which is attributed to the ejected species inside the plume being more easily promoted to an ionised state. However, the transparency of the film falls with a decrease in target-to-substrate distance, which is due to the combined influence of decreased RMS roughness and lower film thickness. The

film deposited at 60 mm distance was the optimised grown film with a transparency as high as 86 %, resistivity of $5.75 \times 10^{-4} \Omega\text{cm}$ and RMS value of 1 nm.

The optimised film, grown at 300°C, an oxygen pressure of 5 mTorr, and 5000 pulses had a resistivity of $4.12 \times 10^{-4} \Omega\text{cm}$ and a transmittance of 89%. The SZO film with above properties can emerge as an alternative to ITO, due to its comparable properties. In addition, ZnO films are cost-effective, non-toxic and can be fabricated with ease.

The electrical and optical properties of SZO films are influenced by the thickness variation of the films. This can be attributed to increased grain size, improved crystallinity and lower density of grain boundary, which affects the free carriers. Mean free path consideration, however, suggested that ionised impurity scattering is the dominant scattering mechanism. The carrier concentration didn't change significantly, indicating that after a threshold both carrier density and carrier mobility are becoming independent of the film thickness.

The values of band gap strongly are dependent on the carrier concentration, which in turn is influenced by deposition conditions. The absorption edge shifts towards higher energy with a rise in carrier concentration which can be explained by Burstein-Moss model.

5.2 Future Work

Ceramic targets used in PLD were prepared in the laboratory of the university by grinding and pressing of the powders followed by calcination and sintering of the pressed pellets. As such ZnO targets used in PLD are likely to be highly porous and brittle. Each target could not be used for more than maximum 15 depositions. In identical growth conditions by different targets, the physical properties of the grown films were not the same. These variations made the comparison among the physical properties of the different films difficult. More studies on the target preparation are required to fully understand of the process.

The properties of the films are affected by the diffusion of oxygen out of the film as well as into the film. Post deposition annealing in various ambient such as H_2 , NH_4 etc. may further improve the properties of the films.

The position of the substrate either out or within preset distance is probable to have a significant impact on the film properties.

Refractive index, extinction coefficient, and effective mass are other optical constants that would benefit from investigation.

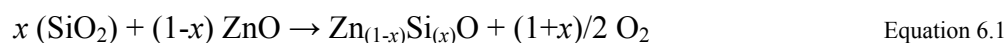
Considering future applications dealing with optical devices such as lasers or LEDs, high-quality epitaxial thin films have to be obtained. Using single crystals as substrates has attracted a large number of researchers to grow epitaxial ZnO thin films by PLD. C-cut Al_2O_3 single crystals (sapphire) or hexagonal $ScMgAlO_4$ (0001) leading to lower lattice mismatch can be substituted for borosilicate glass substrates due to the improved crystal quality of the films, which leads to a decrease in resistivity of the thin films.

Electron Back-Scatter Diffraction (EBSD) is needed to investigate the epitaxial growth of the films on sapphire substrates.

6 Appendix

6.1 Target Preparation

Different mixed powders from zinc oxide (ZnO, purity, 99.99%) and silicon dioxide (SiO₂, purity 99.99%) were studied to examine the solubility of silicon in the target. The possible reaction for the formation of Zn_(1-x)Si_(x)O is:



where x is the percentage of Silicon doping.

The weight percentage of the powders was calculated at 0-8 wt. %. The first group of powders were mixed in acetone and then heated to 800°C and 1100 °C in argon for 8-hour period, while the second group was heated in air. They were then ground and heated at the same temperature for another 8 hours in the same atmosphere. With X-ray diffraction (Philips X'Pert diffractometer), the solubility limit of SiO₂ in ZnO was studied and the secondary phase Zn₂SiO₄ was determined. The binary Zn₂SiO₄ compound exists in the SiO₂-ZnO system. The melting point of the eutectic on the ZnO-rich side is 1,507 °C, and on the SiO₂-rich side it is 1,432 °C[29].

Figure 6.1 illustrates that there is no solubility of SiO₂ and ZnO as well as the secondary phase Zn₂SiO₄ being the dominant composition (impurity) in the target for temperatures above 800°C. It can be seen from the Figure 6.1 d) that no peak was detected for the binary Zn₂SiO₄ compound at 2% doping. This can be explained by the shortage of oxygen in the furnace using Ar as ambient gas which prevented the formation of the Zn₂SiO₄ compound, compared with the same percentage of SiO₂ in air atmosphere (Fig 1.1b), but the fact that Zn₂SiO₄ was observed at higher percentage of silicon doping may rule this theory out.

To avoid the formation of the binary compound, the 2 wt. % Si-doped ZnO powder was chosen and two targets were made in different ambient atmosphere and temperature. Target 1 was calcinated for 8 hours at 750°C in air, ground and calcinated 8 hours at 850°C in air to make disk-shaped targets, 20 mm in diameter and 2 mm thick by a standard pellet press (10-25 ton), and then sintered at 800°C for 8 hrs in air to increase the mechanical strength of the target.

Target 2 was calcinated for 8 hours at 1100°C in Ar, ground and calcinated another 8 hours at 1100°C in Ar to make disk-shaped targets, 25 mm in diameter with 2 mm thick by standard pellet press (10-25 ton), and sintered at 800°C for 8 hrs in Ar to improve the mechanical strength of the target. As such ZnO targets used in PLD are likely to be highly porous and brittle [1] ; each target could not be used more than maximum 15 depositions (15×5000 pulses).

It can be seen from Figure 6.3 that in target 1 (sintered and calcinated in air at 800°C), beneath the surface the powder has not been sintered. It can be interpreted as 800°C is not high enough to have a ceramic target. The holes have been seen in earlier studies of oxide targets [118, 119]. The presence of micrometre-sized cavities on the surface of the both targets is a clear evidence of surface melting. The round shape of these cavities suggested that they were caused by the release of gas from beneath the surface when the region was molten

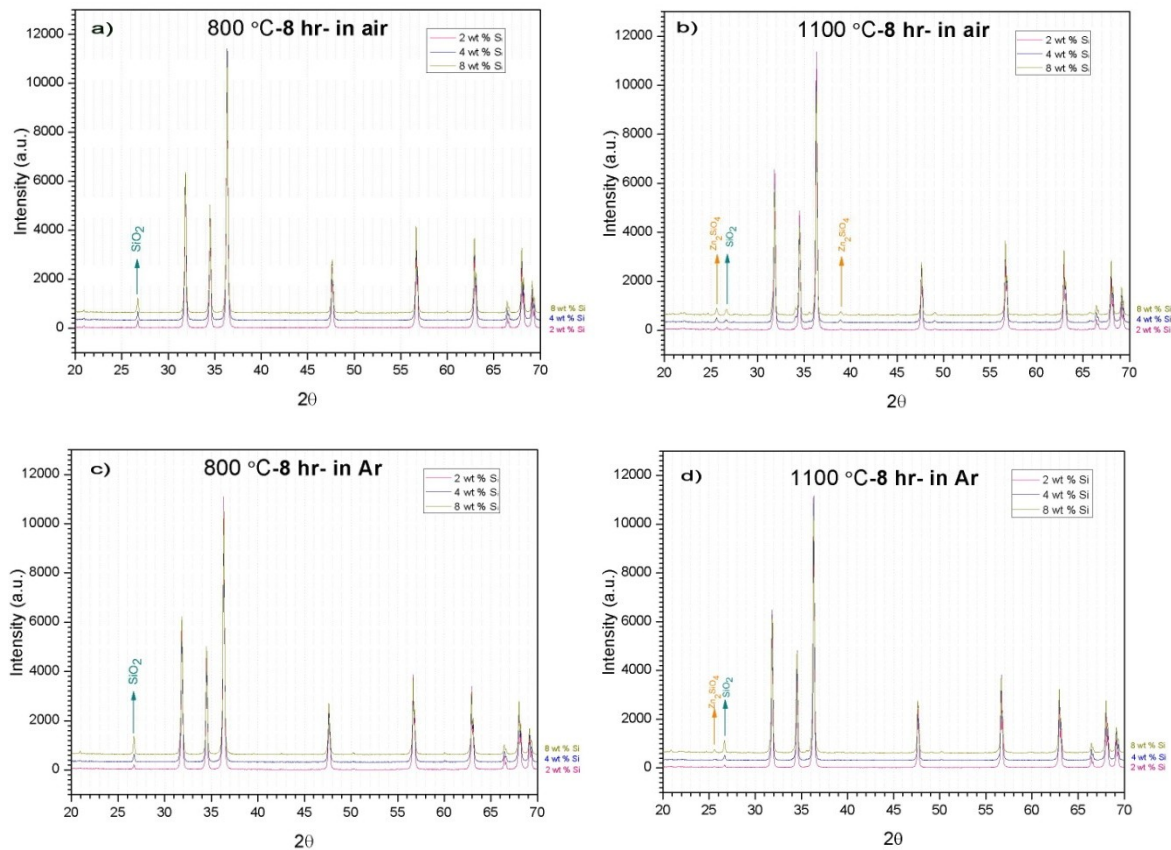


Figure 6.1 : XRD analysis of mixed powders 2, 4 and 8 percent Si-doped ZnO (Zinc oxide (purity, 99.99%) and SiO₂ (purity 99.99%)) a) 800°C in air b) 1100°C in air c) 800°C in Ar d) 1100°C in Ar (8 hours)

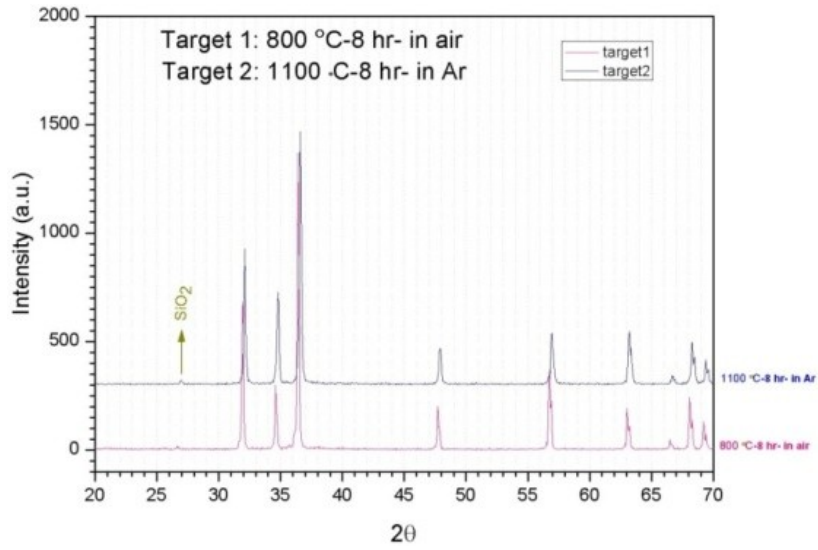
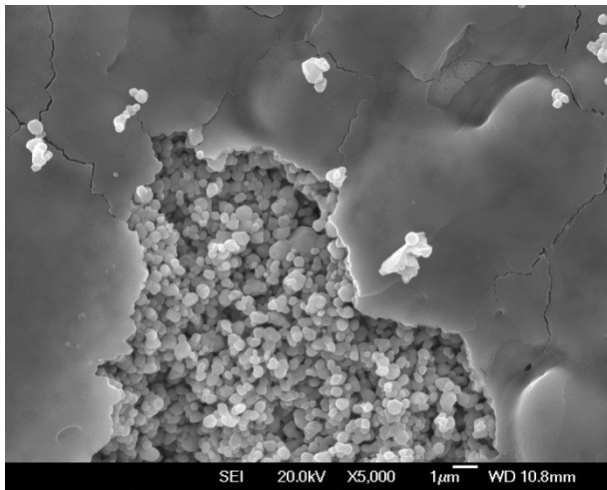


Figure 6.2 XRD analysis of 2 wt.% si-doped ZnO targets in air at 800 °C and in Ar at 1100 °C. The SiO₂ can be observed in both targets which shows Si couldn't diffuse into the ZnO structure as a dopant.

a)



b)

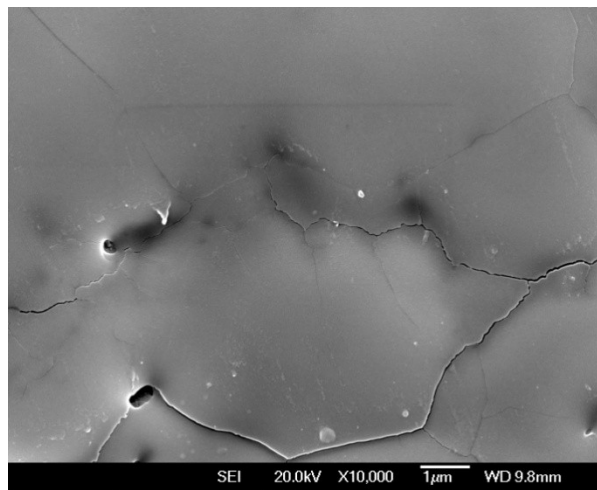


Figure 6.3 SEM micrograph of 2 wt.% si-doped ZnO targets after 10 depositions (50000 pulses, ~180 mJ incident energy) a) made in air at 800 °C b) made in Ar at 1100 °C. Cracks and holes exist in both targets.

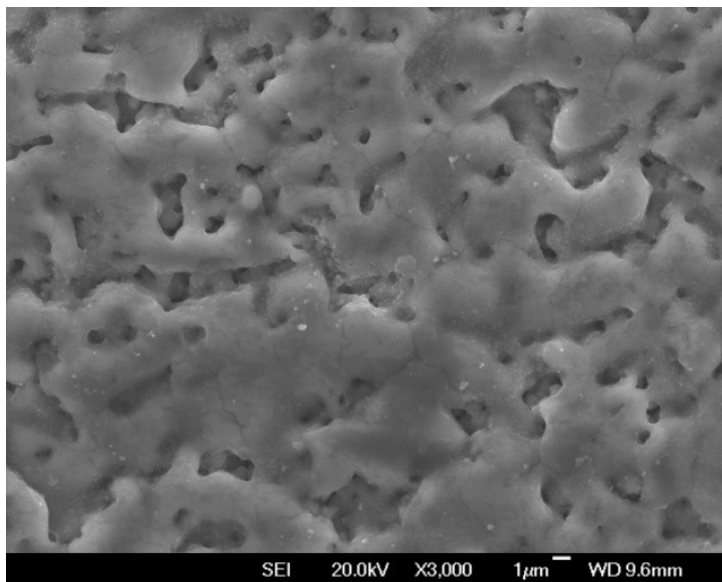


Figure 6.4 SEM micrograph of target 7 (2 wt.% Si-doped ZnO, calcined for 8 hr at 750 °C -8 hr at 850 °C in air, sintered 6 hr in air at 800 °C). The round shape of these cavities suggested that they were caused by the release of gas from underneath the surface when the area was molten.

For the rest of the experiments, the other 6 targets were all made identically from 2 wt.% Si-doped ZnO, calcined for 8 hr at 750 °C and 8 hr at 850 °C in air, sintered 6 hr in air at 800 °C, and 25×2 mm (diameter × height) were used (Figure 6.4). A list of the prepared targets can be found in Table 6.1.

Table 6.1 Summary of SZO targets fabricated under different circumstances

Target Number	Description
1	2% SZO 8-8 hr in air 800 °C calcined, 8 hr in air 800 °C sintered 25mm
2	2% SZO 8-8 hr in air 800 °C calcined, 8 hr in Ar 1100 °C sintered 25mm
3	2% SZO, 8 hr 750 °C -8 hr 850 °C in air calcined, 6 hr in air 800 °C sintered 25mm
4	2% SZO, 8 hr 750 °C -8 hr 850 °C in air calcined, 6 hr in air 800 °C sintered 25mm
5	2% SZO, 8 hr 750 °C -8 hr 850 °C in air calcined, 6 hr in air 800 °C sintered 25mm
6	2% SZO, 8 hr 750 °C -8 hr 850 °C in air calcined, 6 hr in air 800 °C sintered 25mm
7	2% SZO, 8 hr 750 °C -8 hr 850 °C in air calcined, 6 hr in air 800 °C sintered 25mm
8	3% SZO, 8 hr 750 °C -8 hr 850 °C in air calcined, 8 hr in air 800 °C sintered 25mm
9	2% SZO Commercial, 25mm

6.2 Hall Effect Measurements

Hall effect measurements were taken at the University of Oxford, the electrical characteristics of the SZO films were calculated by the equations below:

ρ – Electrical resistivity (Ω cm)

$$\rho = \frac{\pi}{\ln 2} d \frac{V_R}{I} f$$

where: d – sample thickness (cm)

V_R – resistivity voltage (mV)

I – electrical current (mA)

f – correction factor

$$\pi / \ln 2 = 4.5324$$

R_H – Hall coefficient (cm^3/As)

$$R_H = \frac{dV_H}{2BI} 10^4$$

where: d – Sample thickness (cm)

V_H – Hall voltage (mV)

I – electrical current (mA)

B – magnetic field (Vs/m^2) = 0.55 Vs/m^2

$n(p)$ – carrier concentration (cm^{-3})

$$n(p) = \frac{1}{R_H e}$$

where: e – electron charge (As) = 1.602×10^{-19} As

R_H – Hall coefficient (m^3/As)

μ – Carrier mobility (cm^2/Vs)

$$\mu = \frac{R_H}{\rho}$$

where: R_H – Hall coefficient (cm^3/As)

ρ – electrical resistivity ($\Omega \text{ cm}$)

V_H – Hall voltage (mV)

$$V_H = R_H I(B/t)$$

where: B – magnetic field (Vs/m^2)

I – electrical current (mA)

R_H – Hall coefficient (cm^3/As)

6.3 Other Deposition Conditions

Deposition rate can be controlled by many parameters such as laser fluence, oxygen partial pressure, and target-to-substrate distance. The deposition rate increases with increasing fluence, decreasing oxygen partial pressure, and decreasing the target-to-substrate distance, and is linearly proportional to the laser fluence. The threshold laser energy for ablation was found to be 180 mJ, and the deposition rate linearly increased with increasing laser energy up to 220 mJ (Figure 6.5). The laser fluence also affects the properties of ITO films. Low-resistivity films can be obtained at high fluence because the ejected species created at high fluence are much more energetic and can traverse the background gas to the substrate for crystalline film growth [120].

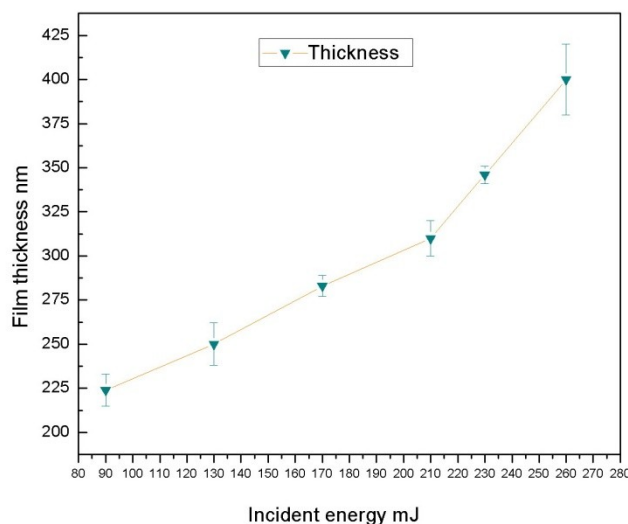


Figure 6.5 Dependence of thickness on incident energy in SZO films. The other deposition condition were: 5000 laser shots at 5 mTorr, 300 °C T_S and 70 mm D_{T-S} on the glass substrate.

For EDX (Energy-dispersive X-ray spectroscopy) analysis, the films have to be deposited on other substrate materials in which the acquired spectra of the elements in silicon-doped zinc oxide could not be influenced by the composition of the substrate. STO (SrTiO_3) and sapphire (Al_2O_3) were used as the substrate. This replacement didn't have significant influence on the electrical properties of the SZO films. The surface morphology of the films grown on STO showed slightly different pattern. No sign of epitaxy, however, has been seen for these samples.

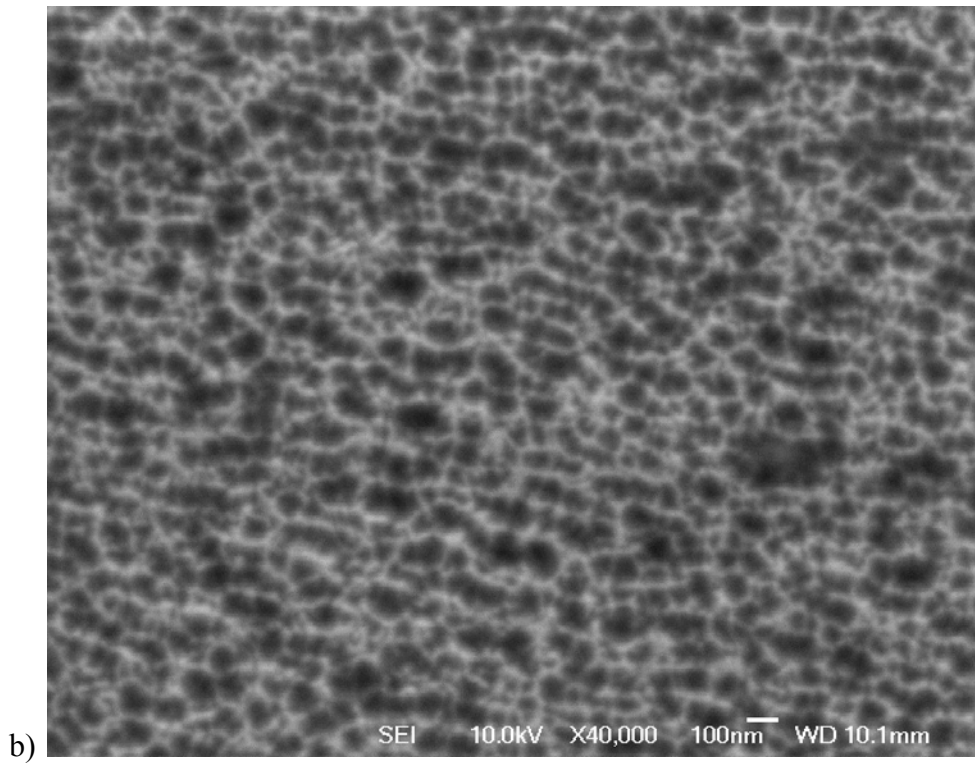
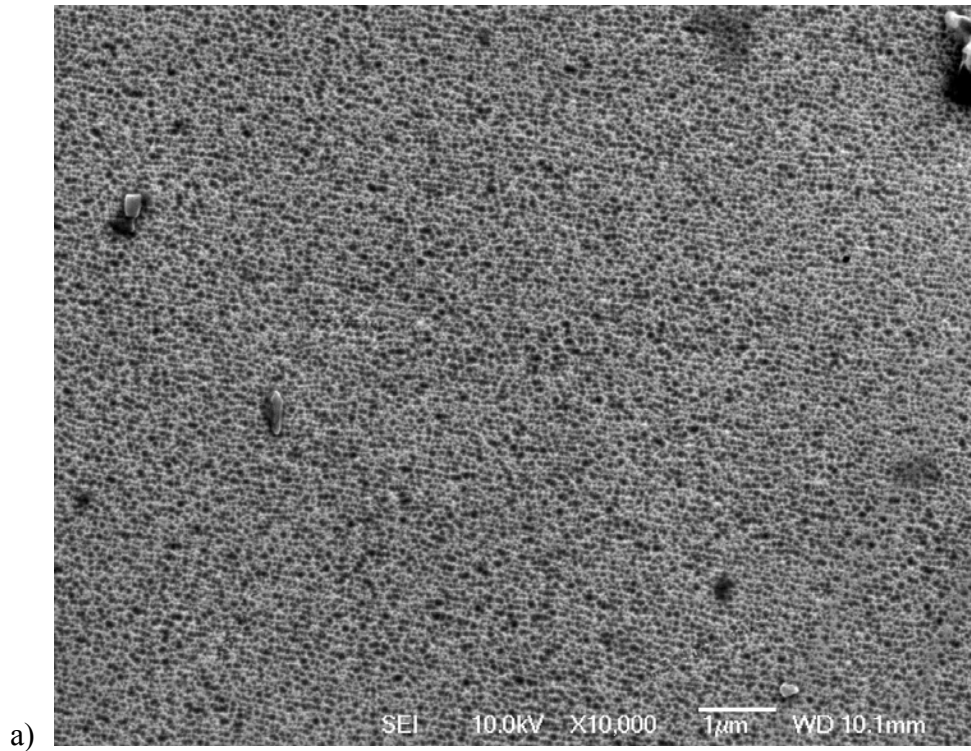


Figure 6.6 high resolution SEM images of the SZO film fabricated by 5000 laser shots at 5 mTorr, 300 °C T_s , 70 mm $D_{T,S}$, and $E=180$ mJ. a) $\times 10000$ b) $\times 40000$

7 References

1. Eason, R., *Pulsed Laser Deposition of Thin Films*. 2007: John Wiley & Sons, Inc.
2. K. Bädcker, *Über die elektrische Leitfähigkeit und die thermoelektrische Kraft einiger Schwermetallverbindungen*. *Annalen der Physik*, 1907. **327**(4): p. 749-766.
3. Yanagi, H.K., H. Kudo, A. Yasukawa, M. Hosono, H. *Chemical design and thin film preparation of p-type conductive transparent oxides*. 1998. Baltimore, Maryland: Kluwer Academic Publ.
4. Kawazoe, H.Y., M. Hyodo, H. Kurita, M. Yanagi, H. Hosono, H., *P-type electrical conduction in transparent thin films of CuAlO₂*. *Nature*, 1997. **389**(6654): p. 939-942.
5. Look, D.C. and D.C.L. Reynolds, C. W. Jones, R. L. Eason, D. B. Cantwell, G., *Characterization of homoepitaxial p-type ZnO grown by molecular beam epitaxy*. *Applied Physics Letters*, 2002. **81**(10): p. 1830-1832.
6. Kwon, B.J.K., H. S. Lee, S. K. Cho, Y. H. Hwang, D. K. Park, S. J., *Optical investigation of p-type ZnO epilayers doped with different phosphorus concentrations by radio-frequency magnetron sputtering*. *Applied Physics Letters*, 2007. **91**(6): p. 3.
7. H. L. Hartnagel, A.L.D., A. K. Jain, and C. Jagadish, *Semiconducting Transparent Thin Films*. 1995, Bristol: Institute of Physics. 358.
8. Ozgur, U.A., Y. I. Liu, C. Teke, A. Reshchikov, M. A. Dogan, S. Avrutin, V. Cho, S. J. and Morkoc, H., *A comprehensive review of ZnO materials and devices*. *Journal of Applied Physics*, 2005. **98**(4): p. 103.
9. <http://titan.physx.u-szeged.hu/~lamilab/plden.htm>.
10. Wang, Z.L., *Zinc oxide nanostructures: growth, properties and applications*. *Journal of Physics-Condensed Matter*, 2004. **16**(25): p. R829-R858.
11. http://en.wikipedia.org/wiki/File:Wurtzite_polyhedra.png.
12. Fujimura, N.N., T.Goto, S. Xu, J. F.Ito, T., *Control of preferred orientation for ZnO film, control of self-texture*. *Journal of Crystal Growth*, 1993. **130**(1-2): p. 269-279.
13. Burton, W.K.C., N. and Frank, F. C., *The growth of crystals and the equilibrium structure of their surfaces*. *Philosophical Transactions of the Royal Society of London Series a-Mathematical and Physical Sciences*, 1951. **243**(866): p. 299-358.
14. B.D. Cullity , S.R.S., *Elements of X-Ray Diffraction*. 3rd ed. 2001: Prentice Hall.
15. C. Klingshirn, *ZnO: From basics towards applications*. *physica status solidi (b)*, 2007. **244**(9): p. 3027-3073.
16. Agura, H., *Low resistivity transparent conducting Al-doped ZnO films prepared by pulsed laser deposition*. *Thin Solid Films*, 2003. **445**(2): p. 263-267.
17. Holmelund, E., *Pure and Sn-doped ZnO films produced by pulsed laser deposition*. *Applied Surface Science*, 2002. **197-198**: p. 467-471.

18. Kim, H., *Epitaxial growth of Al-doped ZnO thin films grown by pulsed laser deposition*. Thin Solid Films, 2002. **420-421**: p. 107-111.
19. Mass, J., P. Bhattacharya, and R.S. Katiyar, *Effect of high substrate temperature on Al-doped ZnO thin films grown by pulsed laser deposition*. Materials Science and Engineering B, 2003. **103**(1): p. 9-15.
20. Park, S.-M., T. Ikegami, and K. Ebihara, *Effects of substrate temperature on the properties of Ga-doped ZnO by pulsed laser deposition*. Thin Solid Films, 2006. **513**(1-2): p. 90-94.
21. Venkatachalam, S., Y. Iida, and Y. Kanno, *Preparation and characterization of Al doped ZnO thin films by PLD*. Superlattices and Microstructures, 2008. **44**(1): p. 127-135.
22. Chang, L.W. *Characterization of Ga-doped ZnO nanowires grown by thermal chemical vapor deposition*. 2008. Shanghai, PEOPLES R CHINA: Ieee.
23. Chen, K.J., F.Y. Hung, and S.J. Chang. *Structural Characteristic, Raman Analysis and Optical Properties of Indium-Doped ZnO Nanoparticles Prepared by Sol-Gel Method*. 2007. Fayetteville, AR: Amer Scientific Publishers.
24. Igasaki, Y. and H. Saito, *The effects of deposition rate on the structural and electrical properties of ZnO:Al films deposited on (112-bar 0) oriented sapphire substrates*. Journal of Applied Physics, 1991. **70**(7): p. 3613-3619.
25. Majumder, S.B., *Investigations on solution derived aluminium doped zinc oxide thin films*. Materials Science and Engineering B-Solid State Materials for Advanced Technology, 2003. **103**(1): p. 16-25.
26. Aktaruzzaman, A.F., G.L. Sharma, and L.K. Malhotra, *Electrical, optical and annealing characteristics of ZnO:Al films prepared by spray pyrolysis*. Thin Solid Films, 1991. **198**(1-2): p. 67-74.
27. Kumar, M., R.M. Mehra, and S.-Y. Choi, *Effect of oxygen ambient on structural, optical and electrical properties of epitaxial Al-doped ZnO thin films on r-plane sapphire by pulsed laser deposition*. Current Applied Physics, 2009. **9**(4): p. 737-741.
28. Al-Mamouri, M., *Silicon Doped Zinc Oxide Transparent Conducting Oxides* University of Birmingham (unpublished), 2008.
29. Levin EM, R.C., McMurdie HF (eds), ‘‘System ZnO-SiO₂’’ *Phase Diagrams for Ceramists*. 1930: The American Ceramic Society, 1964, Fig. 302 (after Bunting EN, Phase equilibria in the system SiO₂-ZnO. J Am Ceram Soc 13(1):5)).
30. Epurescu, G., *p-type ZnO thin films grown by RF plasma beam assisted Pulsed Laser Deposition*. Superlattices and Microstructures, 2007. **42**(1-6): p. 79-84.
31. Kim, H., *Pulsed laser deposition of Zr-N codoped p-type ZnO thin films*. Applied Physics a-Materials Science & Processing, 2008. **93**(3): p. 593-598.
32. Look, D.C. and B. Claftin. *P-type doping and devices based on ZnO*. 2003. Niagara Falls, New York: Wiley-V C H Verlag Gmbh.
33. Look, D.C. *The future of ZnO light emitters*. 2004. Kariega Game Reserve, SOUTH AFRICA: Wiley-V C H Verlag Gmbh.

34. Look, D.C., *As-doped p-type ZnO produced by an evaporation/sputtering process*. Applied Physics Letters, 2004. **85**(22): p. 5269-5271.
35. Krtschil, A. *Local p-type conductivity in n-GaN and n-ZnO layers due to inhomogeneous dopant incorporation*. 2005. Awaji Isl, JAPAN: Elsevier Science Bv.
36. Bagnall, D.M., *Optically pumped lasing of ZnO at room temperature*. Applied Physics Letters, 1997. **70**(17): p. 2230-2232.
37. Ohtomo, A., *Room temperature ultraviolet laser emission from ZnO nanocrystal thin films grown by laser MBE*. Materials Science and Engineering B-Solid State Materials for Advanced Technology, 1998. **54**(1-2): p. 24-28.
38. Dong, B.Z., *Effect of thickness on structural, electrical, and optical properties of ZnO : Al films deposited by pulsed laser deposition*. Journal of Applied Physics, 2007. **101**(3): p. 7.
39. Gupta, R.K., *Band gap engineering of ZnO thin films by In₂O₃ incorporation*. Journal of Crystal Growth, 2008. **310**(12): p. 3019-3023.
40. Burstein, M. and J. Loeb, *ANTITHROMBINE NATURELLE ET COFACTEUR PLASMATIQUE DE LHEPARINE*. Presse Medicale, 1954. **62**(71): p. 1486-1486.
41. Moss, T.S., *The interpretation of the properties of indium antimonide*. Proceedings of the Physical Society of London Section B, 1954. **67**(418): p. 775-782.
42. Dietz, R.E., J.J. Hopfield, and D.G. Thomas, *Excitons and the Absorption Edge of ZnO*. Journal of Applied Physics, 1961. **32**(10): p. 2282-2286.
43. Douglas B Chrisey, G.K.H., *Pulsed Laser Deposition of Thin Films*. 1994: A JOHN WILEY & SONS, INC., PUBLICATION. 612.
44. Chrisey, D.B., and G. K. Hubler, *Pulsed Laser Deposition of Thin Films*. 1994: Wiley, New York.
45. Banerjee, A.N., *Low-temperature deposition of ZnO thin films on PET and glass substrates by DC-sputtering technique*. Thin Solid Films, 2006. **496**(1): p. 112-116.
46. Heitsch, S., *Low temperature photoluminescence and infrared dielectric functions of pulsed laser deposited ZnO thin films on silicon*. Thin Solid Films, 2006. **496**(2): p. 234-239.
47. Matsumura, M. and R.P. Camata, *Pulsed laser deposition and photoluminescence measurements of ZnO thin films on flexible polyimide substrates*. Thin Solid Films, 2005. **476**(2): p. 317-321.
48. Craciun, V. *Effects of laser wavelength and fluence on the growth of zno thin-film by pulsed-laser deposition*. 1994. Strasbourg, France: Elsevier Science Bv.
49. Nakayama, T., *Neutral particle-emission from zinc-oxide surface induced by highdensity electronic excitation*. Radiation Effects Letters, 1982. **67**(5): p. 129-133.
50. Nakayama, T., *Laser-induced sputtering of zno, tio₂, cdse and gap near threshold laser fluence..* Surface Science, 1983. **133**(1): p. 101-113.

51. Sankur, H. and J.T. Cheung, *Highly oriented zno films grown by laser evaporation..* Journal of Vacuum Science & Technology a-Vacuum Surfaces and Films, 1983. **1**(4): p. 1806-1809.
52. Ianno, N.J. *Characterization of pulsed laser deposited zinc-oxide.* 1992. San Diego, Ca.
53. Craciun, V.A., S.Craciun, D.Elders, J.Gardeniers, J. G. E.Boyd, Ian W., *Effects of laser wavelength and fluence on the growth of ZnO thin films by pulsed laser deposition.* Applied Surface Science, 1995. **86**(1-4): p. 99-106.
54. Craciun, V., *Characteristics of high quality ZnO thin films deposited by pulsed laser deposition.* Applied Physics Letters, 1994. **65**(23): p. 2963-2965.
55. Minami, T., H. Nanto, and S. Takata, *OPTICAL-PROPERTIES OF ALUMINUM DOPED ZINC-OXIDE THIN-FILMS PREPARED BY RF MAGNETRON SPUTTERING.* Japanese Journal of Applied Physics Part 2-Letters, 1985. **24**(8): p. L605-L607.
56. Horio, N., *Preparation of zinc oxide/metal oxide multilayered thin films for low-voltage varistors.* Vacuum, 1998. **51**(4): p. 719-722.
57. Kim, H., *Transparent conducting aluminum-doped zinc oxide thin films for organic light-emitting devices.* Applied Physics Letters, 2000. **76**(3): p. 259-261.
58. Kim, H., *Indium tin oxide thin films for organic light-emitting devices.* Applied Physics Letters, 1999. **74**(23): p. 3444-3446.
59. Kim, H., *Effect of aluminum doping on zinc oxide thin films grown by pulsed laser deposition for organic light-emitting devices.* Thin Solid Films, 2000. **377-378**: p. 798-802.
60. Kim, S.S. and B.-T. Lee, *Effects of oxygen pressure on the growth of pulsed laser deposited ZnO films on Si(0 0 1).* Thin Solid Films, 2004. **446**(2): p. 307-312.
61. Kim, H. *Doped ZnO thin films as anode materials for organic light-emitting diodes.* 2002. San Diego, California.
62. Matsubara, K., *ZnO transparent conducting films deposited by pulsed laser deposition for solar cell applications.* Thin Solid Films, 2003. **431-432**: p. 369-372.
63. Ismail, R.A., *Transparent and conducting ZnO films prepared by reactive pulsed laser deposition.* Journal of Materials Science-Materials in Electronics, 2007. **18**(4): p. 397-400.
64. Prasada Rao, T. and M.C. Santhoshkumar, *Effect of thickness on structural, optical and electrical properties of nanostructured ZnO thin films by spray pyrolysis.* Applied Surface Science, 2009. **255**(8): p. 4579-4584.
65. Haga, K., *High-quality ZnO films prepared on Si wafers by low-pressure MO-CVD.* Thin Solid Films, 2003. **433**(1-2): p. 131-134.
66. Hirate, T., *Effects of laser-ablated impurity on aligned ZnO nanorods grown by chemical vapor deposition.* Thin Solid Films, 2005. **487**(1-2): p. 35-39.
67. Lu, J.G., *ZnO-based thin films synthesized by atmospheric pressure mist chemical vapor deposition.* Journal of Crystal Growth, 2007. **299**(1): p. 1-10.

68. Bashir, A., *High-Performance Zinc Oxide Transistors and Circuits Fabricated by Spray Pyrolysis in Ambient Atmosphere*. *Advanced Materials*, 2009. **21**(21): p. 2226-+.
69. Ergin, B., E. Ketenci, and F. Atay, *Characterization of ZnO films obtained by ultrasonic spray pyrolysis technique*. *International Journal of Hydrogen Energy*, 2009. **34**(12): p. 5249-5254.
70. Wang, B., *The grain boundary related p-type conductivity in ZnO films prepared by ultrasonic spray pyrolysis*. *Applied Physics Letters*, 2009. **94**(19).
71. Carcia, P.F., *Transparent ZnO thin-film transistor fabricated by rf magnetron sputtering*. *Applied Physics Letters*, 2003. **82**(7): p. 1117-1119.
72. Kim, K.K., *The grain size effects on the photoluminescence of ZnO/alpha-Al₂O₃ grown by radio-frequency magnetron sputtering*. *Journal of Applied Physics*, 2000. **87**(7): p. 3573-3575.
73. Sato, H., *Transparent conducting p-type nio thin-films prepared by magnetron sputtering*. *Thin Solid Films*, 1993. **236**(1-2): p. 27-31.
74. Minami, T., *Transparent conducting ZnO thin films deposited by vacuum arc plasma evaporation*. *Thin Solid Films*, 2003. **445**(2): p. 268-273.
75. Nakanishi, Y., *Preparation of ZnO thin films for high-resolution field emission display by electron beam evaporation*. *Applied Surface Science*, 1999. **142**(1-4): p. 233-236.
76. Kim, H., *Anode material based on Zr-doped ZnO thin films for organic light-emitting diodes*. *Applied Physics Letters*, 2003. **83**(18): p. 3809-3811.
77. Park, S.H.K., *Characteristics of organic light emitting diodes with Al-doped ZnO anode deposited by atomic layer deposition*. *Japanese Journal of Applied Physics Part 2-Letters & Express Letters*, 2005. **44**(1-7): p. L242-L245.
78. Zhao, J.Q., *Organic light-emitting diodes with AZO films as electrodes*. *Synthetic Metals*, 2000. **114**(3): p. 251-254.
79. Berry, J.J., D.S. Ginley, and P.E. Burrows, *Organic light emitting diodes using a Ga : ZnO anode*. *Applied Physics Letters*, 2008. **92**(19).
80. Jeong, S.H., *Al-ZnO thin films as transparent conductive oxides : Synthesis, characterization, and application tests*. *Journal of the Korean Physical Society*, 2007. **50**(3): p. 622-625.
81. Nayak, P.K., *Spin-coated Ga-doped ZnO transparent conducting thin films for organic light-emitting diodes*. *Journal of Physics D-Applied Physics*, 2009. **42**(3).
82. Masuda, S., *Transparent thin film transistors using ZnO as an active channel layer and their electrical properties*. *Journal of Applied Physics*, 2003. **93**(3): p. 1624-1630.
83. Xiao, R.F., *Growth of c-axis oriented gallium nitride thin films on an amorphous substrate by the liquid-target pulsed laser deposition technique*. *Journal of Applied Physics*, 1996. **80**(7): p. 4226-4228.
84. Komuro, S., *1.54 mu m emission dynamics of erbium-doped zinc-oxide thin films*. *Applied Physics Letters*, 2000. **76**(26): p. 3935-3937.

85. Komuro, S., *Highly erbium-doped zinc-oxide thin film prepared by laser ablation and its 1.54 μ m emission dynamics*. Journal of Applied Physics, 2000. **88**(12): p. 7129-7136.
86. Triboulet, R. and J. Perrière, *Epitaxial growth of ZnO films*. Progress in Crystal Growth and Characterization of Materials, 2003. **47**(2-3): p. 65-138.
87. Binnig, G., C.F. Quate, and C. Gerber, *Atomic Force Microscope*. Physical Review Letters, 1986. **56**(9): p. 930.
88. Kourosh Kalantar-zadeh, B.F., *Nanotechnology-Enabled Sensor*: Springer; 1 edition (October 31, 2007).
89. Dep., C.C.; Available from: <http://ece-www.colorado.edu/~bart/book/ellipsom.htm>.
90. *Obituary. Thomas Edwin Hall*. N Z Med J, 1979. **89**(632): p. 229.
91. Petersen, D.H., *Micro-four-point probe Hall effect measurement method*. Journal of Applied Physics, 2008. **104**(1).
92. Moulzolf, S.C., D.J. Frankel, and R.J. Lad, *In situ four-point conductivity and Hall effect apparatus for vacuum and controlled atmosphere measurements of thin film materials*. Review of Scientific Instruments, 2002. **73**(6): p. 2325-2330.
93. <http://www.imagesco.com/articles/superconductors/four-point-electrical-probe.html>.
94. Keogh, R., *Final year report*. Metallurgy and Materials eng. University of Birmingham, 2008.
95. Zhao, Y., Y. Jiang, and Y. Fang, *The influence of substrate temperature on ZnO thin films prepared by PLD technique*. Journal of Crystal Growth, 2007. **307**(2): p. 278-282.
96. Khandelwal, R., *Effects of deposition temperature on the structural and morphological properties of thin ZnO films fabricated by pulsed laser deposition*. Optics and Laser Technology, 2008. **40**(2): p. 247-251.
97. Kang, S.J., *Effect of substrate temperature on structural, optical and electrical properties of ZnO thin films deposited by pulsed laser deposition*. Journal of Materials Science-Materials in Electronics, 2008. **19**(11): p. 1073-1078.
98. Pandis, C., *Role of low O₂ pressure and growth temperature on electrical transport of PLD grown ZnO thin films on Si substrates*. Solid-State Electronics, 2006. **50**(6): p. 1119-1123.
99. Shan, F.K. and Y.S. Yu, *Optical properties of pure and Al doped ZnO thin films fabricated with plasma produced by excimer laser*. Thin Solid Films, 2003. **435**(1-2): p. 174-178.
100. Shan, F.K. and Y.S. Yu. *Optical properties of pure and Al doped ZnO thin films fabricated with plasma produced by excimer laser*. 2002. Jeju Isl, South Korea.
101. Park, S.M., *Structure and properties of transparent conductive doped ZnO films by pulsed laser deposition*. Applied Surface Science, 2006. **253**(3): p. 1522-1527.
102. Kim, H., *Electrical, optical, and structural properties of indium-tin-oxide thin films for organic light-emitting devices*. Journal of Applied Physics, 1999. **86**(11): p. 6451-6461.

103. Caporaletti, O., *Electrical and optical-properties of bias sputtered zno thin-films*. Solar Energy Materials, 1982. **7**(1): p. 65-73.
104. Nisha, M., *Effect of substrate temperature on the growth of ITO thin films*. Applied Surface Science, 2005. **252**(5): p. 1430-1435.
105. McLean, T.P. and E.G.S. Paige, *A theory of the effects of carrier-carrier scattering on mobility in semiconductors*. Journal of Physics and Chemistry of Solids, 1960. **16**(3-4): p. 220-236.
106. Hwang, J.H., *Point defects and electrical properties of Sn-doped In-based transparent conducting oxides*. Solid State Ionics, 2000. **129**(1-4): p. 135-144.
107. Kim, S.H., *Electrical and optical characteristics of ITO films by pulsed laser deposition using a 10 wt.% SnO₂-doped In₂O₃ ceramic target*. Thin Solid Films, 2005. **475**(1-2): p. 262-266.
108. Hammond, R.H. and R. Bormann, *Correlation between the in situ growth conditions of YBCO thin films and the thermodynamic stability criteria*. Physica C: Superconductivity, 1989. **162-164**(Part 1): p. 703-704.
109. Castro-Rodriguez, R., *Correlation between target-substrate distance and oxygen pressure in pulsed laser deposition of complex oxide thin films*. Applied Physics - Materials Science & Processing, 2005. **81**(7): p. 1503-1507.
110. Kim, H.S. and H.S. Kwok, *Correlation between target-substrate distance and oxygen pressure in pulsed laser deposition of yba₂cu₃o₇*. Applied Physics Letters, 1992. **61**(18): p. 2234-2236.
111. Shim, E.S., *Effect of the variation of film thickness on the structural and optical properties of ZnO thin films deposited on sapphire substrate using PLD*. Applied Surface Science, 2002. **186**(1-4): p. 474-476.
112. Suzuki, A., *Highly conducting transparent indium tin oxide films prepared by pulsed laser deposition*. Thin Solid Films, 2002. **411**(1): p. 23-27.
113. Rao, T.P. and M.C. Santhoshkumar, *Effect of thickness on structural, optical and electrical properties of nanostructured ZnO thin films by spray pyrolysis*. Applied Surface Science, 2009. **255**(8): p. 4579-4584.
114. Lin, K.M., Y.Y. Chen, and K.Y. Chou, *Solution derived Al-doped zinc oxide films: doping effect, microstructure and electrical property*. Journal of Sol-Gel Science and Technology, 2009. **49**(2): p. 238-242.
115. Kishimoto, S., *Dependence of electrical and structural properties on film thickness of undoped ZnO thin films prepared by plasma-assisted electron beam deposition*. Superlattices and Microstructures, 2006. **39**(1-4): p. 306-313.
116. Bouderbala, M., *Thickness dependence of structural, electrical and optical behaviour of undoped ZnO thin films*. Physica B: Condensed Matter, 2008. **403**(18): p. 3326-3330.
117. Mridha, S. and D. Basak, *Effect of thickness on the structural, electrical and optical properties of ZnO films*. Materials Research Bulletin, 2007. **42**(5): p. 875-882.

118. Craciun, V., *Scanning electron microscopy investigation of laser ablated oxide targets*. Journal of Physics D-Applied Physics, 1999. **32**(12): p. 1306-1312.
119. Chivel, Y., M. Petrushina, and I. Smurov, *Influence of initial micro-porosity of target on material ejection under nanosecond laser pulses*. Applied Surface Science, 2007. **254**(4): p. 816-820.
120. Coutal, C., A. Azema, and J.C. Roustan, *Fabrication and characterization of ITO thin films deposited by excimer laser evaporation*. Thin Solid Films, 1996. **288**(1-2): p. 248-253.